UNIVERSITÀ DI PARMA

UNIVERSITÀ DEGLI STUDI DI PARMA

DOTTORATO DI RICERCA IN SCIENZE CHIMICHE

XXXV CICLO

Organic dyes in condensed media: photophysics beyond gas phase

Coordinatore
Prof. Alessia Bacchi

Relatore
Prof. Francesca Terenziani
Prof. Anna Painelli

Dottorando
Dang Khoa Andrea Phan Huu

Anni accademici 2019/20 - 2021/2022

Contents

Introduction

The simulation of the properties of dyes in condensed phase is a daunting but rewarding task with enormous practical implications. For example, in the field or organic opto-electronics, a thorough understanding of the interplay between the active organic dye and the host material may lead to the optimal tuning of the properties of the device, in a *smart matrix* approach. By its nature, the computational study of large disordered systems requires reliable approximations. To this aim, effective models for the dye and the medium are useful to rationalize the behaviour of complex systems.

Chapter 1 of this work addresses a general issue: how the electronic degrees of freedom of the medium, i.e. the medium polarizability, affect the properties of the dye. In line with widespread effective solvation models, approaches are sought for, where the environmental degrees of freedom are renormalized away towards effective molecular Hamiltonians implicitly accounting for the interaction with the environment. The separation of the solute and environmental degrees of freedom relies on the different time scales of relevant motions. Two limiting cases can be considered. The adiabatic coupling neglects the kinetic energy associated to the medium degrees of freedom. The antiadiabatic coupling instead considers an instantaneous response of the medium degrees of freedom to relevant events occurring in the dye. The adiabatic and antiadiabatic approaches allow to renormalize away the medium degrees of freedom leading to effective solvation models and quite naturally apply when the medium degrees of freedom are much slower and faster, respectively, than the relevant degrees of freedom of the dye. The non-adiabatic approach corresponds to the complete quantum mechanical treatment of the system and the medium, but, apart from its computational cost, it requires a detailed knowledge of the dynamics of the medium.

The reaction field model, introduced in Section 1.2, is used as a basis to define the Hamiltonian for the solute-solvent system (Section 1.3). When modelling polarizable non-polar solvents, the electronic degrees of freedom of the solvent, falling in the far UV re much faster than the electronic degrees of freedom of the dye, whose transitions fall in the UV-visible region. Therefore, in Section 1.4, the antiadiabatic approximation is introduced on electronic degrees of freedom of the environment, yielding a renormalized antiadiabatic Hamiltonian. In Section 1.4.1, few-state models are adopted for representative dipolar and quadrupolar

dyes, and the antiadiabatic approach is validated against the numerically exact non-adiabatic results.

Despite their widespread use, current implementations of effective solvation models struggle to accurately describe the phenomenon, leading to a proliferation of approaches, that often yield widely different, and sometimes unphysical, results. Indeed, in current implementations, the electronic degrees of freedom of the medium are treated in the adiabatic approximation, failing to properly account for the medium polarizability, as demonstrated comparing spectroscopic properties computed in the adiabatic and the antiadiabatic limit. In Section 1.5, the issue of electronic solvation of thermally-activated delayed fluorescence (TADF) emitters is tackled, showing how the adiabatic approaches to electronic solvation can lead to spurious results, such as the solvent-induced breaking of the Hund's rule. In Section 1.6 electronic solvation of (multi)polar dyes is discussed more generally, describing several molecular systems (dipolar, quadrupolar and octupolar chromophores) with a family of parametric Hamiltonians, called essential state models. In particular, the antiadiabatic approach and the adiabatic approaches to fast solvation are compared paying attention to absorption and fluorescence spectra, and to the phenomenon of symmetry breaking.

Chapter 2 focuses on modelling TADF dyes in liquid solvents and amorphous matrices. A computational analysis at the DFT and TD-DFT level (Section 2.3.1) and an experimental characterization (Section D.1) on a representative system for twisted donor-acceptor TADF emitters set the bars for a reliable description of the complex TADF photophysics. In Section 2.3.2, the the two-state model presented in Section 1.6 is extended to account for triplet states, an effective molecular vibration and an effective conformational mode. The model is then parametrized against *first principle* calculations and validated against experimental spectra in solution (Section 2.3.3).

In Section 2.4.1, the subtle problem of the calculation of photophysical rates is attacked. The non-adiabaticity and anharmonicity of the molecular modes, like the torsion around the donor-acceptor bond, are important to achieve reliable estimates of transitions rates involving spin-crossover between excited states that are close in energy. To this aim, the model discussed in Section 2.3.2 is solved accounting for the torsional coordinate as a quantum coordinate. The transition rates between eigenstates of different spin multiplicities are then computed using Fermi's golden rule, and the overall rate from initial to final manifolds are obtained as thermal averages, assuming that internal conversion is much faster than the transition of interest. The effect of different molecular parameters and of the solvent polarizability is then studied.

Finally, in Section 2.6, the dynamical response of the medium is considered with great care. Orientational relaxation in liquid solvents occurs on a faster time scale (picoseconds) than the transitions occurring in the solute (from nanoseconds, in case of fluorescence and non-radiative decay, to the micro- or millisecond in case of spin-flip processes) and the solvent is therefore always in equilibrium with the dye (Section 2.6.1). In organic matrices, most, but not all, orientational relaxation pathways are hindered, giving rise to an intricate dynamics characterized by static and dynamic disorder (Section 2.6.2). The model presented in Section 2.3.2 allows for the calculation of the photophysical rates and the simulation of time resolved emission spectra in both liquid solvent and amorphous matrix.

Electronic solvation of (multi)polar chromophores

1

1.1 Introduction

The field of theoretical and computational chemistry greatly benefited from the rapid increase in computational power that occurred over the last century. Indeed, while the first chemistry-related problems dealt by quantum mechanical approaches just involved a few atoms, today quantum chemistry is a widespread tool in research, allowing scientists to gain precious and often experimentally not accessible insights on large systems of up to thousands of atoms.[1, 2] However, a full quantum-mechanical description of macroscopic systems is only possible in crystals, where lattice symmetry can be exploited. Moreover, if the sample is disordered (e. g. in liquid solvents, organic matrices or biological environments) a full quantum-mechanical description of macroscopic systems is not currently, if ever, possible.

A first step to approach the issue is to partition the macroscopic sample into *system* and *environment*. The definition of the boundary between the two requires some chemical intuition and strictly depends on the problem at hand. Of course, the system must contain the chemical species responsible for the phenomenon of interest, and is described with relatively high accuracy, while the environment consists of everything else that may affect the physics of the phenomenon, and it is described with lower accuracy.

In this work, optical spectroscopy in condensed phase is addressed. Specifically, the system of interest is the *solute*, i. e. the chromophore(s) responsible for optical transitions, and the environment describes the disordered medium in which the solute is dispersed, which will be called *solvent*, irrespective of its specific nature of liquid, organic matrix or biological environment.

The development of practical and reliable approaches to simulate how the solvent affects the optical properties of the solute is desirable in many fields of research, from bio-imaging to materials science, and has significant practical implications. For example, the photophysics of dyes used in opto-electronic devices (e. g. organic light emitting devices, organic photovoltaics, etc...) is deeply affected by the environment in which they are dispersed, making it possible, in principle, the concurrent optimization of sought properties in a smart matrix approach.

Once a proper approach is selected to describe the solute, an approach must be defined to treat the solute-solvent interaction,

compromising between accuracy and computational cost. Inter-molecular interactions are commonly classified in specific (hydrogen bonds, halogen bonds, π-π interactions, etc) and non-specific (dielectric interactions, Van der Waals forces, London dispersion, etc.). When specific interactions are involved, the most straightforward approach includes the interacting solvent molecules into the *system* subspace, effectively considering the chromophore and these molecules as a single entity.[1] When specific interactions can be neglected, the solvent is described by its dielectric properties, as electrostatic forces dominate its interplay with the solute.

The dielectric response function of a generic material is strictly related to the transitions it undergoes when it is subjected to an oscillating electromagnetic field. Each transition generates a peak in the absorption spectrum (the imaginary part of the dielectric response) at the frequency of resonance (Figure 1.1). According to the frequency of the electromagnetic field, different modes of the material are involved in the transition: high energy electronic transitions, such as core electron excitations, fall in the far UV, low energy electronic transitions typically occur in the UV-visible region, vibrational transitions fall in the infrared (IR) and rotational transitions in the microwave region. The real part of the dielectric function is characterized by discontinuities at the resonance frequencies and plateaus in the transparency windows.

Each transition contributes to the real value of the dielectric function in the plateau, based on its intensity. [2] Electronic transitions contribute to the optical dielectric constant, ϵ_{opt}, which amounts to the squared refractive index, η.[4] Vibrational transitions are weak and give small contributions to the dielectric constant.[3] Rotational motion is responsible for the low frequency region of the dielectric function: nonpolar solvents are optically silent and the dielectric function stays constant down to its static value, so that $\epsilon_{st} \sim \epsilon_{opt}$. In polar solvents instead, the rotational motion of polar solvent molecules in liquid phase is optically active and gives a large contribution to the static dielectric constant that increases with polarity of the solvent, so that $\epsilon_{st} > \epsilon_{opt}$.[4] In solid matrices the rotational motion is hindered and its contribution to the static dielectric constant is reduced.

As already stated, this work focuses on solute electronic transitions that resonate in the visible region. Good solvents must be transparent in the spectroscopic region of interest, i.e. the near UV-visible regions ($\sim 1\,\mathrm{eV} - 4\,\mathrm{eV}$). The electronic degrees of freedom of the solvent, typically in the far UV, are therefore faster than electronic degrees of freedom of the solute. On the other hand, vibrational and orientational degrees of freedom of the solvent, in the infrared and microwave regions respectively, are slower - in the picosecond

1: Some implicit solvation models, like the SMD model, are parametrized to account for some specific interactions, like hydrogen bonding.

2: This comes naturally from the Kramers-Krönig equations, that relate the real and imaginary parts of the dielectric function:

$$\mathrm{Re}\left\{\epsilon\left(\nu\right)\right\} = \frac{1}{\pi}\fint_{-\infty}^{\infty}\frac{\mathrm{Im}\left\{\epsilon\left(\nu'\right)\right\}}{\nu'-\nu}d\nu'$$

$$\mathrm{Im}\left\{\epsilon\left(\nu\right)\right\} = -\frac{1}{\pi}\fint_{-\infty}^{\infty}\frac{\mathrm{Re}\left\{\epsilon\left(\nu'\right)\right\}}{\nu'-\nu}d\nu'$$

where ϵ is the complex dielectric function, ν is the frequency, and $\fint$ denotes the Cauhy principal value integral.[3]

3: Of course, the dielectric function is weakly frequency dependent in the UV-visible region of interest. By convention the refractive index, η^2, is measured at 589 nm, corresponding to the D-line of sodium.

timescale for liquid solvents, and longer in solid matrices. The different timescales for the solute and solvent response justify the system-environment separation between solute and solvent.

1.2 The reaction field model

The laws of electrostatics that govern solute-solvent interactions are well-known. In the following sections, the solute-solvent interaction is described in the dipolar approximation: the solute is described as a point dipole occupying a cavity in the solvent, which is described as a dielectric continuum. Due to the presence of the solute, the solvent generates an electric field, called the *reaction field*, proportional to the solute dipole moment. In a self-consist way, the reaction field polarizes the solute and the solute dipole moment polarizes the solvent.[5, 6]

The vastly different response timescale of electronic and orientational degrees of freedom of the solvent allows for a separation between the electronic and orientational components of the reaction field, F_{el} and F_{or} respectively. Modelling the solvent as a bi-modal elastic medium,[4] the total Hamiltonian is

$$\mathcal{H} = \mathcal{H}_{gas} + \left[\frac{1}{2} K_{el} \vec{F}_{el}^2 + T_{el} - \hat{\vec{\mu}} \cdot \vec{F}_{el} \right] + \left[\frac{1}{2} K_{or} \vec{F}_{or}^2 + T_{or} - \hat{\vec{\mu}} \cdot \vec{F}_{or} \right]$$

(1.1)

where $\mathcal{H}_{gas}$ is the gas phase molecular Hamiltonian, $\hat{\vec{\mu}}$ is the molecular dipole moment operator, T_{el} (T_{or}) is the kinetic energy associated to electronic (orientational) solvent degrees of freedom, and K_{el} (K_{or}) the relevant force constant. At the equilibrium, the energy is at a minimum for both F_{el} and F_{or} and, exploiting the Hellmann-Feynman theorem:

$$0 = \frac{\partial \langle \mathcal{H} \rangle}{\partial F_{el}} = K_{el} \langle F_{el} \rangle - \langle \mu \rangle$$

(1.2)

$$0 = \frac{\partial \langle \mathcal{H} \rangle}{\partial F_{or}} = K_{or} \langle F_{or} \rangle - \langle \mu \rangle$$

(1.3)

So that, at the equilibrium, the reaction field is proportional to the dipole moment. The following relations are obtained:

$$F_{el} = r_{el} \langle \mu \rangle \qquad r_{el} = \frac{1}{K_{el}}$$

(1.4)

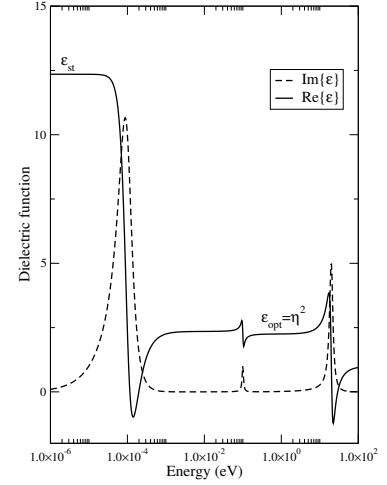$$F_{or} = r_{or} \langle \mu \rangle \qquad r_{or} = \frac{1}{K_{or}}$$

(1.5)

Figure 1.1: Real and imaginary parts of the dielectric function of a generic polar solvent with one electronic, one vibrational and one rotational transition, each modelled as a Lorentzian:

$$\epsilon(\omega) = 1 + \frac{Ne^2}{\epsilon_0 m_e V} \sum_j \frac{f_j}{\omega_j^2 - \omega^2 + i\omega\Gamma_j}$$

where N/V is the density (number of molecules in unit volume), e is the electron charge, m_e is the electron mass, ϵ_0 is the vacuum permittivity, f_j, ω_j and Γ_j are respectively the oscillator strength, transition frequency and width associated to the j-th transition.

4: One harmonic mode is associated to electronic degrees of freedom, the other to orientational degrees of freedom. While this approximation may seem drastic, the details obtained if additional modes are considered is lost as soon as either the *adiabatic* or the *antiadiabatic* approximations are made.

Eq. 1.1 can be rewritten as

$$\mathcal{H} = \mathcal{H}_{gas} + \left[\frac{\vec{F}_{el}^2}{2r_{el}} + T_{el} - \hat{\vec{\mu}} \cdot \vec{F}_{el} \right] + \left[\frac{\vec{F}_{or}^2}{2r_{or}} + T_{or} - \hat{\vec{\mu}} \cdot \vec{F}_{or} \right] \quad (1.6)$$

The proportionality constants r_{el} and r_{or} between the field and the dipole moment depend on the dielectric function of the solvent, and on specific solute-solvent pair properties, such as the shape and size of the cavity occupied by the solute. For a spherical cavity, r_{el} and r_{or} have a simple analytical form, as proposed by Onsager:[5]

$$r_{el} = \frac{1}{2\pi\epsilon_0 a^3} f\left(\epsilon_{opt}\right) \quad (1.7)$$

$$r_{or} = \frac{1}{2\pi\epsilon_0 a^3} \left[f\left(\epsilon_{st}\right) - f\left(\epsilon_{opt}\right) \right] \quad (1.8)$$

where a is the radius of the cavity, ϵ_0 is the vacuum permittivity and $f\left(\epsilon\right) = \frac{\epsilon-1}{2\epsilon+1}$.

Orientational degrees of freedom of the solvent are much slower than the relevant degrees of freedom of the solute, so that the kinetic energy of the orientational motion, $\hat{T}_{or}$, can be neglected, making $\mathcal{H}$ parametrically dependent on F_{or}. In other words, F_{or} can be treated as a classical mode. This is known as the *adiabatic* approximation, at the basis of well-established theories that rationalize the behaviour of dyes solvated in polar media (solvatochromism).[5, 7, 8] On the other hand, electronic solvent degrees of freedom are more delicate: they are faster than electronic transitions of the solute, therefore the kinetic energy, T_{el}, is non-negligible. In the following sections, approaches to electronic solvation are discussed.

Since polar solvation is well understood, the focus of this work is only on electronic solvation, as relevant to non-polar solvents, so that the Hamiltonian of interest reduces to:

$$\mathcal{H} = \mathcal{H}_{gas} + \left[\frac{\vec{F}_{el}^2}{2r_{el}} + T_{el} - \hat{\vec{\mu}} \cdot \vec{F}_{el} \right] \quad (1.9)$$

In Section 1.3 the numerically exact non-adiabatic approach to electronic solvation is discussed. In Section 1.4 the antiadiabatic approximation is imposed, and the antiadiabatic Hamiltonian is derived from the non-adiabatic one. In Section 1.4.1 the antiadiabatic approximation is numerically evaluated by comparison with non-adiabatic and adiabatic approaches.

1.3 The non-adiabatic approach

In the non-adiabatic approach, both solute and solvent are treated at the quantum level. The solvent operators are expressed in second quantization, setting

$$F_{el} = g\left(\hat{b}^\dagger + \hat{b}\right) \tag{1.10}$$

$$T_{el} = \left[i\frac{\sqrt{\hbar\omega_{el}}}{2}\left(\hat{b}^\dagger - \hat{b}\right)\right]^2 \tag{1.11}$$

where $\hat{b}$ ($\hat{b}^\dagger$) is the bosonic annihilation (creation) operator, $g = \sqrt{\hbar\omega_{el}r_{el}/2}$ is the strength of the coupling, and ω_{el} is the frequency assigned to the electronic polarization of the solvent, typically in the far UV. Substituting eq. 1.10 and 1.11 into eq. 1.9 gives the second quantized Hamiltonian:

$$\mathcal{H} = \mathcal{H}_{gas} - g\hat{\mu}\left(\hat{b}^\dagger + \hat{b}\right) + \hbar\omega_{el}\left(\hat{b}^\dagger\hat{b} + \frac{1}{2}\right) \tag{1.12}$$

where the first term on the right side is the gas phase Hamiltonian of the solute, the second term is the solute-solvent interaction Hamiltonian, and the last term is the Hamiltonian of the harmonic oscillator associated to the solvent. The most convenient basis is obtained as the direct product of the solute basis times the solvent basis, where the solvent basis consists of the eigenstates of the harmonic oscillator. Of course, the solute and the solvent basis must be truncated to numerically solve the problem by direct diagonalization of the Hamiltonian.[5]

For the sake of clarity, a molecular system described in terms of three electronic states (f_1, f_2, f_3) is considered. If the matrix elements $h_{ij} = \langle f_i| \mathcal{H}_{gas} |f_j\rangle$ and $\mu_{ij} = \langle f_i| \hat{\mu} |f_j\rangle$ are known, the non-adiabatic Hamiltonian matrix can be written on the product basis as[6]

$$\mathcal{H} = \begin{pmatrix} h_{11} & h_{12} & h_{13} & -g\mu_{11} & -g\mu_{12} & -g\mu_{13} & 0 & 0 & 0 \\ \cdot & h_{22} & h_{23} & -g\mu_{21} & -g\mu_{22} & -g\mu_{23} & 0 & 0 & 0 \\ \cdot & \cdot & h_{33} & -g\mu_{31} & -g\mu_{32} & -g\mu_{33} & 0 & 0 & 0 \\ \cdot & \cdot & \cdot & h_{11}+\hbar\omega_{el} & h_{12} & h_{13} & -\sqrt{2}g\mu_{11} & -\sqrt{2}g\mu_{12} & -\sqrt{2}g\mu_{13} \\ \cdot & \cdot & \cdot & \cdot & h_{22}+\hbar\omega_{el} & h_{23} & -\sqrt{2}g\mu_{21} & -\sqrt{2}g\mu_{22} & -\sqrt{2}g\mu_{23} \\ \cdot & \cdot & \cdot & \cdot & \cdot & h_{33}+\hbar\omega_{el} & -\sqrt{2}g\mu_{31} & -\sqrt{2}g\mu_{32} & -\sqrt{2}g\mu_{33} \\ \cdot & \cdot & \cdot & \cdot & \cdot & \cdot & h_{11}+2\hbar\omega_{el} & h_{12} & h_{13} \\ \cdot & \cdot & \cdot & \cdot & \cdot & \cdot & \cdot & h_{22}+2\hbar\omega_{el} & h_{23} \\ \cdot & \cdot & \cdot & \cdot & \cdot & \cdot & \cdot & \cdot & h_{33}+2\hbar\omega_{el} \end{pmatrix} \tag{1.13}$$

The diagonalization of this non-adiabatic Hamiltonian is of course possible, at least for not too large numbers of solute and solvent states, and would lead to a numerically exact non-adiabatic solution. However, this treatment would require a detailed knowledge of the solvent dielectric response. Moreover, it is computationally expensive as the product basis rapidly increases in size as the

5: The solute basis is truncated to a few low-energy electronic excitations. Convergence on the number of solvent quanta is rapidly achieved (typically 1 to 3 quanta), as $\hbar\omega_{el}$, falling in the UV, is larger than electronic excitations of the solute, falling in the near UV or visible regions.

6: Hermiticity of $\mathcal{H}$ is exploited to avoid writing the lower triangle of the Hamiltonian matrix. The solvent basis is truncated to the lowest three eigenstates of the harmonic oscillator, so that the basis is

$$|f_1,0\rangle, |f_2,0\rangle, |f_3,0\rangle,$$
$$|f_1,1\rangle, |f_2,1\rangle, |f_3,1\rangle,$$
$$|f_1,2\rangle, |f_2,2\rangle, |f_3,2\rangle.$$

7: If n is the number of solute electronic states, N is the number of electronic polarization modes of the solvent, m_i is the number of boson states associated to the i-th mode, the size of the basis becomes $n \prod_i^N m_i$

8: e. g. the solvent is accounted for as a continuum dielectric, its electronic polarization is modelled as a single harmonic mode, its dielectric response is condensed into one parameter ϵ_{opt}, etc...

description of solute and solvent becomes more detailed.[7]

To conclude this section, it must be noted that the non-adiabatic approach presented here does not account for the solvent as being strictly implicit. While certain aspects are omitted,[8] some knowledge of the solvent dielectric function is required. In other words, the non-adiabatic approach is more akin to full QM methods, where the solute together with a number of solvent molecules are treated at the QM level, than to implicit solvation methods.

1.4 The antiadiabatic approximation

While achieving numerically exact solutions to the solute-solvent problem is appealing, a true implicit solvation model is desired, that does not require a detailed description of the solvent leading at the same time to a more computationally manageable problem. In the following, the *antiadiabatic approximation* is adopted, where an instantaneous electronic polarization is assumed for the solvent, resonating in the UV, with respect to charge fluctuations in the solute, resonating in the visible region.

To proceed towards the antiadiabatic Hamiltonian, the effective electronic states are written according to first order perturbation theory:

$$|\tilde{f_i}\rangle = |f_i\rangle |0\rangle + \frac{g}{\hbar\omega_{el}} \sum_k \mu_{ik} |f_k\rangle |1\rangle \qquad (1.14)$$

where, in line with the antiadiabatic approximation, the coupling to states with more than a single oscillator quantum is neglected and molecular energies are disregarded with respect to $\hbar\omega_{el}$. The matrix elements of the antiadiabatic Hamiltonian are the matrix elements of the non-adiabatic Hamiltonian on the effective antiadiabatic states:

$$\langle \tilde{f_i}|\mathcal{H}|\tilde{f_j}\rangle = h_{ij} - 2\frac{g^2}{\hbar\omega_{el}} \sum_k \mu_{ik}\mu_{kj} + \frac{g^2}{\hbar^2\omega_{el}^2} \sum_{km} \mu_{ik}\mu_{jm} \langle 1|\langle f_m|\mathcal{H}|f_k\rangle|1\rangle$$
$$(1.15)$$

To calculate $\langle 1|\langle f_m|\mathcal{H}|f_k\rangle|1\rangle$, it is noted that the contribution from the interaction part in the Hamiltonian, $-g\hat{\mu}\left(\hat{b}^\dagger + \hat{b}\right)$ goes higher order and is neglected. The only relevant contribution is then $\langle 1|\langle f_m|\mathcal{H}_{gas}|f_k\rangle|1\rangle$. Off-diagonal elements are $\langle 1|\langle f_m|\mathcal{H}_{gas}|f_k\rangle|1\rangle = h_{mk}$, so that resulting corrections to the renormalized Hamiltonian are proportional to $\frac{g^2}{\hbar^2\omega_{el}^2}$ and therefore negligible in the $\hbar\omega_{el} \to \infty$ limit. Diagonal elements instead are $\langle 1|\langle f_m|\mathcal{H}_{gas}|f_m\rangle|1\rangle = h_{mm} + \hbar\omega_{el} \sim \hbar\omega_{el}$. Corresponding terms turn out proportional to $\frac{g^2}{\hbar\omega_{el}}$

and must be retained, leading to

$$\langle \tilde{f}_i | \mathcal{H} | \tilde{f}_j \rangle = h_{ij} - \frac{g^2}{\hbar \omega_{el}} \sum_k \mu_{ik} \mu_{kj} \qquad (1.16)$$

Having defined $g = \sqrt{\hbar \omega_{el} r_{el}/2}$, the above equation reduces to

$$\mathcal{H}_{\text{antiadiabatic}} = \mathcal{H}_{gas} - \frac{r_{el}}{2} \hat{\mu}^2 \qquad (1.17)$$

The antiadiabatic Hamiltonian is obtained via a perturbative expansion on $1/\omega_{el}$ and therefore is the exact Hamiltonian in the $\omega_{el} \to \infty$ limit, irrespective of the strength of the solute-solvent interaction.

1.4.1 Numerical evaluation of the antiadiabatic approximation

In the following Section, a few-state model (FSM) is defined and applied to a set of organic dyes (Figure 1.2) to numerically validate the antiadiabatic approximation.[9] First the comparison is made against the numerically exact non-adiabatic results. Then, approaches based on the adiabatic approximation to the electronic solvation, as implemented in quantum chemistry codes, are critically evaluated.

Comparison with the non-adiabatic approach

A few state model (FSM) is defined for the four molecules in Figure 1.2, following a similar procedure as in Ref. [10]. **DANS** and **RD** are polar dyes showing positive and negative solvatochromism, respectively.[7, 11] **Q1** and **Q2** are quadrupolar dyes: both have negligible polarity but **Q1**, of interest for non-linear optics, has a sizable transition dipole moment to the first excited state, while **Q2**, of interest for thermally-activated delayed fluorescence, has a negligible transition dipole moment.[12]

Gas phase density functional theory (DFT) is adopted to optimize each molecule in the ground state. On each equilibrium geometry, gas phase time-dependent DFT (TD-DFT) was run to obtain excited state properties.[9] The first three singlets (the ground state and the first two excited singlets) are selected as the molecular basis, so that the gas phase Hamiltonian, $\mathcal{H}_{gas}$, is diagonal, its matrix elements being the excitation energies of each singlet state (setting the energy of the ground state as zero).[10] The matrix elements of the main component of dipole moment operator (indicated by the

9: In this section, the CAM-B3LYP functional and the 6-31G(d) basis set are used for all DFT and TD-DFT calculations.[13]

10: Results in Figure 1.3 show that the results marginally depend on the truncation of the solute basis.
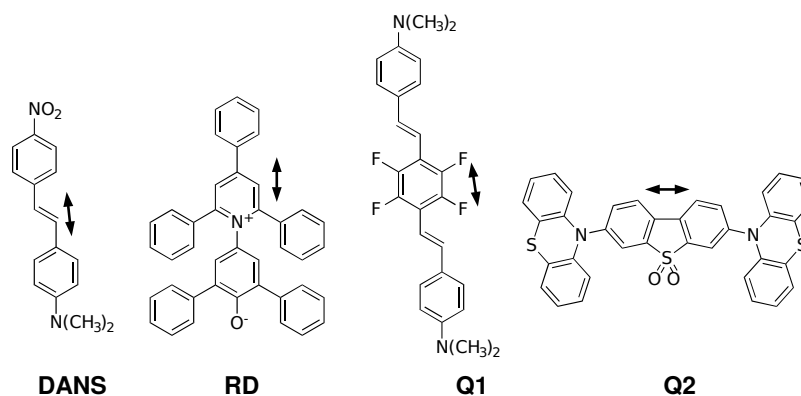
Figure 1.2: The molecules considered in Section 1.4.1: **DANS** (dimethylamino-nitrostylbene) and **RD** (the Reichardt dye) are dipolar dyes; **Q1** (a fluorinated bis-alkylaminos-tyryl derivative) and **Q2** (3,7-bis(10H-phenothiazin-10-yl)dibenzo[b,d]thiophene-S,S-dioxide) are quadrupolar dyes. Top: Kekulè structures. Bottom: optimized geometries (CAM-B3LYP/6-31G(d) level). The arrows mark the direction of the main component of the dipole moment operator.
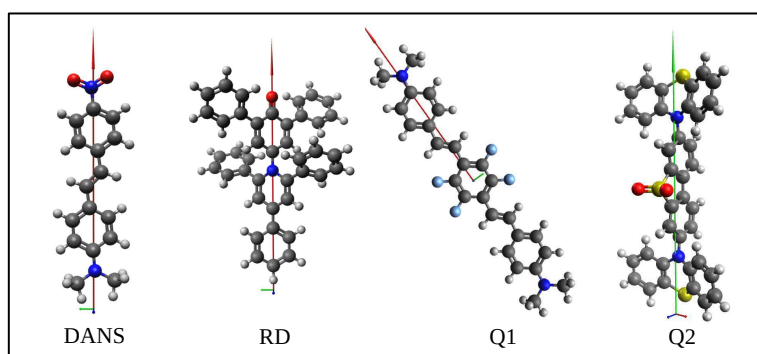
arrows in Figure 1.2) are calculated using the MULTIWFN software. Table 1.1 displays all parameters entering the FSM.

Figure 1.4 compares the molecular properties (excitation energy, transition dipole moment and, for dipolar dyes, ground state permanent dipole moment) calculated in the antiadiabatic approximation and upon exact diagonalization of the non-adiabatic Hamiltonian (Eq. 1.12), setting $\hbar \omega_{el} \sim 6\,\text{eV}$ or $20\,\text{eV}$ and accounting for three boson states. Molecular properties are plotted against $f\left(\epsilon_{opt}\right) = \left(\epsilon_{opt} - 1\right)/(2\epsilon_{opt} + 1)$, estimated for each molecule setting a to the relevant Onsager radius. The region corresponding to most organic solvents and amorphous matrices is in the $0.175 < f(\epsilon_{opt}) < 0.225$ range, as highlighted by the gray region in Figures 1.4, 1.5 and 1.6. Results in Figure 1.4 confirm that the antiadiabatic Hamiltonian in Eq. 1.17 represents the $\omega_{el} \rightarrow \infty$ limit of the non-adiabatic Hamiltonian in Eq. 1.12. Moreover, with the notable exception of **Q1**, results are marginally affected by the ω_{el} value, suggesting that the effective solvation model obtained imposing the antiadiabatic approximation is reliable even for solvents with comparatively low-energy excitations. Indeed, $6\,\text{eV}$ represents the absorption cutoff for most organic media, but absorption maxima are typically located at much higher energies. For **Q1**, a highly polarizable dye, the solute-solvent separation is more delicate and should be considered with care in largely polarizable environments.

The ground state dipole moment of the two polar dyes, **DANS** and **RD**, smoothly increases with $f\left(\epsilon_{opt}\right)$, due to the stabilization of polar states in condensed media. For **DANS**, a polar dye with a mostly neutral ground state, this implies an increase of the transition dipole moment and a decrease of the transition frequency, while the opposite occurs for **RD**, a dye with a mostly zwitterionic ground state. Quadrupolar dyes, **Q1** and **Q2**, have vanishing permanent dipole moment, but the solvent polarizability is responsible for a sizable decrease of the transition frequency.

Table 1.1: Molecular parameters entering the FSM

	DANS	RD	Q1	Q2
h_{11} (eV)	0.00	0.00	0.00	0.00
h_{22} (eV)	3.52	1.67	3.37	3.66
h_{33} (eV)	4.00	2.51	4.15	3.68
μ_{11} (D)	9.38	14.82	0.00	0.00
μ_{22} (D)	25.95	−3.75	0.00	0.00
μ_{33} (D)	5.75	3.45	0.004	0.00
μ_{12} (D)	9.64	6.55	14.08	0.00
μ_{13} (D)	−0.03	0.00	0.00	0.00
μ_{23} (D)	0.04	0.38	14.44	21.97
a (Å)	5.33	6.33	5.85	6.12

Comparison with adiabatic approaches

The adiabatic approximation, introduced in Section 1.1 to tackle orientational degrees of freedom of the solvent, is adopted in current implementations of effective solvation models to address electronic solvation as well. Under the adiabatic approximation, the kinetic energy term, T_{el} is neglected in eq. 1.12, so that the Hamiltonian acquires a parametric dependence on F_{el}, that in turn becomes a classical solvent mode.

For comparison purposes, the Hamiltonian in Eq. 1.12 is solved in the adiabatic approximation, adopting the same strategies as implemented in Gaussian16.[14–18]
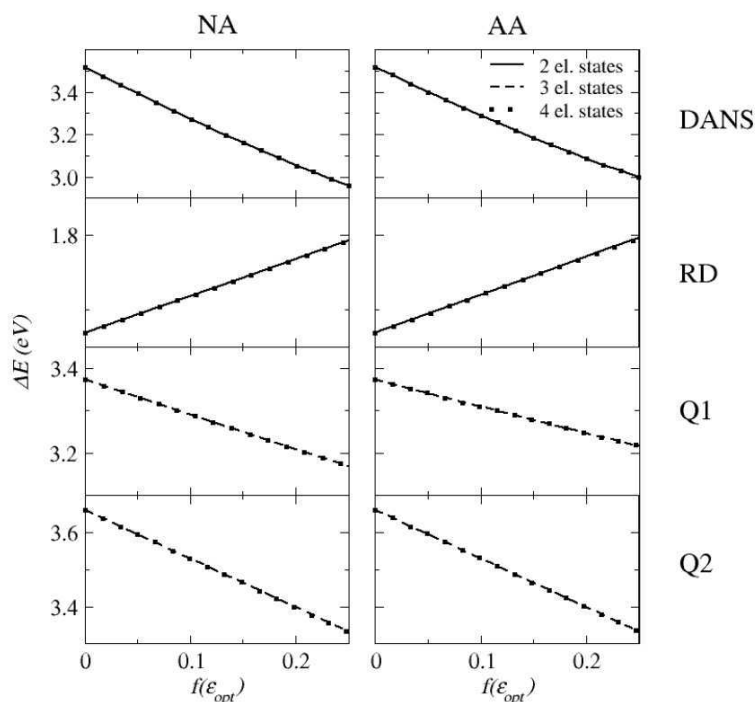
Figure 1.3: Comparing non-adiabatic (NA, left panels) and antiadibatic (AA, right panels) transition energies calculated in the FSM accounting for 2, 3 and 4 states. The 2-state results are not reported for **Q1** and **Q2**, since at least three states are needed to capture the physics of quadrupolar dyes.
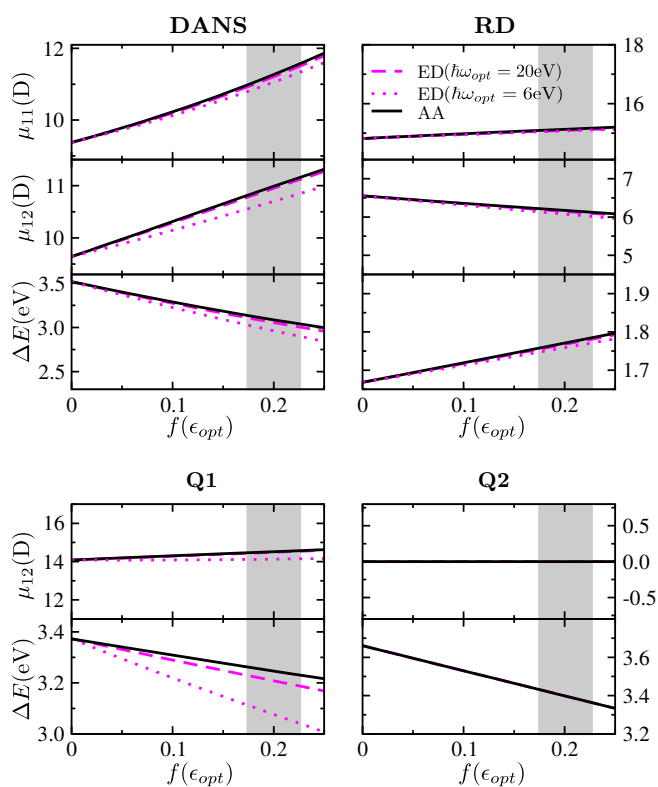

Figure 1.4: Validation of the antiadiabatic approach. Top panels: for the two polar dyes the ground state dipole moment μ_{11}, the transition dipole moment μ_{12} and the transition energy ΔE are reported vs $f(\epsilon_{opt})$. Bottom panels: for quadrupolar dyes the transition dipole moment μ_{12} and the transition energy ΔE are reported vs $f(\epsilon_{opt})$. Black lines refer to antiadiabatic results, magenta lines show exact diagonalization (ED) results obtained by diagonalization of the nonadiabatic Hamiltonian for $\omega_{el} = 6$ and 20 eV (dotted and dashed lines, respectively). For **Q2** all lines are superimposed. The shaded area marks the region where most organic solvents are located.

In PCM, the cavity occupied by the solute is formed as the super-position of interlocked spheres centered on the solute atoms, with radii close to the Van Der Waals radii. The surface is then subdivided in *tesserae* each bearing a partial charge. The solute-solvent interaction is electrostatic in origin and generates an intrinsically-self consistent problem, with the charge distribution of the solute polarizing the surrounding solvent and being in turn polarized by the solvent.[19]

When it comes to electronic transitions in solution, PCM accounts for the dynamical response of the solvent partitioning the apparent surface charges between a fast component, governed by the optical dielectric constant, and a slow component, governed by the static dielectric constant.

Several approaches have been proposed to address non-equilibrium solvation as relevant to electronic solvation. In this work, the linear response (LR), corrected linear response (CLR) and external iteration (EI) approaches available in the GAUSSIAN16 suite are discussed.[15, 17, 20] In all cases, a reference electronic state must be defined, that is self-consistently equilibrated to both fast and slow apparent surface charges. This state is selected as the ground state for absorption, or the lowest excited state for emission.

LR is arguably the most used approach, due to its simplicity. In LR, excitation energies are determined directly as singularities of the frequency-dependent linear-response functions of the solvated molecule in the ground state, avoiding explicit calculations of the excited state wavefunctions, leading to a fast and computationally convenient approach.[15] Specifically, defining the frozen-solvent transition energy as the transition energy calculated maintaining the fast and slow solvent degrees of freedom equilibrated to the reference state (the ground state for absorption, the excited state for emission), LR corrections are applied that only depend on the transition density between the reference and the final state. While computationally convenient, LR does not account for the variation of the charge distribution in the solute upon excitation, and therefore its use for CT transitions is not recommended.[16]

State-specific approaches were then proposed, accounting for the variation of the solute charge distribution upon excitation. Specifically, in EI, the fast degrees of freedom of the solvent are equilibrated to the excited state charge density, in a self-consistent procedure. The non-equilibrium transition energy is then computed as the difference between the energy of the final state and of the initial state, both states being obtained with the fast solvent degrees of freedom equilibrated to the relevant state (for polar solvents slow solvent degrees of freedom are maintained fixed to the equilibrium value for the ground state, when referring to

absorption processes, and to the excited state when referring to emission).[17] It is important to underline that in EI two different potentials for the ground and the excited states are considered in an effort to account for the fast relaxation of the solvent degrees of freedom. However, the approach is still strictly adiabatic, as each Hamiltonian is defined and diagonalized for a specific fixed potential. Moreover, since transitions are computed between eigenstates obtained from the diagonalization of different Hamiltonians, the calculation of fundamental spectroscopic properties such as the transition dipole moment is precluded.

CLR bridges the gap between LR and EI and represents a perturbative approximation to EI. As in LR, the zero-order transition energy is calculated as the frozen-solvent transition energy. Corrections are then applied that depend on the variation of the charge distribution upon excitation. According to Ref. [20], the correction is computed by considering the orbital response to the excitation of interest, in turn obtained as the solution of the Kohn–Sham Z-vector equations (relaxed density). CLR relies on a first order perturbative approach, so that corrections only apply to the energies, while wavefunctions are not affected. Transition dipole moments are therefore accessible and coincide with those obtained in LR. However, CLR represents just a linear perturbative approximation to the complete EI calculation, and, apart from computational convenience, it is unclear why a linear perturbative treatment should be preferred to a nominally exact calculation.

For the sake of comparison, the adiabatic calculation is set up for **DANS**, **RD**, **Q1** and **Q2**. The first step is the calculation of the ground state obtained upon diagonalization of the adiabatic Hamiltonian with F_{el} fixed at the ground state equilibrium. Top panels of Figure 1.5 compare the adiabatic and antiadiabatic estimates of the permanent dipole moments of **DANS** and **RD**. The permanent dipole moments of the quadupolar dyes, **Q1** and **Q2** are vanishing and therefore are not shown. The adiabatic approximation fails already in the calculation of the ground state. In particular, the adiabatic approximation underestimates the increase of the ground state dipole moment of **DANS** in condensed media. Indeed, the ground state dipole moment of **DANS** is smaller than its excited state dipole moment. The reaction field equilibrated at the ground state is therefore small and more polar states than the ground state are less stabilized in the adiabatic approximation than in the antiadiabatic approach where each state is stabilized by the interaction with its own reaction field. The opposite occurs for **RD**, whose dipole moment is larger in the ground than in the excited state.

Turning attention to spectral properties, in the LR approach[15] the transition energy is calculated from the vertical transition energy,

$\Delta E_{21}^{(0)}$ as follows:[16]

$$\Delta E_{21}^{LR} = \Delta E_{21}^{(0)} - r_{el}|\mu_{21}|^2 \qquad (1.18)$$

The LR transition energy in Figure 1.5 compares well with the antiadiabatic result only for **DANS**. In general, LR energies are not accurate since they do not account for the variation of the solute polarity upon excitation. To improve on LR, state specific approaches were introduced. Among them, the EI approach equilibrates the fast solvation field around the excited state and calculates the transition energy as the energy difference between the equilibrated excited and ground states (Figure 1.5). Calculated EI energies always deviate considerably from antiadiabatic results.[17] More fundamentally, EI suffers from a basic flaw when applied to fast solvation, since the optimized ground and excited states are eigenstates of two different adiabatic Hamiltonians, thus precluding the calculation of transition dipole moments. The CLR approach circumvents this problem only accounting for perturbative corrections to transition energies, while maintaining the wave funtions unperturbed.[20] In CLR the correction to the transition energy is proportional to the square of the variation of the dipole moment upon excitation:[16]

$$\Delta E_{21}^{CLR} = \Delta E_{21}^{(0)} - \frac{r_{el}}{2}\left(\mu_{22} - \mu_{11}\right)^2 \qquad (1.19)$$

The CLR estimate of the transition energies is good for the two polar dyes, whose solvatochromic shifts are governed by the variation of the molecular dipole moment upon excitation. Some amount of error cancellation on the ground and excited state permanent dipole moments enters into play here, since, as discussed above, the adiabatic estimate of the ground state dipole moment is poor.

Adiabatic approaches fail in the most striking way for the quadrupolar dyes, **Q1** and **Q2**. These dyes have a negligible polarity and therefore have vanishing CLR corrections. The sizable transition dipole moment of **Q1** leads to a sizable LR correction, largely deviating from antiadiabatic results. **Q2** instead has a negligible transition dipole moment, then for this dye both LR and CLR corrections vanish. Neither LR nor CLR reproduce the excited state stabilization of **Q2** due to the medium refractive index. The solvent polarizability stabilizes instantaneous charge fluctuations in the solute, an effect that cannot be appreciated in any adiabatic approach to fast solvation.

Figure 1.5: Adiabatic vs. antiadiabatic results. The same as in Figure 1.4 but comparing antiadiabatic results (black line) with adiabatic results (colored lines). The ground state dipole moment μ_{11} (red line with dots) is the same in all adiabatic implementations. The transition dipole moment μ_{12} is undefined in EI, and is the same for LR and CLR approaches. For transition energies, the dotted red lines show the vertical excitation energy, the continuous red lines show LR results, the continuous red lines with dots show CLR results, the blue line show the EI results. For **DANS**, LR and CLR energies are almost superimposed. For **Q1** the vertical excitation energy, CLR and EI energies are coincident. For **Q2** all adiabatic energies but EI are superimposed. The shaded area marks the region relevant for organic solvents and matrices.
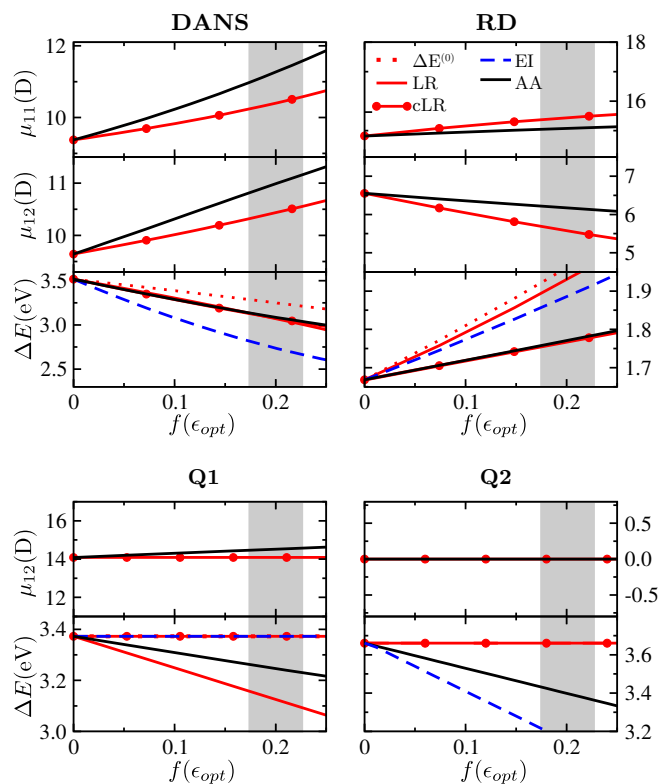
Validation of the adiabatic FSM

To validate the proposed FSM, adiabatic results, already reported in Figure 1.5, are compared with analogous results from TD-DFT calculations for solvated dyes adopting the adiabatic implementations of the *polarizable continuum model* (PCM) in GAUSSIAN16 (Figure 1.6).[16, 19] In order to only account for the effect of solvation, TD-DFT calculations are run for the dyes of interest keeping the molecular geometry fixed to the gas phase ground state geometry. Fictitious solvents with $\epsilon_{st} = \epsilon_{opt}$ are used, in order to avoid any effect due to solvent polarity. In analogy with Figure 1.5, results are plotted against $f(\epsilon_{opt})$.

Overall, the comparison between FSM and TD-DFT confirms that the adopted FSM captures the basic physics modelled by PCM for the systems of interest. The most interesting observation is that sizable CLR corrections to the transition energies of the two quadrupolar dyes are calculated in TD-DFT. Since **Q1** and **Q2** are nonpolar, these corrections are due to quadrupolar and higher order terms in the solute-solvent interactions, that are fully disregarded in the FSM. However, the important point here is not the quality of the dipolar approximation. The results presented here demonstrate that the adiabatic approximation fails in the most dramatic way to describe fast solvation as it cannot properly account for the first order (dipolar) corrections to the transition energy of nonpolar dyes.
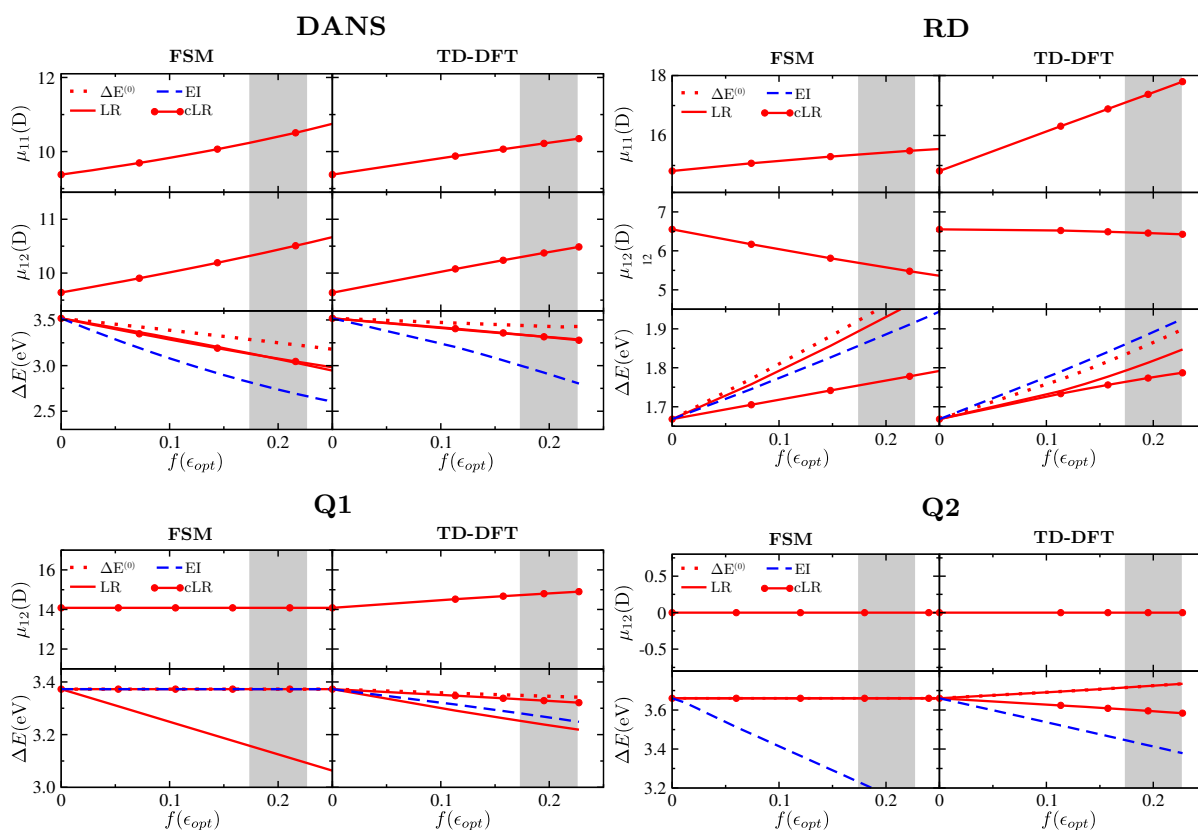
Figure 1.6: Adiabatic results for **DANS**, **RD**, **Q1** and **Q2**. Left panels: FSM results. Right panels: TD-DFT results.

1.5 Electronic solvation and the singlet-triplet gap

In this Section, the focus is on electronic solvation of emitters showing *thermally-activated delayed fluorescence* (TADF), a triplet harvesting phenomenon of great interest in the field of organic light-emitting devices that is discussed in greater detail in Chapter 2. The early chemical design of TADF emitters was focused on the minimization of the singlet-triplet gap, ΔE_{ST}, by space-separation of the HOMO and LUMO. To this aim, electron-donor and electron-acceptor moieties were connected in a twisted conformation.[21–24] The inherent synthetic flexibility of organic compounds makes it possible to synthesize a large collection of dyes, which differ not just in the nature of the donor and acceptor units but also in the ways these units are connected: other than dipolar emitters, quadrupolar and octupolar emitters have been synthesized and studied, as well as more exotic systems with through-space CT interaction.[24–27]

Quantum chemical calculations are a useful tool to explore this vast chemical space, allowing for a systematic *in silico* screening of a large amount of chemical structures to select a limited number of promising compounds to be subjected to detailed experimental
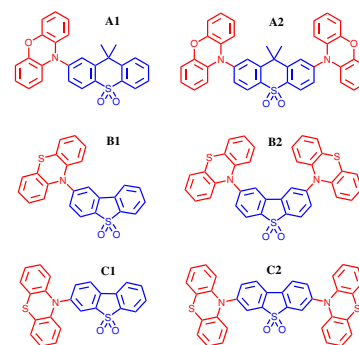

Figure 1.7: Molecules considered in this Section 1.5 (**A1**) PO-TXO2. (**A2**) DPO-TXO2. (**B1**) 2-PTZ-DBTO2. (**B2**) DPTZ-DBTO2. (**C1**) PTZ-DBTO2. (**C2**) 3,7-DPTZ-DBTO2. In all molecules, red and blue colors mark the electron donor and acceptor groups, respectively.

and theoretical characterizations. To this effect, cheap, fast, and reliable computational approaches are needed. TD-DFT arguably represents one of the most effective computational tools in this respect, thanks to the favorable trade-off between accuracy and computational cost. Once the proper functional is selected, reliable TD-DFT results can be obtained for isolated (gas phase) dyes, but material scientists need to address the properties of the dyes in condensed phases (either in solution or in a matrix). Implicit solvation models, like PCM or COSMO, are computationally inexpensive, but, as demonstrated in the previous section, adopt an adiabatic approximation for the electronic degrees of freedom of the solvent, leading to a proliferation of approximation schemes (LR, CLR and EI) and to somewhat unreliable results.[15, 17–19, 28]

In this section, with reference to TADF dyes, current implementations of continuum solvation models are discussed, showing that they do not properly address environmental effects on the singlet–triplet gap, with results that depend on the adopted approximation scheme and lead, in some cases, to an inversion of the order of the lowest singlet and triplet states.[29]

In particular, three dipolar emitters (**A1**, **B1** and **C1**) and their quadrupolar counterparts (**A2**, **B2** and **C2** respectively) are considered, as shown in Figure 1.7.[23–25] For each emitter, single point TD-DFT calculations on the optimized ground state geometry are performed to obtain excitation energies (in the Tamm-Dancoff approximation[30]),[31] both in gas phase and accounting for non-equilibrium solvation in PCM. The electronic nature of the states is evaluated using the natural transition orbitals (NTOs) associated to each transition. NTOs are collected in Appendix C.[11]

11: All DFT and TD-DFT calculations in this Section are performed using GAUSSIAN16.[14] The optimized ground state structures of **A2**, **B2** and **C2** are obtained at the B3LYP/6-31G(d) level. Ground state geometries for **A1**, **B1** and **C1** are obtained substituting one of the donor units with an hydrogen atom. TD-DFT calculations are performed at the M06-2X/6-31G(d) level imposing the Tamm-Dancoff approximation.

As discussed in Section 1.4, the ground state properties of the solute are not properly addressed when the adiabatic approximation is adopted to fast solvation. Since in current PCM implementations the ground state geometry is optimized in this approximation, leading to unreliable results, all data below are obtained for the optimized geometry in gas phase. Moreover, in order to exclude any contribution from polar solvation, custom non-polar solvents are considered, setting the static dielectric constant equal to the squared refractive index. Calculations are repeated for different values of the refractive index, η. Results (Figure 1.8 and Figure 1.11) are displayed as a function of $f(\eta^2) = (\eta^2 - 1)/(2\eta^2 + 1)$, the region corresponding to most organic solvents and polymeric hosts covering the $0.175 < f(\eta^2) < 0.225$ interval. The three approaches to non-equilibrium solvation discussed in Section 1.4.1 (LR, CLR and EI) are adopted to obtain transition energies to be compared with antiadiabatic results.
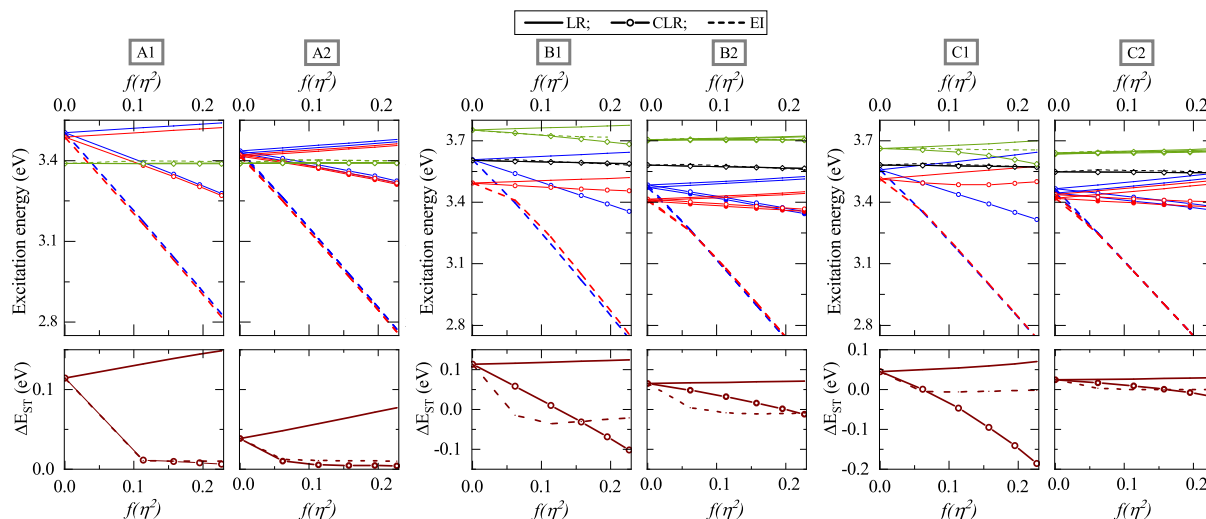
(a) A1 (left) and **A2** (right) **(b) B1** (left) and **B2** (right) **(c) C1** (left) and **C2** (right)

Figure 1.8: Top panels: excitation energies vs $f(\eta^2)$ for states ^{1}CT (blue), ^{3}CT (red), ^{3}LE$_A$ (black),^{3}LE$_D$ (green). Bottom panels: the calculated energy gap between the lowest singlet and triplet states. In all panels solid lines refer to LR, symbols refer to CLR, dashed lines refer to EI.

A1 and A2 dyes

A1 and **A2** are TADF emitters with dipolar (D-A) and quadrupolar (D-A-D) structure, respectively, where A is 9,9-dimethylthioxanthene-S,S-dioxide (TXO2) and D is the phenoxazine (PO) group. The optimized ground state structure has the D and A moieties almost orthogonal. Both **A1** and **A2** have a negligible permanent dipole moment. Figure 1.8a shows the $f(\eta^2)$-dependence of the transition energies for the first few excitations of both molecules, calculated in the different implementations of PCM, discussed above. The nature of each state is defined with reference to the natural transition orbital (NTO), displayed in Figure C.1 and C.3.

In gas phase, the lowest triplet excitation of **A1** at 3.389 eV is fully localized on the donor. The state, labeled ^{3}LE$_D$, has negligible permanent dipole moment. The second triplet at 3.487 eV and the lowest singlet at 3.504 eV are instead almost pure CT states, labeled ^{3}CT and ^{1}CT, respectively, and have a large permanent dipole moment oriented along the CT axis (see Table C.1). Increasing $f(\eta^2)$, LR excitation energies marginally increase due to the solvent stabilization of the ground state, without any significant effect on the energies of the excited states. CLR and EI give qualitatively different results than LR: indeed already in non-polar solvents both approaches point to a different nature of the lowest excited triplet that becomes a CT state rather than an LE state. This has enormous spectroscopic consequences,[32–34] and it is important to realize that LR, the default approach to solvation, gives the wrong order of excited states for TADF dyes. In fact, not accounting for the large

charge reorganization upon CT excitation, LR does not capture the large stabilization of CT states when going from gas-phase to condensed phases, leading to unreliable results already in non-polar media. On the other hand, CLR and EI lead to wildly different results, with energy differences ≈ 0.5 eV for typical $f\left(\eta^2\right)$ values for organic media. CLR and EI results for the energy gap between the lowest singlet and triplet states, ΔE_{ST}, are similar, even if largely different from the LR result.

In **A2**, the number of relevant excited states doubles with respect to **A1**, as symmetric and antisymmetric CT and LE_D states enter into play. In gas phase, the lowest triplets (≈ 3.39 eV) are two degenerate states localized on the donors, ^3LE_D, while CT states are at higher energies: a pair of almost degenerate triplets, ^3CT, at ≈ 3.42 eV and a pair of singlets, ^1CT, at 3.428 eV and 3.436 eV. Despite the different structure and higher number of excited states, the dependence of LR, CLR and EI transition energies on $f(\eta^2)$ (Figure 1.8a, right panel) can be explained in a similar way as for **A1**, with the caveat that EI and CLR corrections are due to the variation of the molecular quadrupolar moment of **A2** upon excitation. Once again, ΔE_{ST} results from CLR and EI calculations are similar but largely different from LR results.

B1, B2, C1 and C2

B1 and **B2** have been extensively studied both from a theoretical and experimental perspective.[32, 33] The D and A units (phenothiazine, PTZ, and dibenzo[b,d]thiophene 5,5-dioxide, DBTO, respectively) are connected as shown in Figure 1.7. In the optimized ground state, D and A moieties lie on nearly orthogonal planes. Results for **B1** and **B2** are displayed in Figure 1.8b. Several states must be considered for these systems. In fact the gas phase NTO and MO analysis (Figure C.4 and C.5) reveals that **B1** lowest triplet (3.493 eV) has a predominant CT character, so that it is dubbed ^3CT, but with a non-negligible contribution from a local excited state. The next triplet, ^3LE_A, at 3.604 eV, is almost entirely localized on the acceptor unit. The lowest singlet state at 3.607 eV, ^1CT, is a pure CT state, with a large permanent dipole moment aligned approximately along the DA axis. The third triplet at 3.753 eV is a localized excited state on the D unit, ^3LE_D state, with a non-negligible CT character. As before, the LR corrections to the excitation energies are minor for all states, in view of the very small transition dipole moments of relevant excitations. On the opposite, CT states are largely stabilized in CLR and EI but, as before, the two approaches yield very different results.

B2 is the quadrupolar counterpart of **B1** and more states enter into play. However, the nature and relative energies of the states in gas

phase is similar in **B1** and **B2**. The lowest triplets (≈ 3.41 eV) are mostly ^{3}CT, but have a non-negligible LE component, as shown from the NTO analysis (Figure C.6). Interestingly, the low energy triplet in **B2** has a larger CT character than in **B1**. The next triplet at 3.580 eV is localized on the acceptor. The pair of degenerate ^{3}LE$_D$ states at ≈ 3.70 eV has a non-negligible CT component. The lowest singlets, ^{1}CT, at 3.473 eV and 3.484 eV are essentially pure CT states.

As already discussed, LR corrections are negligible due to the very small transition dipole moments in TADF dyes. In CLR, corrections to the ^{3}LE$_A$ and ^{3}LE$_D$ states are also negligible. On the other hand, ^{3}CT and ^{1}CT states are stabilized as the transitions occur with a significant change in the charge distribution. However, another serious problem emerges: both CLR and EI show an inversion in the order of the lowest singlet and triplet states. In other terms, according to these calculations, the lowest excited state of both **B1** and **B2** dissolved in an organic non-polar medium would correspond to a singlet and not to a triplet state. As discussed below, this result originates from the mishandling of fast solvation. In **B1**, the lowest triplet has dominant CT character but with a sizable contribution from the triplet excitation localized on the acceptor, while the lowest singlet state is an almost pure CT state. The variation of the charge distribution upon excitation is therefore larger for the lowest singlet than for the lowest triplet excitation, leading to a larger stabilization of the singlet state with respect to the triplet state, with an effect that is most apparent in CLR. Indeed, in CLR the nature of the states is frozen, while in EI the nature of the states changes in the iterative process. Specifically, in our case, during the EI iterations the weight of the LE component in the lowest triplet state decreases, reducing ΔE_{ST}, that stays small but negative. In any case, the three implementation of the solvation model lead to very different values for ΔE_{ST}. Due to the larger CT component in ^{3}CT states in **B2** with respect to the same state in **B1**, the singlet-triplet inversion occurs at larger $f\left(\eta^2\right)$ values.

C1 and **C2** are very similar to **B1** and **B2**, respectively, as they share the same D and A units, even if connected in a different way. Result in Figure 1.8c are interpreted in the same way as for **B1** and **B2**. NTOs (see Figure C.7 and C.9) show a smaller mixing of local and CT triplet states than observed in **B1**/**B2**. Accordingly, for both **C1** and **C2**, ^{3}CT states have a larger weight of CT character than for **B1** and **B2**, resulting in larger charge separation. However, negative ΔE_{ST} are observed again with most prominent effects in CLR.

Figure 1.9: Antiadiabatic transition energies of excited singlet (black) and triplet (red) states of **B1** as a function of $f\left(\eta^2\right)$. The three panels refer to results obtained truncating the electronic basis to the first (a) 10 singlet and 10 triplet states; (b) 10 singlets and 20 triplets; (c) 17 singlet and 26 triplets.
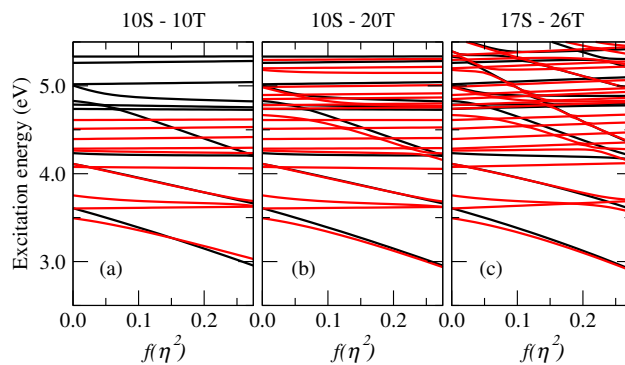
The FSM approach

The scattering of the results obtained in the three current PCM implementations available in GAUSSIAN16 package, the impossibility to calculate the transition dipole moment in the formally exact EI approach, addressed by limiting the analysis to first order perturbation theory in CLR, clearly point to some fundamental problem in solvation models, that can be traced back to the adiabatic approximation, as discussed in Ref. [9] and in section 1.4.1. To demonstrate that also the singlet-triplet inversion calculated in CLR and EI for some dyes in non-polar solvents is a spurious result of the adiabatic approach to fast solvation, the **B1** dye is selected as a model system to compare adiabatic and antiadiabatic results.

To address the antiadiabatic problem the same FSM approach is adopted as described in Section 1.4. Specifically, the Hamiltonian in Eq. 1.17 is written on the basis of the eigenstates of the gas-phase Hamiltonian, as obtained from TD-DFT calculations. The matrix elements of the dipole moment operator on the same basis are extracted using the MULTIWFN software.[12]

12: Specifically, spin-orbit coupling is neglected and the independent spin subspaces, formed by the first n singlets and m triplets, are obtained from the TD-DFT calculation for the gas-phase molecule.
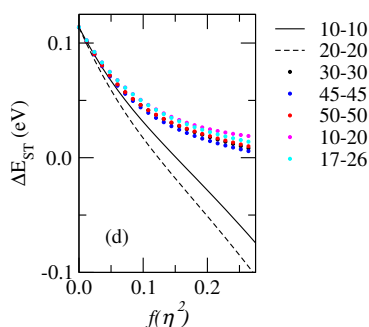
Results of course depend on the number of states included in the basis sets and, since the diagonalization is performed independently in the singlet and triplet subspaces, it is important to consistently choose the number of states in the two subspaces. Setting the same number of states in both subspaces (see Figure 1.9 and Figure 1.10) gives rise to the crossing of singlet and triplet states. The reason for this result is easily recognized in a basis that spans a much wider energy interval for the singlet vs the triplet subspace. Increasing the number of triplet states, so that the same energy window is roughly spanned in both subspaces, leads to more reliable results. Data in Figure 1.9 and Figure 1.10 show that spanning a range of $\sim 6\,\text{eV}$ with 17 singlets and 26 triplets leads towards convergence.

Figure 1.10: Antiadiabatic ΔE_{ST} as a function of $f\left(\eta^2\right)$ for different number of excited singlet and triplet states as denoted in the legend.

Right panels of Figure 1.11 collect antiadiabatic results for **B1**, obtained setting the cavity radius to the Onsager's radius, $a = 5.44\,\text{Å}$. These results clearly point to an excitation spectrum where
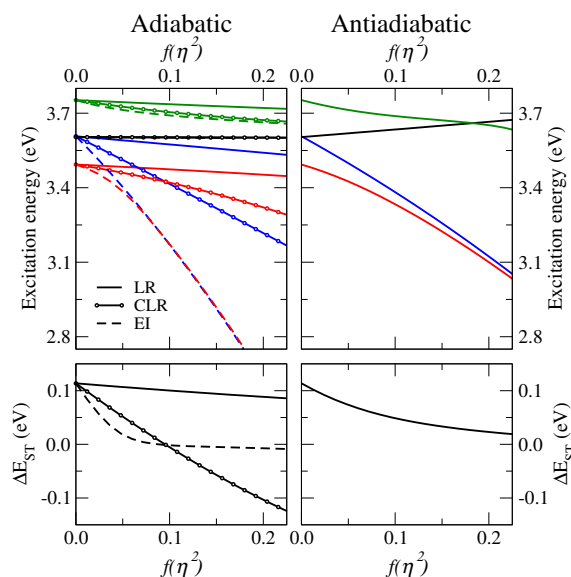
Figure 1.11: Comparison between adiabatic and antiadiabatic results (left and right panels, respectively) for **B1** in the few state model accounting for 17 singlet and 26 triplet states. Top panels: Calculated excitation energies vs $f(\eta^2)$ for states ^{1}CT (blue), ^{3}CT (red), ^{3}LE$_A$ (black), ^{3}LE$_D$ (green). Bottom panels: the calculated energy gap between the lowest singlet and triplet states. In left panels (adiabatic results) solid lines refer to LR, symbols refer to CLR, dashed lines refer to EI.

the transition energies for the state with CT character (either singlet or triplet) are lowered due to the medium polarizability while LE states are less affected. As expected, LR results are completely off for CT states. On the other hand, EI largely overestimates the stabilization of CT states and CLR underestimates it (cf. Figure 1.8b). At variance with EI and CLR, antiadiabatic results point to a normal order of excited states, with the lowest being a triplet.

Comparing antiadiabatic results in the right panels of Figure 1.11 with PCM results in Figure 1.8b may however be misleading due to the approximations introduced to build the FSM adopted to run antiadiabatic calculations. For a more stringent comparison of antiadiabatic and adiabatic approximations, left panels of Figure 1.11 show results obtained in the adiabatic approximation, and specifically in its LR, CLR and EI variants, as done in Section 1.4.

The first observation is that adiabatic results in Figure 1.11 compare favourably with PCM results in Figure 1.8b, suggesting that the adopted approximations capture most of the relevant physics. More important is however the comparison between adiabatic and antiadiabatic results in Figure 1.11, relevant to the same model. Solvation effects on LE states are marginal, but, as for CT states, neither EI nor CLR properly capture the stabilization of either the singlet or triplet states with differences in the estimated transition energies of several tenths of eV at $f(\eta^2) \sim 2$, as relevant to common organic media. Moreover, the antiadiabatic singlet-triplet gap decreases considerably as a result of the medium polarizability, but at variance with CLR and EI results, it stays positive. Quite irrespective of the quality of the proposed molecular model, results in Figure 1.11 unambiguously demonstrate that the adiabatic approach, when applied to describe the spectroscopic effect of the medium polarizability, leads to unreliable results.

1.6 Essential state models

Essential-state models (ESM) are a family of parametric Hamiltonians, that offer a reliable theoretical tool to address optical properties of π-conjugated dyes, whose low-energy photophysics is governed by charge-transfer (CT) transitions. In the ESM framework, CT dyes are described in terms of electron donor (D) and electron acceptor (A) groups linked by π-conjugated bridges. Accordingly, the minimal electronic basis is obtained from the main charge resonance structures.

Minimal models for CT interactions date back to the 50s, when Mulliken proposed a two-state model to describe the optical properties of CT complexes of benzene and iodine in solution.[35] The same model is at the core of Marcus theory for electron transfer.[36] More recently, ESMs have been developed to describe dipolar, quadrupolar and octupolar CT organic dyes, where electron donor and electron acceptor moieties are connected by a π-conjugated bridge.[12, 37–40] The coupling with nuclear degrees of freedom and the effect of polar solvation can be accounted for in a straightforward way to describe the linear and non-linear optical properties of these dyes.[37, 41] Moreover ESM offer a solid basis to address aggregation, energy transfer and relaxation dynamics in real-time.[11, 42–44]

In the following section, ESMs are adopted to critically address the effect of different theoretical approaches to electronic solvation.[45] In Chapter 2, the two-state model for push-pull chromophores will be extended to tackle the photophysics of thermally-activated delayed fluorescence emitters, where triplet states, conformational degrees of freedom and the surrounding environment play a pivotal role.
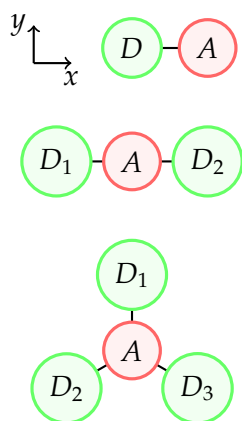
1.6.1 Essential State Models for multipolar dyes

In this subsection the ESMs for dipolar, quadrupolar and octupolar π-conjugated chromophores (Figure 1.12) are described, addressing the electronic problem and then extending the Hamiltonian to account for molecular vibrations and solvation, using the models discussed in Section 1.4. In Subsections 1.6.2, 1.6.3, 1.6.4, electronic solvation of dipolar, quadrupolar and octupolar chormophores, respectively, is discussed in detail.

The minimal basis for ESM is built from states that correspond to the main charge resonance structures of the chromophore: one neutral state, $|N\rangle$, and one zwitterionic state per each molecular branch, $|Z_i\rangle$, where i counts the molecular branch. In quadrupolar and octupolar dyes, the molecular branches are equivalent and

Figure 1.12: Sketch of the structures of dipolar, quadrupolar and octupolar π-conjugated chromophores. The sketch for quadrupolar and octupolar chromophores with electron-donating core and electron-accepting outer groups are not shown.

the zwitterionic states are degenerate, separated from $|N\rangle$ by a gap of $2z$ and each coupled to $|N\rangle$ through the hopping integral τ.[46][13]

The electronic Hamiltonian is given by

$$\hat{\mathcal{H}} = 2z\hat{\rho} - \tau\hat{\sigma} \tag{1.20}$$

where the ionicity and hopping operators, $\hat{\rho}$ and $\hat{\sigma}$ respecively, are defined as

$$\hat{\rho} = \sum_{i}^{n} |Z_i\rangle \langle Z_i| \tag{1.21}$$

$$\hat{\sigma} = \sum_{i}^{n} |Z_i\rangle \langle N| + h.c. \tag{1.22}$$

where i runs on the n molecular branches. The electronic properties of the dye are fully determined in terms of the *ionicity*, defined as the expectation value of $\hat{\rho}$ on the ground state:

$$\rho = \frac{1}{2}\left(1 - \frac{z}{\sqrt{z^2 + n\tau^2}}\right) \tag{1.23}$$

The ionicity measures the degree of charge separation and the dipolar, quadrupolar or octupolar character of a chromophore in its ground state.

In order to address spectroscopy, the dipole moment operator, $\hat{\mu}$, is defined on the diabatic basis assuming that the only sizeable term is the dipole moment of the zwitterionic states, μ_0. In the reference frame defined in Figure 1.12, the dipole moment operator for different structures reads

$$\begin{array}{llllr} \hat{\mu}_x = \mu_0\hat{\rho} & \hat{\mu}_y = 0 & \hat{\mu}_z = 0 & \text{dipolar} & (1.24) \\ \hat{\mu}_x = \mu_0\hat{\delta} & \hat{\mu}_y = 0 & \hat{\mu}_z = 0 & \text{quadrupolar} & (1.25) \\ \hat{\mu}_x = \mu_0\hat{\delta}_x & \hat{\mu}_y = \mu_0\hat{\delta}_y & \hat{\mu}_z = 0 & \text{octupolar} & (1.26) \end{array}$$

where for quadrupolar chromophores the auxiliary operator is[12]

$$\hat{\delta} = |Z_1\rangle \langle Z_1| - |Z_2\rangle \langle Z_2| \tag{1.27}$$

Analogously, for octupolar chromophores the auxiliary operators are[47]

$$\hat{\delta}_x = \frac{\sqrt{3}}{2}\left(|Z_2\rangle \langle Z_2| - |Z_3\rangle \langle Z_3|\right) \tag{1.28}$$

$$\hat{\delta}_y = -|Z_1\rangle \langle Z_1| + \frac{1}{2}\left(|Z_2\rangle \langle Z_2| - |Z_3\rangle \langle Z_3|\right) \tag{1.29}$$

The auxiliary operators measure the charge unbalance in symmetric structures.

13: The minimal basis used in ESM corresponds to the *diabatic* basis, that is composed of states with a definite electronic character. For the sake of generality, the basis used in this subsection is *unsymmetrized*. Using a *symmetrized* basis is convenient (and elegant) when dealing with quadrupolar and octupolar chromophores, revealing which states couple under the action of the Hamiltonian, and whether the transition between the eigenstates are optically allowed or forbidden.

The coupling between electronic and nuclear motion strongly affects optical properties of π-conjugated chromophores, and is the origin of the vibronic structure of optical spectra, of the Stoke's shift, and of relaxation phenomena and symmetry breaking in quadrupolar and octupolar structures. In ESMs, one effective molecular coordinate per molecular branch is taken into account.[37] Assuming displaced harmonic potentials with the same force constant for each diabatic state (linear electron-vibration coupling), the vibrational Hamiltonian reads

$$\hat{\mathcal{H}}_v = -\sqrt{2\epsilon_v}\omega_v \sum_{i=1}^{n} \hat{q}_i \left|Z_i\right\rangle \left\langle Z_i\right| + \frac{1}{2} \sum_{i=1}^{n} \left(\omega_v^2 \hat{q}_i^2 + \hat{p}_i^2\right) \quad (1.30)$$

where ω_v is the frequency associated to the vibrational modes, ϵ_v is the vibrational relaxation energy and $\hat{p}_i$ is the conjugated momentum to $\hat{q}_i$ mode. Vibrational modes are treated as quantum coordinates in a non-adiabatic approach. In second quantization:

$$\hat{q}_i = \sqrt{\frac{\hbar}{2\omega_v}} \left(\hat{a}_i^\dagger + \hat{a}_i\right) \quad (1.31)$$

$$\hat{p}_i = i\sqrt{\frac{\hbar\omega_v}{2}} \left(\hat{a}_i^\dagger - \hat{a}_i\right) \quad (1.32)$$

where $\hat{a}_i^\dagger$ ($\hat{a}_i$) is the bosonic creation (annihilation) operator acting on the states of the i-th oscillator.

The coupled electron-nuclear problem is then solved writing and diagonalizing the total Hamiltonian on the basis spanned by the product of the electronic and vibrational basis. To this aim, the vibrational basis must be truncated to a sufficiently large number M of vibrational states to achieve convergence of the properties of interest, yielding a nM^n-dimensional basis.[14] The diagonalization of the non-adiabatic Hamiltonian yields the numerically exact vibronic eigenstates. Permanent and transition dipole moments are computed rotating on the eigenstate basis the dipole moment operator written on the diabatic basis, allowing the calculation of absorption and emission spectra using the procedure described in Appendix A. In particular, the absorption spectrum is computed assuming that only the lowest vibronic eigenstate is populated at ambient temperature, while the emission spectrum is computed assuming that only the lowest vibronic eigenstate of the excited state manifold, i.e. the Kasha's state, is populated, implicitly considering that the internal conversion rate is much faster than the emission rate.

14: Generally, reaching convergence in optical spectra requires $M \sim 10$.

Interaction with the dielectric solvent is accounted for in the reaction field approach discussed in Section 1.2.[48] The reaction field couples to the dipole moment operator, therefore only one of

its components must be taken into account for linear chromophores (dipolar and quadrupolar), co-linear with the CT direction. Two components must be taken into account for octupolar dyes, as shown in Figure 1.12.

The antiadiabatic correction, which introduces two-electron integrals, has a very simple form and a clear physical meaning in ESM. Indeed, for dipolar, quadrupolar and octupolar dyes one finds that $\hat{\vec{\mu}}^2 = \mu_0^2 \hat{\rho}$ and the electronic solvation Hamiltonian in the antiadiabatic approximation (eq. 1.17) reads

$$\hat{\mathcal{H}}_{el} = -\epsilon_{el}\hat{\rho} \qquad (1.33)$$

where $\epsilon_{el} = \mu_0^2 r_{el}/2$ is the electronic solvent relaxation energy, which measures the amount of energy gained by the system in a zwitterionic state due to the relaxation of the electronic clouds of the solvent molecules. In other words, when going from gas phase to solution, the energy of the zwitterionic states, $2z$, is renormalized by the electronic solvent relaxation energy, so that $z \rightarrow z - \epsilon_{el}/2$. This result is general as it does not depend on the solvation model, aside from the dipolar approximation. Eq. 1.7 can be used to relate ϵ_{el} with the refractive index of the solvent in the assumption of a spherical cavity. Due to the small variability of refractive indices in typical liquid organic solvents used in UV-vis spectroscopy, the relevant range of ϵ_{el} values is narrow, and antiadiabatic corrections are generally accounted for intrinsically in the z parameter when ESMs are parametrized against experimental spectra.

The adiabatic approximation is adopted to treat orientational solvation, neglecting the kinetic energy operators associated to the components of the orientational field. The orientational solvation Hamiltonian reads

$$\hat{\mathcal{H}}_{or} = \sum_{\alpha=1}^{3} F_{or,\alpha} \frac{\hat{\mu}}{\mu_0} + \sum_{\alpha=1}^{3} \frac{F_{or,\alpha}^2}{4\epsilon_{or}} \qquad (1.34)$$

where the sums run on the $N_\alpha = x, y, z$ components of the reaction field (effectively one component for linear chromophores and two for octupolar chromophores), and the dipole moment μ_0 has been collapsed into F_{or}, so that the reaction field is expressed in energy units.

In the adiabatic approximation, F_{or} is a classical coordinate, so that the total Hamiltonian is diagonalized for different values of F_{or}. The energy of the electronic (or vibronic) states depends on F_{or}, defining the so called potential energy surfaces (PES). For each F_{or} value, the matrix elements of the molecular Hamiltonian are renormalized according to eq. 1.34, and all the properties relevant to spectroscopy, such as the permanent dipole moments and the transition dipole moments, are computed rotating on

the adiabatic basis the relevant operators written on the diabatic basis. For a given vibronic eigenstate, the minimum in the F_{or}-dependent PES is the equilibrium position. In macroscopic samples, thermal fluctuations create a distribution of F_{or} values around the equilibrium position, so that the properties originate from a Boltzmann distribution of chromophores in equilibrium with the solvent molecules that surround them, and can be effectively computed as thermal averages over the population of the relevant electronic (or vibronic) state of the solute.

Absorption spectra are computed for each value of F_{or}, assuming that only the lowest vibronic state is populated at ambient temperature. The total absorption spectrum is then obtained weighting the F_{or}-dependent spectra by the thermal distribution of the lowest vibronic eigenstate. Analogously, emission spectra are computed for each value of F_{or}, assuming that only the lowest vibronic eigenstate of the excited state manifold (i.e. the Kasha's state) is populated at ambient temperature. The total emission spectrum is then obtained weighting the F_{or}-dependent emission spectra by the thermal distribution of the Kasha's state.

Since ϵ_{or} enters eq. 1.34 as the inverse force constant of the restoring harmonic potential, broader thermal distributions are expected as the polarity of the solvent increases, leading to inhomogeneous broadening of absorption and emission spectra. Moreover, for different values of ϵ_{or}, different equilibrium positions along F_{or} may be obtained for the ground and the emissive (Kasha) states, giving rise to solvatochromism. In symmetric systems, such as quadrupolar and octupolar chromophores polar solvation can drive symmetry breaking.[12] In the following subsections, electronic solvation is discussed and purely non-polar solvents are taken into account, effectively neglecting orientational degrees of freedom of the solvent. However, notions related to polar solvation are useful to understand the effect that an adiabatic treatment has on the system when electronic degrees of freedom are mistakenly treated with the same approximation as orientational degrees of freedom, i.e. under the adiabatic approximation.

1.6.2 Two-state model for dipolar dyes

Neglecting electron-vibration coupling ($\epsilon_v = 0$ in eq. 1.30), the molecular properties of polar D–π–A dyes only depend on the z/τ ratio. In the following sections, units are used so that $\hbar = 1$ and τ is set as the energy unit. The actual τ value for most CT dyes is in the order of $1\,\text{eV}$, even if for dyes of interest for thermally activated delayed fluorescence, the typical τ values are one order of magnitude smaller. All properties of interest can be expressed as a function of ρ, the ground state ionicity (eq. 1.23). The transition

dipole moment, $\mu_{CT} = \sqrt{\rho(1-\rho)}$, shows a maximum at $\rho = 0.5$. The transition frequency is $\omega_{CT} = \tau/\sqrt{\rho(1-\rho)}$, showing a minimum at $\rho = 0.5$. The ground state permanent dipole moment is $\mu_g = \mu_0\rho$ and the excited state one is $\mu_\varepsilon = \mu_0(1-\rho)$. The mesomeric dipole moment, $\mu_\varepsilon - \mu_g = \mu_0(1-2\rho)$, is positive for mostly neutral dyes ($\rho < 0.5$) and negative for mostly zwitterionic dyes ($\rho > 0.5$). Accordingly, mostly neutral dyes show a normal solvatochromic behavior (the absorption band redshifts upon increasing the solvent polarity), while mostly zwitterionic dyes show inverse solvatochromism (the absorption band blueshifts upon increasing the solvent polarity), so that simple spectroscopic data allow to discriminate between the two classes of polar dyes.

Figure 1.13 shows results for a mostly neutral dye ($z = 0.75$, corresponding to $\rho_{gas} = 0.2$) and a mostly zwitterionic dye ($z = -0.75$, $\rho_{gas} = 0.8$). The analytic results for the purely electronic model ($\epsilon_v = 0$) in panels a–c and f–h show the evolution of the molecular properties when ϵ_{el} increases from 0, as relevant to the gas phase, to larger values, typical of organic media. In all cases, the ionicity ρ increases with ϵ_{el}, as a result of the stabilization of charge-separated states by the electronic polarizability of the environment. The adiabatic results (blue lines in Figure 1.13) show sizable deviation from the antiadiabatic results (black curves), but the most clear failure of the adiabatic approach is recognized in having two different sets of results, corresponding to the two different adiabatic Hamiltonians obtained upon fixing the reaction field to the equilibrium value for the ground state (blue continuous lines) or for the excited state (blue dotted lines). This is clearly unphysical, since the electronic clouds of the solvent molecules readjust quickly (instantaneously in the antiadiabatic limit) to the charge reorganization in the solute. In any case, taking the adiabatic results at face value, one should use the adiabatic Hamiltonian with F_{el} equilibrated to the ground state or to the excited state to simulate absorption or fluorescence processes, respectively. A spurious red-shift of the fluorescence band with respect to the absorption band would then be observed.

Current implementations of continuum solvation models in quantum chemical packages recognize the problem and address the fast nature of electronic solvation imposing that the fast component of the reaction field F_{el} is instantaneously equilibrated to each state. Accordingly, absorption and fluorescence involve the same two states: the ground state obtained diagonalizing the adiabatic Hamiltonian with F_{el} equilibrated to the ground state, and the excited state obtained diagonalizing the adiabatic Hamiltonian with F_{el} equilibrated to the first excited singlet. Along these lines, the spurious adiabatic Stokes shift disappears but another major problem arises as optical transitions are calculated between two

states obtained from the diagonalization of two different adiabatic Hamiltonians. The unphysical nature of this approach is best demonstrated in the so-called state-specific implementations of continuum solvation models where the calculation of transition dipole moments, and hence of spectral intensities, is impossible. This issue is circumvented in the perturbative CLR approach (corrected linear response approach) that adopts first-order perturbation theory to correct the state energies, leaving the wavefunctions unaffected. However, a perturbative treatment definitely represents a low-quality approach, if compared with the formally exact adiabatic results of the state-specific approach. More generally, the major issue of current implementations of solvation models, relying on the adiabatic treatment of fast degrees of freedom, cannot be relieved by degrading the results via a low-order perturbative approach.

To address vibronic bandshapes in ESMs, electron-vibration coupling is accounted for in a non-adiabatic calculation. Specifically, the molecular Hamiltonian (modified as in eq. 1.33 to account for fast solvation in the antiadiabatic limit, or account for the static corrections due to the equilibrated F_{el} in the adiabatic limit) is solved by writing the corresponding matrix on the basis defined as the direct product of the electronic basis states times the eigenstates of the harmonic oscillator(s) in the last term of eq. 1.30. Of course, the vibrational basis is truncated to a large enough number of vibrational states as to obtain convergence. Once the molecular Hamiltonian is diagonalized, the absorption and fluorescence spectra are calculated from the transition energies and transition dipole moments assigning each vibronic transition a Gaussian lineshape with a fixed linewidth (in this work it is set to 0.04), as explained in the previous section and in Appendix A. In the antiadiabatic approach to fast solvation, the eigenstates obtained upon diagonalization of a single effective Hamiltonian enter the calculation of both the absorption and fluorescence spectra. On the other hand, in the adiabatic approach to fast solvation, two different Hamiltonians with F_{el} equilibrated either to the ground or to the excited state are used for the calculation of the absorption and fluorescence spectra, respectively. As shown in Figure 1.13, the rightmost panels relevant to each dye show an example of vibronic bandshapes calculated for the absorption and emission spectra setting $\epsilon_v = 0.3$. Since band shape are to be compared, all normalized spectra are translated to set the origin of the energy axis at the 0–0 transition energy. The calculated absorption and fluorescence bandshapes in the adiabatic approximation for fast solvation are marginally different from the antiadiabatic results.

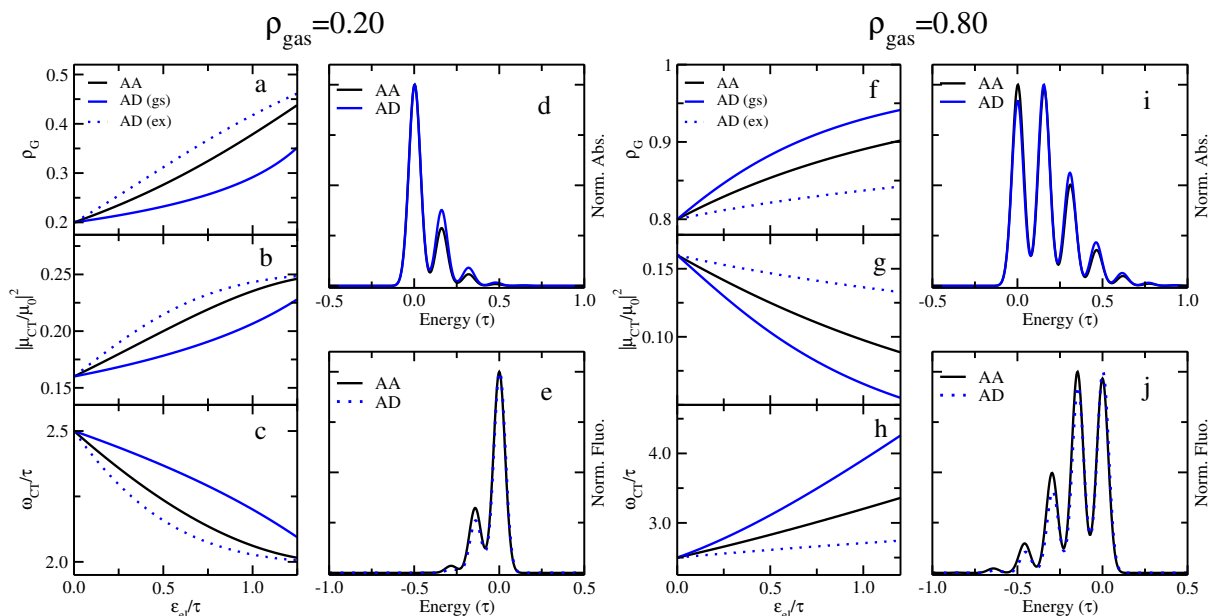### 1.6.3 Quadrupolar dyes and symmetry-breaking

Figure 1.13: Fast solvation effects on the properties of polar chromophores with $\rho_{gas} = 0.2$ (left side) or $\rho_{gas} = 0.8$ (right side). On each side, right panels show properties (ground-state ionicity, transition dipole moment, transition frequency) as a function of ϵ_{el} for a system with $\epsilon_v = 0$. The right panels show vibronic bandshapes calculated for a system with $\tau = 0.3$ and $\epsilon_v = 0.32$. Antiadiabatic (antiadiabatic) results: black lines; Adiabatic (AD) results with F_{el} equilibrated with the ground state (full blue lines) or with the optically-allowed excited state (dotted blue lines)

Symmetry is exploited to address the electronic problem of quadrupolar dyes, combining the two degenerate basis states $|Z_1\rangle$ and $|Z_2\rangle$ as $|Z_\pm\rangle = (|Z_1\rangle \pm |Z_2\rangle)/\sqrt{2}$. The mixing between $|Z_+\rangle$ and $|N\rangle$ results in a ground state $|\mathcal{G}\rangle$ and an excited state $|\mathcal{E}\rangle$. The excited state $|\mathcal{E}\rangle$ cannot be reached upon one-photon absorption and is located at higher energy than the optically active state $|\mathcal{C}\rangle = |Z_-\rangle$. The mixing between $|N\rangle$ and $|Z_+\rangle$, measured by ρ, only depends on the z/τ ratio. As sketched in Figure 1.14, the systems with large mixing ($\rho \sim 0.5$) are characterized by large energy gaps among all states (class II dyes), while the systems with small mixing ($\rho \to 0$ or $\rho \to 1$ class I or III dyes, respectively) show a pair of quasi-degenerate eigenstates, either in the excited or ground state regions, signalling a conditional instability.

By studying the problem for the isolated molecule in the gas phase, valuable information can be collected about the tendency of the dye towards symmetry breaking, adopting an adiabatic approximation to treat molecular vibrations. Along these lines, the potential energy surfaces (PESs) for the ground and excited states can be drawn and analytical results may be obtained for the phase diagram of quadrupolar dyes (Fig 1.15). In the (ϵ_v,ρ) plane, the black curves mark the boundaries between the three different classes: for class I dyes the PES associated with the first excited state shows a double minimum along the antisymmetric mode, suggesting a tendency to symmetry breaking for this state. Class II dyes are characterized by well-behaved PES for all the three states,
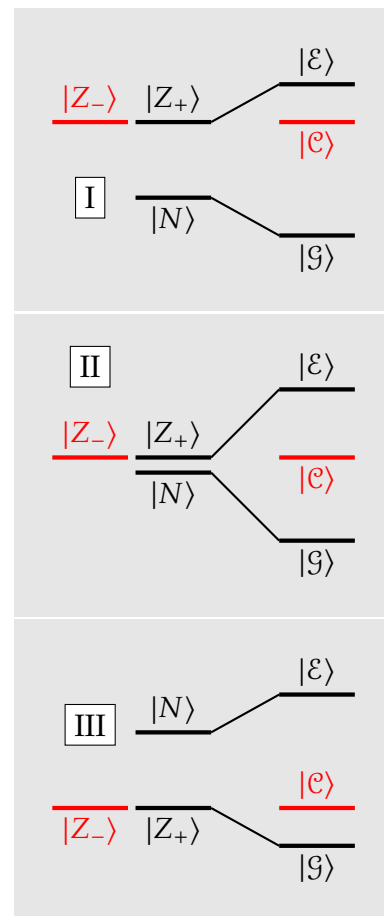

Figure 1.14: Sketch of the essential states of class I, II and III quadrupolar chromophores
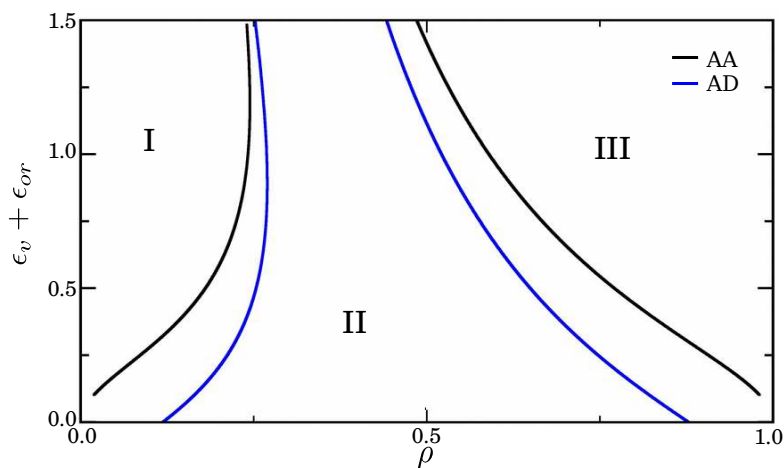
Figure 1.15: Phase diagram for quadrupolar dyes. The black line show antiadiabatic (antiadiabatic) results, the blue lines show adiabatic (AD) results for $\epsilon_{el} = 0.3$

and are therefore not prone to symmetry breaking. Finally, class III dyes are characterized by a bi-stable ground state. It is important to underline at this stage that symmetry breaking cannot be observed in an isolated molecule.[49] The double minimum in the excited or ground state of the systems in class I or III, respectively, does not necessarily imply a symmetry breaking phenomenon and finite-size systems will oscillate between the two minima recovering the full symmetry in a sort of dynamical Jahn–Teller effect.[50] Of course, a genuine symmetry breaking may be observed if the dye is dissolved in a polar solvent. Polar solvation, corresponding to an extremely slow motion, can be described accurately in the adiabatic approximation, and the relevant relaxation energy, $\epsilon_{or} = \mu_0^2 r_{el}/2$, enters the picture summing up to ϵ_v in the phase diagram shown in Figure 1.15, thus widening the region where either ground or excited state instability occurs. Even more importantly, the slow motion associated with polar solvation basically freezes the system in one of the minima not allowing the tunneling in the time window of relevance to optical spectroscopy. Symmetry breaking driven by polar solvation in the excited state of class I polar dyes quite naturally explains the large positive solvatochromism observed in the fluorescence spectra of these systems, while the ground-state symmetry breaking in class III dyes is the key to understand the anomalous absorption solvatochromism observed in long cyanine dyes, in spite of their nominally symmetric structure.[51–53]

The phase diagram in Figure 1.15 is not affected if fast solvation is accounted for. Indeed in the antiadiabatic approximation, the electronic polarizability of the solvent lowers the energy gap $2z$, as discussed in Section 1.6.2, leading to an increase of ρ. However, the phase diagram in Figure 1.15 relies on ρ and hence still applies: the black lines separating the different regions in the phase diagram are not affected by the variation of the medium refractive index. Instead, if the adiabatic approximation is incorrectly enforced to describe fast solvation, the relevant relaxation energy ϵ_{el} would enter the

picture much as in the case of polar solvation, hence summing up to ϵ_v, as shown in Figure 1.15, favoring symmetry breaking. In other words, as illustrated in the phase diagram in Figure 1.15 for the specific case $\epsilon_{el} = 0.3$ (blue lines), the boundaries between the different regions in the phase diagram would be downshifted by ϵ_{el}, artificially widening the instability regions associated with class I and class III dyes.

Figure 1.16 show analytical results for the electronic model ($\epsilon_v = \epsilon_{or} = 0$) relevant to the three quadrupolar systems with z adjusted to have ρ_{gas} = 0.2, 0.5 and 0.8, as representative of class I, II and III dyes, respectively. In all cases, the antiadiabatic results (black lines) predict an increase of ρ upon increasing the medium polarizability. This always implies an increase of the transition dipole moment μ_{CT} for the allowed $\mathcal{G} \rightarrow \mathcal{C}$ transition. For the class I system (ρ_{gas} = 0.2), the two transition frequencies ($\mathcal{G} \rightarrow \mathcal{C}$ and $\mathcal{G} \rightarrow \mathcal{E}$) decrease considerably with the medium refractive index, while the effects are less pronounced in the other two systems, with the lowest (highest) transition decreasing (increasing) in energy with ϵ_{el}.

Enforcing the adiabatic approximation for fast solvation leads to different Hamiltonians, depending on the reference state selected to equilibrate the reaction field. The continuous and dotted blue lines shown in Figure 1.17 refer to the adiabatic results obtained by fixing F_{el} to the equilibrium value relevant to the ground state or to the optically-allowed ($\mathcal{C}$) excited state, respectively. Since the ground-state dipole moment vanishes as long as the ground state symmetry is conserved, the adiabatic results obtained for F_{el} equilibrated to the ground state do not vary at all with ϵ_{el} as long as the ground-state symmetry is preserved. This is the case for the quadrupolar dye with ρ_{gas} = 0.2 (left panels), where no variation of either $\rho_{\mathcal{G}}$ or μ_{CT} or ω_{CT} is obtained in the ground-state adiabatic approximation (full blue lines) when ϵ_{el} is increased. On the other hand, the adiabatic results obtained for F_{el} equilibrated to the optically-allowed excited state do not vary at all with ϵ_{el} as long as the excited-state symmetry is preserved. This is the case of the quadrupolar dye with ρ_{gas} = 0.8 (right panels), where no variation of either $\rho_{\mathcal{G}}$ or μ_{CT} or ω_{CT} is obtained in the excited state adiabatic approximation (dotted blue lines) when ϵ_{el} is increased. The adiabatic results contrast sharply with the antiadiabatic results that instead properly account for the effect of solvent polarizability on the molecular properties.

However, the most striking failure of the adiabatic approximation to fast solvation in quadrupolar systems is the prediction of spurious symmetry-breaking phenomena. The class II system in the middle panels of Figure 1.16 (ρ_{gas} = 0.5) is a paradigmatic example: if electronic solvation is properly described in the antiadiabatic

Figure 1.16: Fast solvation effects on the properties (ground-state ionicity, transition dipole moment, transition frequency) of quadrupolar dyes belonging to different classes and with $\epsilon_v = 0$. Two transition energies are shown corresponding to the $\mathcal{C}$ and $\mathcal{E}$ states (lower and higher transition energy, respectively). The transition dipole relevant to the transition from the ground to the $\mathcal{E}$ state vanishes and is not shown. Antiadiabatic (antiadiabatic) results: black lines; Adiabatic (AD) results with F_{el} equilibrated with the ground state (full blue lines) or with the optically-allowed excited state (dotted blue lines). The abrupt changes observed in adiabatic results mark the occurrence of symmetry breaking.
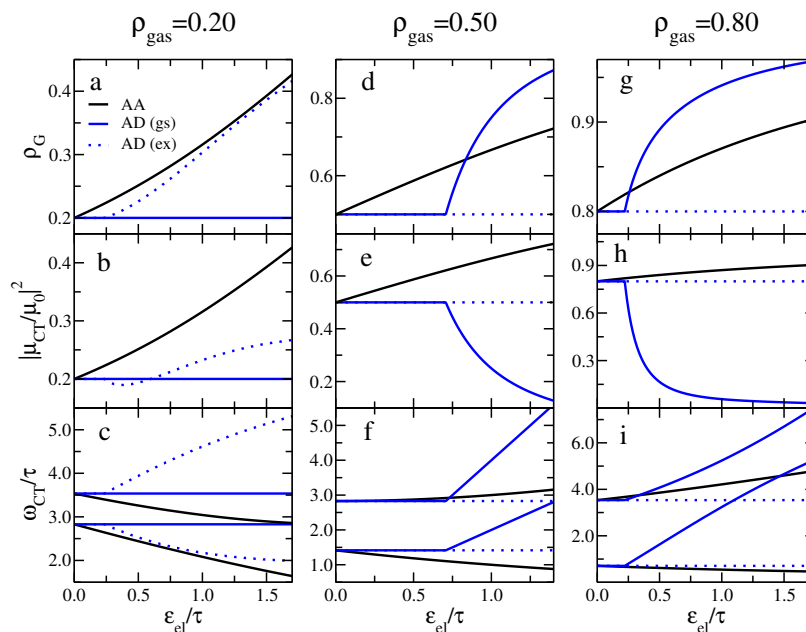
approximation, the system is not prone to symmetry breaking, but if a ground state adiabatic approach is enforced, the ground state undergoes symmetry breaking at $\epsilon_{el} \sim 0.75$, as shown by the abrupt variation of the molecular properties (full blue lines). At the same time, the symmetry is preserved in the excited state, so that in the adiabatic approximation, when F_{el} is equilibrated to the $\mathcal{C}$ state, ϵ_{el} does not affect the molecular properties (dotted blue lines). For the system with $\rho_{gas} = 0.8$, the ground-state adiabatic approximation predicts symmetry breaking in the ground state for $\epsilon_{el} \sim 0.25$, while the symmetry is preserved in the $\mathcal{C}$ state. For the system with $\rho_{gas} = 0.2$, the excited state adiabatic approximation predicts symmetry breaking in the $\mathcal{C}$ state for $\epsilon_{el} \sim 0.30$, while the symmetry is preserved in the ground state.

The vibronic bandshapes are shown in Figure 1.17 for the same three representative systems, but fixing $\epsilon_v = 0.3$ and $\epsilon_{el} = 0.32$. Marginal differences between the antiadiabatic and adiabatic results are found as long as the symmetry is conserved in the adiabatic calculation, while sizable deviations are of course observed for emission spectra of class I dyes and huge deviations are seen for the absorption spectra of class III dyes, due to spurious symmetry-breaking effects obtained in the adiabatic picture.

1.6.4 Octupolar dyes and symmetry-breaking

The three-fold rotation axis in octupolar chromophores implies the presence of doubly degenerate states, which leads to instabilities, precluding the presence of class II dyes, as shown in the phase diagram in the bottom panel of Figure 1.18. As in the case of quadrupolar chromophores, the phase diagram, plotted against
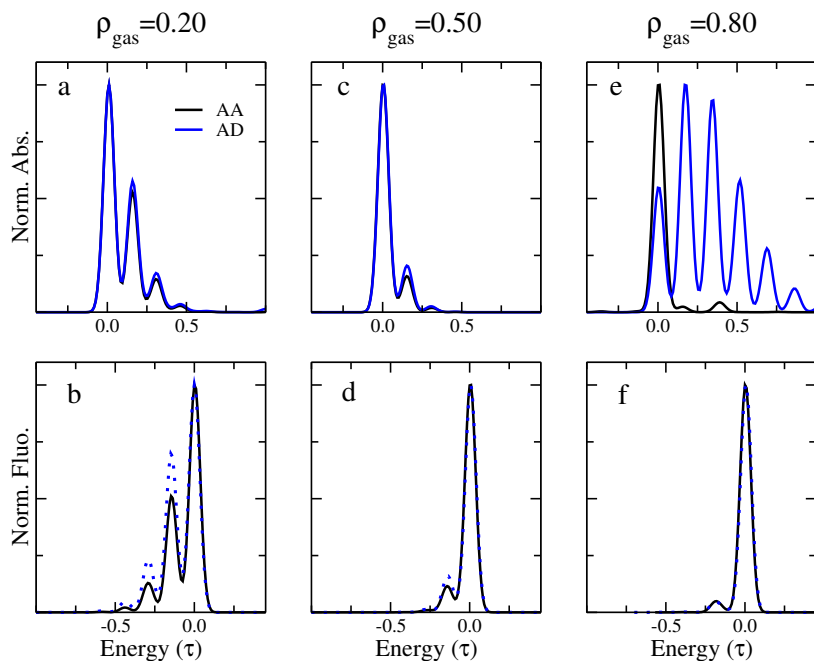
Figure 1.17: Vibronic absorption (top) and fluorescence (bottom) spectra for quadrupolar dyes of different classes, for $\epsilon_v = 0.3$ and $\epsilon_{el} = 0.32\tau$. Black lines: antiadiabatic results; Blue lines: adiabatic results.

the ground-state ionicity, is independent of ϵ_{el} in the correct antiadiabatic limit (black line). In the adiabatic approximation instead the boundary is lowered along the ordinate by ϵ_{el} (blue line). Class I octupolar chromophores are characterized by a symmetry breaking in the first excited state, while class III octupolar chromophores show symmetry breaking both in the ground state and first excited state.

The left panels of Figure 1.18 show the molecular properties calculated for an octupolar dye with $\rho_{gas} = 0.2$ (to the best of our knowledge there are no examples of octupolar dyes of class III). The antiadiabatic calculation predicts, as expected, an increasing contribution of zwitterionic states into the ground state (increasing ρ) when ϵ_{el} is increased. Concomitantly, the transition dipole moment towards the optically-allowed state, corresponding to a doubly degenerate state, increases while the excitation energy towards either the lowest-energy (allowed) or the highest-energy (forbidden) excited states decreases. The system remains stable, preserving its symmetry, as long as slow degrees of freedom do not enter into play. The adiabatic calculation instead predicts no effect of the medium polarizability when F_{el} is equilibrated to the ground state. On the other hand, when the reaction field is equilibrated to the lowest excited state, clear signatures of a spurious symmetry breaking appear. As for vibronic bandshapes, the results in Figure 1.18d and Figure 1.18e for the dye with $\rho_{gas} = 0.2$, $\epsilon_v = 0.3$ and $\epsilon_{el} = 0.32$ show marginal differences between the spectra calculated in the adiabatic vs the antiadiabatic approximation.
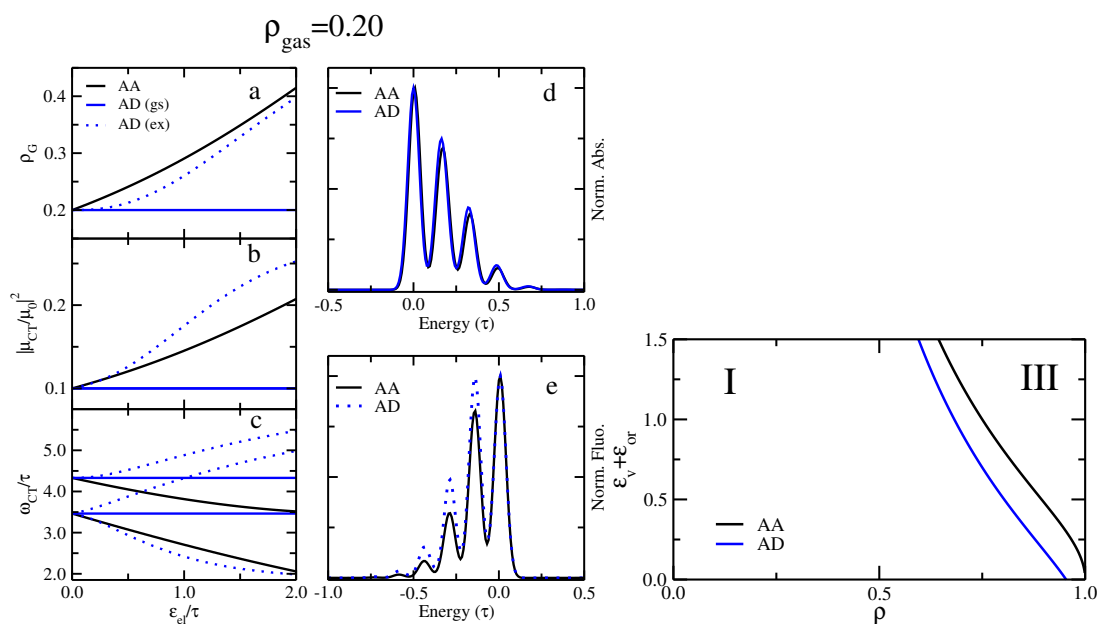
$\rho_{gas}=0.20$

Figure 1.18: Top panels: fast solvation effects on an octupolar chromophore with $\rho_{gas} = 0.20$. Black lines show antiadiabatic (antiadiabatic) results; blue lines show adiabatic (AD) results with F_{el} equilibrated with the ground state (continuous lines) or with the optically-allowed excited state (dotted lines). Panels (a-c) show the electronic properties (ground-state ionicity, transition dipole moment, transition frequencies) as a function of ϵ_{el} for a system with $\epsilon_v = 0$. Panels (d) and (e) show vibronic absorption and fluorescence spectra, respectively, calculated for $\epsilon_{el} = 0.32$ and $\epsilon_v = 0.3$. Bottom panel: phase diagram ($\epsilon_{el} = 0.3$ for the adiabatic, AD, result).

1.7 Conclusion

Solvation is a complex phenomenon involving several degrees of freedom characterized by different timescales. In particular, a slow component of solvation is driven by the orientational motion of polar solvent molecules around the solute, and is only relevant in polar solvents. Another component is instead always present, irrespective of the solvent polarity, and is related to the solvent electronic polarizability, as measured by the solvent refractive index. This component is related to the rearrangement of the electronic clouds of solvent molecules and therefore corresponds to a fast motion, since the electronic excitation of the solvent typically falls in the mid/far-UV region, i.e. at significantly higher frequencies than the relevant degrees of freedom of organic dyes. The slow orientational component of solvation can be safely dealt with in the adiabatic approximation, but the same approximation is not suitable to treat fast solvation, as it does not account for the fast response of the solvent electronic clouds in response to the charge fluctuations in the solute.

Explicit-solvent approaches[54–63] relying on QM-MM methods are often adopted to investigate solvent effects on the spectroscopic properties of organic dyes. Even more popular are continuum solvation models, like PCM, COSMO, etc...[54, 58, 64–80] As extensively discussed in this chapter, none of these approaches

properly accounts for the electronic polarizability of the medium, leading to results that need a careful consideration. Several variants of continuum solvation models are discussed in the literature,[16, 17, 19, 81–83] that face the problem of fast solvation from slightly different perspectives, however, with the notable exception of early attempts,[84, 85] all approaches rely on the diagonalization of a molecular Hamiltonian obtained for a fixed potential from environmental charges. Whatever choice is made for the definition of the excited states of interest for absorption and emission processes, these methods are bound to fail, since the actual molecular states for a molecule in a polarizable environment should all be obtained diagonalizing a single Hamiltonian where the environmental polarizability affects in different ways the energy of the states of the systems and their coupling. Similarly quantum-classical approaches with explicit solvent models (QM-MM approaches) do not properly account for the solvent polarizability, even when a *polarizable environment* is considered. In fact in polarizable models, one allows the charges on the solvent molecules to reorganize in response to the solute perturbation, but the molecular Hamiltonian is always defined accounting for a frozen potential generated by the surrounding charges.

In this chapter, the adiabatic approximation on electronic degrees of freedom of the solvent is critically discussed, and several shortcomings are revealed. In section 1.4.1, with reference to widely studied dipolar and quadrupoar dyes, the main quantities relevant to spectroscopy are adressed describing the solute in terms of a few-state electronic basis. A more general approach has been adopted in section 1.6, where dipolar, quadrupolar and octupolar dyes are modelled using essential state models and addressing electronic properties as well as spectral bandshape, extending the model to account for electron-vibration coupling through effective molecular coordinates. In these cases, the adiabatic approximation leads to an incorrect description not only of the transition properties, but of the molecular ground state itself (Section 1.4.1 and 1.6.2). For example, in polar dyes with a largely neutral ground state, the adiabatic approximation underestimates the increase of the ground state dipole moment as due to the polarizability of the environment, simply because the equilibrium reaction field for a largely neutral ground state is small and cannot account for the large stabilization of polar charge fluctuations.

Moreover, when applied to quadrupolar and octupolar dyes, the adiabatic approximation to fast solvation can drive symmetry breaking in systems where it cannot possibly occur (section 1.6.3 and 1.6.4). Specifically, genuine symmetry breaking can never occur in isolated (gas phase) molecular systems, nor can it be induced by fast solvation. Only polar solvation, associated with an

extremely slow, classical coordinate may drive a *bona fide* symmetry breaking in a molecular system. Symmetry breaking phenomena as often discussed in the chemical literature in the gas phase or in non-polar solvents are actually artifacts associated with the adiabatic treatment of vibrational degrees of freedom and/or of fast solvation.

In section 1.5, electronic solvation of TADF dyes is discussed. TADF dyes are particularly delicate to model since the subtle interplay between localized and CT states makes environmental or matrix effects crucial in the definition of the tiny energies, the singlet-triplet gap and the spin-orbit coupling, that define the system performance.[32–34, 45, 56, 65, 78, 80, 86] Of special concern is the inversion of the lowest singlet and triplet states calculated in the adiabatic CLR and EI implementations of PCM for some TADF-dyes. Indeed the breaking of the Hund rule was reported in so called multi-resonant CT systems, a family of strongly correlated molecular systems, typically with highly symmetric structures, exhibiting a characteristic spatial separation of HOMO and LUMO orbitals that are delocalized on the whole molecular structure.[87–91] The molecules discussed here do not show these characteristics. Moreover, the singlet-triplet inversion observed in multi-resonant CT systems requires high quality *ab initio* calculation, involving at least double excitations.[87, 88] The inclusion of a standard TADF dye in a polarizable environment was also suggested as a possible origin for singlet-triplet inversion.[56, 87] However these results were obtained and discussed treating the medium polarizability in the adiabatic approximation and deserve a careful reconsideration, either adopting the more adequate antiadiabatic approximation or possibly addressing both the solute and its surrounding medium in a fully quantum mechanical approach.

Since the adiabatic approximation is not valid for the electronic degrees of freedom of the solvent, models that allow to properly account for the dynamical response of the solvent must be developed. In this Chapter, as a proof-of-concept the reaction field model is adopted to describe the solute-solvent interaction. It is much simpler than implicit solvation models like COSMO or PCM, but it aims at the same physics (i.e. dielectric solvation) and represents a good starting point to address the core concept of this work: solvent and solute electronic degrees of freedom related to the electronic polarizability must be coupled accounting for the relative dynamics, with electronic degrees of freedom of the solvent being faster than solute degrees of freedom.

The non-adiabatic approach discussed in section 1.3 describes the solvent electronic polarization as an explicit quantum mode, leading to a Hamiltonian written on the basis spanned by the direct product of solute and solvent basis, that can be diagonalized

to achieve numerically exact results. The non-adiabatic approach, however, is not an implicit solvation model, as knowledge of the solvent excitations is required. Since the electronic degrees of freedom of the solvent resonate at higher frequencies with respect to electronic degrees of freedom of the solute, the antiadiabatic approximation is adopted, that assumes that the solvent electronic polarization responds instantaneously to charge fluctuations in the solute. The antiadiabatic approximation leads to a proper implicit solvation model, not requiring any detailed knowledge of the solvent dielectric response. The solvent electronic degrees of freedom are renormalized away in the antiadiabatic limit, leading to an effective Hamiltonian with the same size as the gas phase Hamiltonian.

In the early 90's antiadiabatic approaches were proposed for fast solvation, but never gained traction.[84, 85] Most probably, this is related to the choice of a wrong name for the approximation that was called Born-Oppenheimer rather than antiadiabatic. Indeed the Born-Oppenheimer approximation is a specific flavor of the most general adiabatic approximation that allows to separate slow degrees of freedom from relevant electronic degrees of freedom, through the definition of an electronic Hamiltonian that parametrically depends on slow coordinates.[92] It is true that also slow degrees of freedom are finally treated in the adiabatic approximation, but this is only possible after the adiabatic electronic Hamiltonian (defined for frozen slow coordinates) is diagonalized. Using the name Born-Oppenheimer to address an antiadiabatic approximation, where instead a single electronic Hamiltonian is defined, was therefore unfortunate and may be the reason why the strategy was not recognized as the only viable approach to renormalize out the of the problem the degrees of freedom related to fast solvation.

The term antiadiabatic, borrowed from the physics community working on polarons and superconductivity,[93] was used in the context of fast solvation in 1999,[37] with reference to semiempirical model Hamiltonians, and was proposed again in the context of quantum chemical approaches.[9] Other authors have also recently recognized the value of the antiadiabatic approach to treat fast solvation.[94] Unfortunately, these authors stick on the Born-Oppenheimer notation, that obscures the qualitatively different nature of the antiadiabatic approach with respect to the adiabatic approximation. As extensively discussed here, the antiadiabatic approximation can be applied to solute degrees of freedom slower than the electronic degrees of freedom of the solvent, typically located deep in the UV (energies much larger than 6 eV): applying it to all electronic excitations in the solute is bound to fail, as also demonstrated in Ref. [94]. However, a clever choice of the

basis states can be made as to renormalize only relevant degrees of freedom, and, as the results in Figure 1.9 show for a specific example, converged antiadiabatic results can be obtained working in an energy window well within the critical threshold for common solvents.

15: This is the case for some matrices used in TADF applications

While the adiabatic approximation can never be applied to electronic solvation, whose dynamics is faster than the relevant solute degrees of freedom, the antiadiabatic approximation works well when the solvent degrees of freedom are much faster than the solute ones. The antiadiabatic approximation therefore should be considered with care when the solvent excitation spectrum comes very close in energy to the solute spectrum.[15] For common solvents and polymeric matrices used in spectroscopy, the UV-cutoff is typically larger (and often much larger) than 4 eV. Moreover, it must be recognized that the UV cutoff signals the frequency where the solvent absorption starts, the relevant absorption bands being located at much larger energy (just as an example, the water cutoff is at 6.5 eV, but the absorption spectrum peaks at ~ 15 eV[95], with a large UV tail that moves the central frequency to ~ 24 eV[9]). In systems where the antiadiabatic approximation to fast solvation breaks down, due to similar timescales of the solute and solvent motions, the adiabatic approximation still does not represents a viable alternative. Rather, solute and solvent degrees of freedom cannot be disentangled and one must resort to a full quantum mechanical approach to the solute and the solvent. Along these lines, the beautiful work reported in ref. [96] for water solvated dyes, offers another independent demonstration of the failure of the adiabatic approximation to fast solvation. In that work, a QM-MM approach is adopted, where the potential generated in the QM region by the charges on water molecules in the MM region is described (as usual) in the adiabatic approximation. In order to get reliable results, the solvation sphere described by QM must include a large number of water molecules (of the order of at least 200, depending on the solute and on the state of interest).

Once fast solvation is accounted for in the antiadiabatic approximation, polar solvation can be dealt with in the adiabatic approximation. For this application EI, leading to formally exact results, is more accurate than either LR or CLR approaches, based on perturbative expansions. Optical transitions occur vertically with respect to slow degrees of freedom. Accordingly, the eigenstates involved in the absorption process are obtained diagonalizing the adiabatic Hamiltonian with the potential due to slow solvation fixed to the ground state equilibrium value. Similarly, the states involved in fluorescence are obtained diagonalizing the adiabatic Hamiltonian with the slow-solvation potential equilibrated to the lowest excited singlet. In either case, transitions are calculated between states that

are obtained from the diagonalization of the same EI Hamiltonian. The issue of incongruent eigenstates, affecting EI when applied to fast solvation, does not show up in dealing with polar solvation, for which the adiabatic approximation works well.

In this Chapter, electronic solvation is addressed with success adopting of the reaction field model. The model relies however on several approximations: the solute-solvent interaction is truncated to the dipolar term. The solute is treated as a point dipole that occupies the center of a spherical cavity. Indeed, the computed properties of the dyes studied here with the reaction field model qualitatively agree with those obtained with PCM, that, along with other implicit solvation models like COSMO and SMD, aim at the same photophysics, i.e. dielectric solvation, with much more detailed description of the solute-solvent interaction. However, current implementations of PCM, COSMO and SMD lack an antiadiabatic approach to electronic solvation. An antiadiabatic approach that goes beyond the limits of the reaction field model is therefore desirable to study atomistic systems in realistic surroundings, described either as a continuum with solute-adapted cavity or explicitly with molecular mechanics. Specifically, there are some cases where the reaction field model is expected to fail, such as for solutes with large dimensions, that cannot be described as point dipoles, and ionic species, where the monopole term is the leading term in the multipole expansion. First steps in this direction have been made during my secondment at the Institut Néel in Grenoble, under the supervision of Dr. Gabriele D'Avino.

Thermally-activated delayed fluorescence | 2

2.1 Introduction

Arguably, organic light emitting diodes (OLED) represent the most successful application in the field of plastic optoelectronics. Indeed OLED entered the market of displays and are currently exploited in several commercial devices. This boosted research activities in science and technology, in a multidisciplinary effort involving chemists, physicists, and engineers. The simplest OLED device is composed of a thin layer of fluorescent organic material, called the active layed, sandwiched between an anode and a cathode. When a sufficient potential is applied, electrons and holes are injected in the material from the electrodes and migrate in the active layer under the action of the electric field. The charge carrier recombination generates bound electron-hole pairs, excitons, that can then decay radiatively (Figure 2.1).[97] The internal quantum efficiency of an OLED depends on many factors, such as the ease of charge injection and the ratio of emissive excitons over the total number of formed excitons. Devices of increasing complexity, in terms of electrode engineering [98] and/or with structured, multilayer active interfaces [99], were successfully devised to improve the device efficiency. On the other hand, chemists gave a valuable contribution to the design and synthesis of new active materials that show excellent luminescence quantum yields [100, 101].

However, there is an intrinsic limitation in the efficiency of fluorescent OLED, also referred to as first generation OLED, (Figure 2.2), that is traced back to the inability to control the spin orientation of the charge carriers injected in the active material. Simple spin-statistics suggests that out of the excitons formed upon charge

Figure 2.1: Sketch of an OLED. The zoomed region shows the amorphous nature of the active layer, composed of emitter molecules (magenta) dispersed host molecules (blue). In some case, the matrix is constituted by the emitter itself.
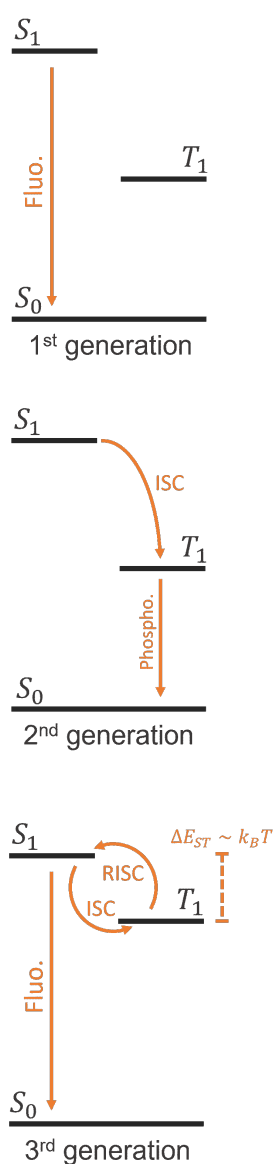
recombination, the emissive singlet excitons are formed in a 1:3 ratio with respect to the triplet excitons, posing a 25% limit to the maximum internal efficiency. Therefore triplet harvesting, namely converting triplet states into emissive states, is an attractive way to increase the efficiency of OLEDs [102]. The most direct way to approach triplet harvesting exploits phosphorescent materials. This lead to the development of phosphorescent OLEDS (PHOLEDS), also referred to as second generation OLED, that can reach 100% internal quatum efficiency (Figure 2.2).[103] However this approach has serious limitations. First, in order to facilitate intersystem crossing (ISC), heavy atoms such as Pt and Ir are generally needed, considerably increasing the cost of production. Moreover, and more importantly, achieving efficient blue phosphorescence is intrinsically difficult. Indeed, phosphorescence originates from the radiative decay of the lowest triplet state of the emitter, that generally resonates at much lower energies than the lowest energy singlet state. Finally, the long lifetime of phosphorescent states makes PHOLEDs inadequate for applications where high frequency modulation of the emission is needed. As a consequence, modern OLED RGB displays rely on efficient second generation devices for the red and green emissive units, while inefficient first generation devices are used for the blue emissive unit, with serious consequences on device lifetime and energy consumption.

A more promising way to harvest triplet states implies transferring the excitation from the triplet to a singlet state. Triplet-triplet annihilation (TTA) was first discovered in anthracene derivatives [104] and has been exploited to convert two triplet states into a singlet state in OLEDs [105]. This has some advantages over phospherescence since it does not require heavy atoms, but still limits the maximum internal quantum efficiency to 62.5%, due to the 2:1 ratio of triplet-to-singlet conversion.

Thermally-Activated Delayed Fluorescence (TADF) breaks this limit bringing the internal quantum efficiency to a theoretical 100%. TADF was first observed more than fifty years ago in eosin molecules [106] and has been recently proposed as a promising triplet harvesting method for OLEDs, in the pioneering work of Adachi [107]. At variance with organic molecules, where the lowest singlet (S_1) and triplet (T_1) states are separated by energy gaps of the order of $0.5 - 1.0$ eV, in TADF emitters the S_1-T_1 energy gap is comparable to the thermal energy (Figure 2.2). Under these conditions, the excitation can be transferred from triplet to singlet states in a process called reverse intersystem crossing (RISC). As a result, *delayed* fluorescence is obtained, in addition to *prompt* fluorescence. Ideally, TADF offers several advantages over other triplet harvesting methods, allowing, with pure organic molecules, internal quantum efficiencies comparable to the ones of PHOLEDs,

Figure 2.2: Schematic representation of the states and main photophysical processes involved in first, second and third generation OLED.

with faster decay rates. Moreover, it is advantageous over TTA for its 1:1 singlet-to-triplet conversion ratio. Finally, delayed fluorescence has the same spectral characteristics of prompt fluorescence, ideally making the design of efficient blue emitters easier. OLEDs based on TADF emitters show clear and undisputed advantages over PHOLED, and are therefore referred to as third generation OLED.[1]

Despite the hype, at present third generation OLED technology (specifically blue TADF OLED) is not ready for commercial applications, due to the poor operational lifetime. Indeed, blue TADF emitters require to relatively high operational voltages that promote decomposition reactions of the emitter, often involving reactions with the host molecules. Moreover, the lifetime of triplet excitons is generally too long, favouring degradation reactions or inefficient TTA. Experimental and theoretical characterization of degradation mechanisms is intrinsically difficult, even more so since the current understanding of TADF photophysics is not developed enough to allow the rational design from the emitter to the device.[108]

The first design of TADF emitters [21] was based on the reduction of the S_1-T_1 energy gap, using intramolecular charge transfer (CT) in systems containing spatially separated electron donor and electron acceptor moieties. In the classical design, heteroaromatic fragments are connected in a twisted conformation around the donor-acceptor bond.[21] Because of the large dihedral angle between the donor and acceptor units, efficient charge separation and low electron-hole overlap is achieved in CT states, resulting in a low S_1-T_1 exchange interaction energy and, consequently, reduced singlet-triplet energy gaps. This initial approach gave good results in terms of device efficiency, stimulating the interest towards further study of TADF.

It was soon suggested that the mechanism behind TADF is actually more intricate than initially proposed. Indeed, the spin-flip transition between states of the same character, such as pure CT triplet and singlet states, is forbidden by the El Sayed rule.[109]For this reason, the key role of triplet local excited states, ^{3}LE, i.e. states where the excitation is localized on either the donor or the accepetor units, has been proposed for efficient RISC [24]. The triplet manifold is inherently more complex than the singlet manifold: due to the stabilization of triplet states by the exchange interaction, ^{3}LE states are generally lower in energy than their singlet counterpart, ^{1}LE, so that, in some systems, ^{3}LE and ^{3}CT states are close in energy. Being ^{3}LE-^{1}CT transitions El Sayed allowed, low energy ^{3}LE states may indeed play an important role in RISC, facilitating the singlet-triplet upconversion either as mediators between ^{3}CT and ^{1}CT, through a multi-step mechanism, or through a mixing with CT triplet states.

1: A fourth generation of OLED has also been proposed, where TADF dyes first allow triplet harvesting, then tranfer the excitation thorugh energy transfer mechanisms to fluorescent dyes with a high quantum yield.

Moreover, strictly orthogonal (non-conjugated) systems have vanishingly small transition dipole moments from the excited singlet to the ground state,[35] strongly suppressing emission intensity. Indeed, the prompt fluorescence lifetime in TADF emitters, typically in the $\sim 10^{-8} - 10^{-7}$ s is longer than in common organic fluorescent probes, typically in the 10^{-9} s timeframe. Despite the obvious intrinsic drawbacks, many twisted donor-acceptor systems show TADF activity, suggesting that the aforementioned considerations on the magnitude of transition dipole moments and spin-orbit couplings are based on an incomplete picture of the TADF process.

Indeed, conformational flexibility modulates the donor-acceptor conjugation, affecting most properties that govern TADF efficiency, like the singlet-triplet gap, the spin-orbit couplings and the transition dipole moment, often turning transitions that are forbidden in a "frozen molecule picture" into allowed transitions.[33, 34, 110] Adding to the complexity of the phenomenon, the ever-present effects of the environment are expected to be significant on TADF emitters, where both localized and charge transfer states play a role. Modelling the environment is of paramount importance as TADF emitters in the final device are dispersed in amorphous matrices composed of small organic molecules or polymers, as sketched in Figure 2.1. On the other hand, spectroscopic characterization is also carried out on samples in condensed phase, typically in solution, meaning that even in the most controlled conditions, the medium in which the dye of interest is dissolved must be considered with great care. In this work, donor-acceptor TADF dyes are considered, with a focus on molecular modelling and calculation of the photophysical rate constants related to the TADF process.[45, 111, 112]

For the sake of completeness, this introductory section is concluded with a discussion on other approaches towards efficient TADF. The intrinsic drawbacks of donor-acceptor TADF emitters stimulated research towards novel TADF emitters. The first natural development over the donor-acceptor design was using multipolar structures composed of multiple donor and acceptor units, in an effort to increase the electronic density of states in the singlet and triplet manifolds, in turn allowing for multiple non-radiative pathways for ISC and RISC.[23, 24] In principle, the models developed and discussed in this chapter are applicable to multipolar emitters as well, at the cost of an increased complexity in terms of molecular structure as well as number of excited states involved in the photophysics. Another promising design is based on through space CT complexes, i.e. systems composed of electron donor and electron acceptor moieties not directly connected through a chemical bond, but still experiencing electron hopping through space.[27, 113] A

different strategy aims to achieve small singlet-triplet gaps, as well as high fluorescence quantum yields and narrow emission bands, exploiting multiresonant TADF emitters. Multiresonant emitters are planar conjugated organic molecules that include nitrogen and/or boron atoms to achieve spatial separation between HOMO and LUMO and therefore small singlet-triplet gaps.[87–91] One of the most intriguing developments on multiresonant TADF systems occurred when it was realized that special heteroatomic conjugated systems, like heptazine and its derivatives, break the Hund's rule, showing a negative singlet-triplet gap. Strictly speaking, these systems cannot be classified as TADF emitters, as thermal activation is not required for RISC when the S_1 is lower in energy than T_1. Negative singlet-triplet gap emitters open new challenges in modelling, as high quality quantum chemical methods are required to account for the strong electron correlation responsible for the breaking of the Hund's rule.[91]

2.2 Theoretical modelling and challenges

As already hinted in the previous section, modelling donor-acceptor TADF emitters requires methods to address the photophysics of electronic states with different spin and electronic character. Moreover, the role of vibrational and conformational motions cannot be neglected, opening the issues of identifying the relevant molecular modes and strategies to deal with the coupling between electronic and nuclear degrees of freedom. The excited state landscape in TADF emitters is generally rather crowded, with many states cohexisting in a narrow energy window. The adiabatic and Born-Oppenheimer approximations at the basis of modern quantum chemistry must therefore be applied with care, and in some cases are expected to fail, as, for example, when degeneracy or near degeneracy occurs between the ^{1}CT and ^{3}CT states. Additionally, the surrounding environment plays an important role, affecting the relative energy of the excited states and the dynamics of molecular motion, also giving rise to broadening phenomena that in turn call for a statistical description of the macroscopic sample to meaningfully simulate experiments.

Parametric Hamiltonians have been proposed and are extensively adopted in the host laboratory, in particular Essential-State Models (ESMs) that successfully describe the spectroscopic properties of CT chromophores.[39, 46, 114, 115] In ESM, CT dyes are described in terms of a reduced number of electronic states, usually corresponding to the main resonating structures. Molecular vibrations are introduced leading to a vibronic Hamiltonian that can be diagonalized in a non-adiabatic approach. The interaction with the

environment can also be accounted for in terms of electrostatic interactions. This versatile approach has successfully described the photophysics of multipolar dyes in solution[40, 114] and in aggregates [116, 117] The comparative simplicity and low computational cost make ESMs a good starting point to describe complex phenomena, such as relaxation dynamics of systems in excited states [118]. In Section 1.6, ESMs describing dipolar, quadrupolar and octupolar dyes are discussed. In this Chapter, and in particular in Section 2.3.2, the two-state ESM for dipolar dyes is extended to account for triplet states in order to model dipolar TADF emitters. ESMs are semi-empirical methods and are usually validated against experimental data, namely optical spectra. This poses an interesting issue when they are applied to TADF emitters, since parameters for triplet states need to be defined. Triplet states are inherently more difficult to characterize experimentally than singlet states, since the main source of information is represented by phosphorescence spectra, and thus are relevant only to the excited triplet state in its relaxed geometry. Moreover, phosphorescence is only typically observed at low temperature and in rigid matrix.

One promising way to overcome these problems is offered by *first principle* calculations, that give specific information on triplet states, (e.g. vertical excitation energies) that are not accessible experimentally. First principle methods are widely used by theoreticians to study TADF emitters and among those, TD-DFT is the most popular, as it offers a good compromise between low computational cost and accuracy [108]. However, TD-DFT has some intrinsic limitations when used to study systems where both localized and CT states play a role [119]. As discussed in Appendix A, some of the issues are traced back to the fact that the most common functionals are accurate in computing either localized or CT transitions, but not both [120]. This problem is faced in Section 2.3.1, where the validation of ESMs against TD-DFT calculations is described.

As for the environment, the polarizable continuum model [19] offers a computationally accessible way to account for dielectric solvent effects in first principle methods, while QM/MM and molecular dynamics methods, at a higher computational cost, allow to model specific interactions also addressing matrix rigidity. However, as discussed in Chapter 1, in excited state calculations this brings to a fairly intricate theoretical problem, since the phenomena of interest are intrinsically dynamic and solvent degrees of freedom respond differently to electronic transitions. In this Chapter this issue will be discussed in detail and the results for TD-DFT calculations accounting for the solvent will be discussed. The concerted optimization of the active dye and its matrix requires a detailed understanding of several interconnected features and concurrent forces towards the precise control of the tiny energy gaps, and of

the tiny interactions that govern TADF efficiency. This challenging endeavor must rely on a careful and critical exploitation of several tools available to the theoretician, validating against a large body of experimental data the adopted approaches and relevant results.

As a first step in this direction, in this Chapter a representative TADF dye is studied, DMAC-TRZ in Figure 2.3a.[121, 122] An extensive spectroscopic characterization of the dye in several solvents and in a frozen matrix, performed in the host laboratory, is reported in Appendix D.1. Spectroscopy studies (performed by prof. Monkman's group in Durham Unversity) in degassed solution and typical host matrices is reported in Appendix D.2. A critical analysis of TD-DFT results is then presented that, together with the large body of experimental data, is exploited to build and validate an ESM for DMAC-TRZ, accounting for low-lying electronic excited states, a conformational degree of freedom and a coupled molecular vibration while addressing environmental effects (Section 2.3).

In Section 2.4, the model developed for DMAC-TRZ is used to calculate photophysical rates. To this aim, a complete non-adiabatic solution of the molecular Hamiltonian is adopted and the rates are computed using the state-by-state Fermi Golden rule. The role of different model parameters on the rates is discussed, as well as the role of the medium polarizability.

In Section 2.6, the discussion is extended to polar environments. Both liquid solvents, as relevant to spectroscopic characterization, and amorphous organic matrices, as relevant to devices, are simulated, in terms of their different dielectric and mechanical responses, allowing the calculation of time-resolved emission spectra.

2.3 Modelling TADF: parametrization and validation

In this section, an effective model is developed to describe the photophysics of DMAC-TRZ, a prototypical donor-acceptor TADF dye. In analogy with many TADF dyes of this family, the two subunits, 9,9-dimethyl-9,10-dihydroacridine (DMAC) and 2,4,6-triphenyl-1,3,5-triazine (TRZ), are connected in a twisted conformation around the donor-acceptor bond, in order to minimize the energy gap between the ^{1}CT and ^{3}CT states through spatial separation of electron and hole densities.

Specifically, in Section 2.3.1 a computational analysis is first carried out using DFT and TD-DFT methods, in order to characterize the electronic states of interest, as well as the molecular modes responsible for the photophysics. In Section 2.3.2, an essential state model

is proposed for DMAC-TRZ, and parameters are extracted from gas phase first principle calculations. The surrounding environment is accounted for using the reaction field model, discussed in Section 1.2. The solvent response dynamics are taken into account partitioning the solvent degrees of freedom in a fast component, related to the electronic response, and in a slow component, related to the orientational response, as discussed in Section 1.4. In Section 2.3.3, the model is validated by comparison with experimental spectra. To this aim, absorption, emission and excitation spectra in liquid and frozen solvent are taken into account. The spectroscopic characterization of DMAC-TRZ and its sub-units is discussed in Appendix D.1.

2.3.1 Computational analysis

In the optimized ground state geometry of DMAC-TRZ (Figure 2.3d), the dihedral angle (θ in Figure 2.3a) amounts to 90°, suggesting a negligible delocalization of electrons between the donor (DMAC) and acceptor (TRZ) units. To address excited states in such a large molecule, TD-DFT is the method of choice and, being interested in both singlet and triplet states, the Tamm-Dancoff approximation is adopted. [31][2]

The choice of the functional is arguably very important when modelling excitations in TD-DFT, as it deeply affects the order of the excited states. The most widely used hybrid functionals, like B3LYP and PBE0, have a low percentage of exact exchange, leading to an overstabilization of CT states.[3] Range-separated functionals, like CAM-B3LYP and functionals with large component of exact exchange, like M06-2X, are considered more suitable to model CT states, but yield different a different order of excited states for DMAC-TRZ (Figure 2.3b). Recent studies propose the use of *optimally tuned* range-separated exchange functionals, where the range-separation parameter, ω, is optimized for each molecule of interest.[126, 130, 131] Fairly reliable results for TADF-dyes are obtained in the optimal long-range corrected PBE (LC-ω*PBE).[126]

Excitation energies of DMAC-TRZ, reported in Figure 2.3b for the lowest singlet and triplet states, are obtained for the optimized $\omega = 0.195$ value and are compared with results obtained with B3LYP,[123] CAM-B3LYP[124] and M06-2X functionals[125] (the ω-tuning procedure is described in Appendix B.0.3). While all functionals find almost degenerate singlet and triplet states with a dominant CT character, the relative energies of CT and LE states change, with B3LYP and PBE0 largely underestimating the energy of CT states and CAM-B3LYP overestimating it. M06-2X slightly overestimates all transition energies, but gives a very similar

2: DMAC-TRZ is optimized in the ground state at the B3LYP/6-31G(d) level. Excited states are modelled using TD-DFT under the Tamm-Dancoff approximation, as suggested in Ref. [31], using the 6-31G(d) basis set and testing different functionals: B3LYP,[123] CAM-B3LYP[124], M06-2X functionals[125] and LC-ω*PBE.[126]. Spin-orbit coupling (SOC) is computed at the M06-2X/6-31G(d) level using the Breit-Pauli Hamiltonian as implemented in Orca 4.1 package.[127, 128] All other calculations are performed in the Gaussian 16 B.10 package. [14]

3: Despite this well-known issue, TD-B3LYP calculations in gas phase with a LR solvent achieve good agreement with the experiment, due to cancellations of errors, coming from the lack of solvent stabilization.[129]
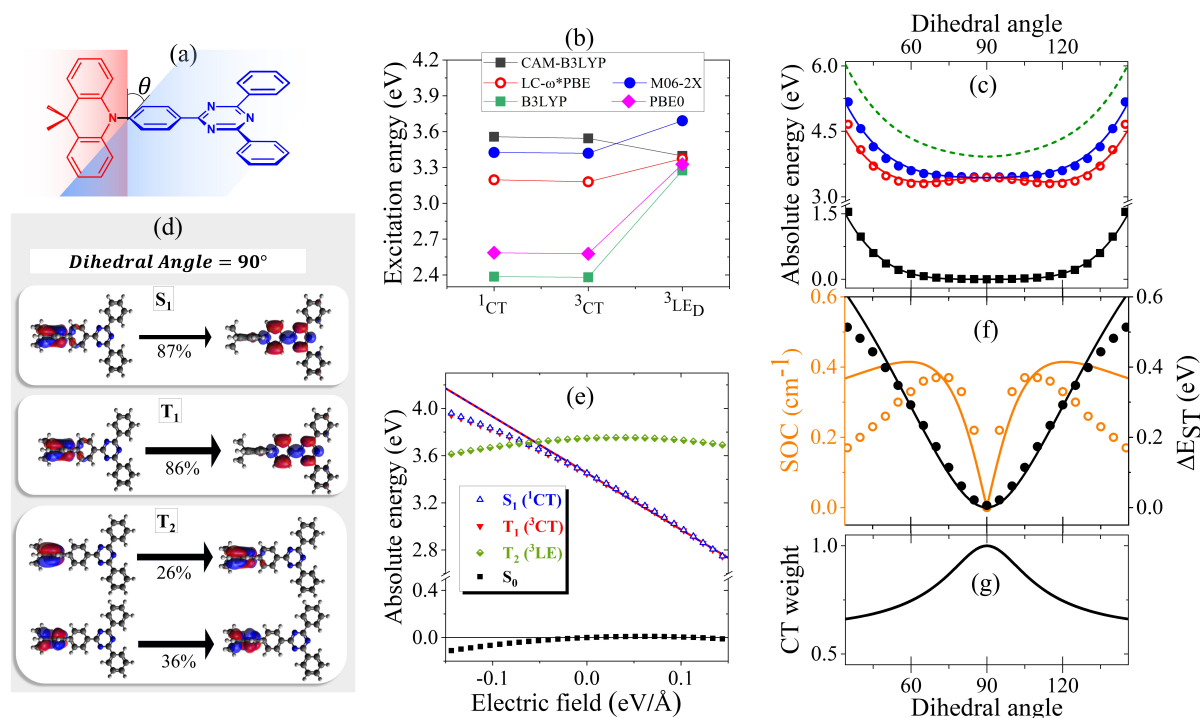
Figure 2.3: (a) a sketch of DMAC-TRZ, showing the dihedral angle, (b) Excitation energies for the three lowest excited states calculated at the equilibrium geometry with different functionals. (c) The energy of the ground (black), lowest excited singlet (blue) and triplet (red) states calculated as a function of θ in TD-DTF (symbols) and ESM (lines). The green dashed line shows the effective LE triplet introduced in the ESM. (d) Natural transition orbitals of the lowest singlet excited state and of the two-lowest triplet states. (e) Energies of the four lowest states as a function of the applied field (f) The singlet-triplet gap (black) and the spin-orbit coupling (orange) between the lowest singlet and triplet states vs θ. Symbols and lines refer to TD-DFT and ESM results, respectively. (g) The weight of the CT state in the lowest triplet as estimated in ESM.

trend as LC-ω*PBE functional for the excitation energies of singlet and triplet states. Results in Figure 2.3b refer to the equilibrium geometry, $\theta = 90°$, but similar results were obtained for few selected values of the dihedral angle (Figure B.1 and Table B.1). On this basis, M06-2X is adopted as functional of choice.

Figure 2.3 summarizes main TD-DFT results. At the equilibrium geometry, the planes of DMAC and TRZ moieties are mutually orthogonal ($\theta = 90°$) and the lowest lying singlet and triplet states (S_1 and T_1, respectively) are almost degenerate. The next excited state T_2, at 3.75 eV (not shown in the figure), is again a triplet. Based on relevant natural transition orbitals (Figure 2.3d) the two lowest and almost degenerate singlet and triplet states are CT states (^{1}CT and ^{3}CT, respectively), while the next excited state is a triplet state localized on donor unit (^{3}LE$_D$). To further confirm the nature of the states, Figure 2.3e shows the evolution of the energies of the lowest states vs an electric field applied along the D-A axis. The energy of the ground (S_0) and of the T_2 state marginally depends on the applied field, suggesting that the two states have a very small permanent dipole moment, confirming the local nature of

T_2. On the opposite, the large and almost linear dependence of the energy of S_1 and T_1 states on the applied field, points to a large and almost constant dipole moment for both states, confirming their CT nature.

To better understand the physics of TADF in DMAC-TRZ, the energies of the relevant states are calculated upon varying the dihedral angle, while keeping the geometry of the two fragments fixed. Results in Figure 2.3c are interesting in several respect. First of all, the potential associated to the ground state and to the first singlet state are fairly flat, suggesting considerable conformational disorder. Moreover, a double-minimum structure is observed for the lowest triplet state: the equilibrium conformation for the relaxed triplet has a twist angle $\theta \sim 60°$ or $120°$. As it will be discussed in the next section, this variation of conformation in the triplet state can only be rationalized accounting for the coupling with some higher energy (local) excited triplet state. Figure 2.3f finally summarizes results of interest for TADF: the θ-dependence of the singlet-triplet gap and of the corresponding spin-orbit coupling. As expected, the singlet-triplet gap increases when the mutual orientation of the D and A planes deviates from orthogonality, and at the same time the spin-orbit coupling first increases, to decrease again for $75° < \theta < 105°$.

The comparison with experiment requires a careful analysis of solvation effects, typically dealt with approximating the solvent as a continuum dielectric medium.[19] However, as discussed in Chapter 1 and specifically for TADF dyes in section 1.5, current implementations of continuum solvation models in quantum chemical packages do not properly account for the role of the solvent electronic polarizability, leading to results that wildly depend on the specific approximation scheme adopted, already in the comparatively simple case of a non-polar solvent. Therefore, in the following Section a minimal model is developed for DMAC-TRZ that will allow us to discuss solvation and matrix effects in a simple and reliable approach.

2.3.2 Setting up the model

In this section, a model for DMAC-TRZ is set up on the basis of the computational results (section 2.3.1) and experimental data (section D.1). In the spirit of essential state models (ESM) (Section 1.6) a minimal set of electronic diabatic basis states is selected to describe the ground and the low-energy excited states.[39, 132–134] As for singlet states, the two-state model, proposed and extensively validated for D-A dyes, [11, 39, 132] and discussed in section 1.6.2, also applies to DMAC-TRZ. In the singlet subspace, the electronic basis states are selected as the neutral DA state, N, and the zwitterionic
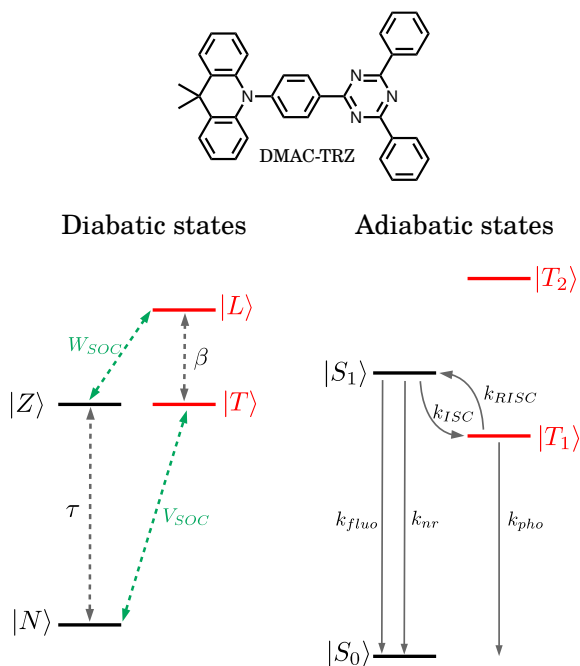
Figure 2.4: Top: Kekulé structure of DMAC-TRZ. Left panel: a schematic view of the four diabatic states and of the relevant mixing matrix elements. Right panel: the four electronic adiabatic states, the arrows mark the relaxation processes of interest.

D$^+$A$^-$ state, Z. The two states are separated by an energy difference $2z$ and are mixed by a matrix element $-\tau$, as sketched in Figure 2.4. As discussed above, the orthogonal configuration of the D and A planes, suggests a vanishing τ at the equilibrium so that the ground state S$_0$ and the first excited state S$_1$ basically coincide with N and Z, respectively.

To account for the lowest triplet state, the basis must be extended to account for the zwitterionic triplet state T. As a consequence of the exact charge separation in the zwitterionic states, the states Z and T are degenerate. Moreover, according to the El-Sayed rule, the spin-orbit coupling between the two states vanishes. A finite spin-orbit coupling V_{soc} instead mixes T with N.

To reproduce the θ dependence of the calculated energies of the excited singlet and triplet states in Figure 2.3c, the spin-orbit coupling V_{soc} is treated as a minor perturbation, so that, at the lowest order, only two electronic parameters enter the three state model: $2z$ whose marginal θ-dependence is neglected, and τ whose dependence on θ is definitely relevant. Information on the $\tau(\theta)$ dependence can be extracted mapping TD-DFT results on ESM. Specifically, in ESM the product between the transition frequency, $\hbar\omega_{CT} = \tau(\theta)/\sqrt{\rho(1-\rho)}$, and the transition dipole moment, $\mu_{CT} = \mu_0/\sqrt{\rho(1-\rho)}$ is proportional to τ:[135]

$$\mu_{CT}\hbar\omega_{CT} = \mu_0\tau(\theta) \qquad (2.1)$$

The dependence of $\tau(\theta)$ is obtained fitting the values of $\mu_{CT}\hbar\omega_{CT}$ predicted using TD-DFT calculations for different values of θ with
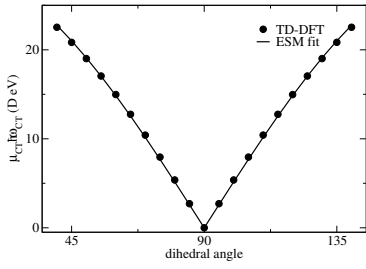
Figure 2.5: TD-DFT results for $\mu_{CT}\hbar\omega_{CT}$ (symbols) fitted with the function $A|\cos\theta|$ (line) with A as fitting parameter.
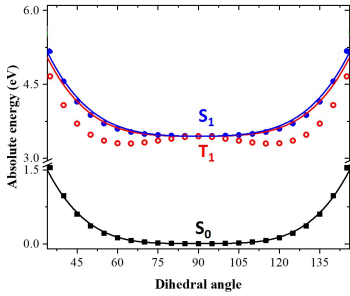
Figure 2.6: Energy of the ground and lowest excited singlet and triplet states calculated as a funcion of θ in TD-DFT (symbols) in the three-state ESM (lines).

the function $f(\theta) = A|\cos(\theta)|$ (Figure 2.5).

Of course, a restoring potential for θ must be introduced, equal for all states, in the hypothesis that state-specific features can be reproduced by the ESM, provided the relevant physics is properly accounted for. The restoring potential is set via an expansion to the fourth order around the equilibrium $V(\delta) = a_2\delta^2 + a_4\delta^4$, where $\delta = \theta - 90°$. The relevant three-state Hamiltonian on the $|N\rangle$, $|Z\rangle$, $|T\rangle$ basis reads:

$$\hat{\mathcal{H}} = \begin{pmatrix} 0 & -\tau_0|\sin\delta| & V_{soc} \\ -\tau_0|\sin\delta| & 2z & 0 \\ V_{soc} & 0 & 2z \end{pmatrix} + a_2\delta^2 + a_4\delta^4 \quad (2.2)$$

Irrespective of model parameters, in the three-state model the triplet state only marginally mixes with the singlet state and therefore the relevant potential energy curve cannot reproduce the double minimum calculated in TD-DFT, as shown in Figure 2.6.

A TD-DFT analysis of the nature of the lowest triplet state shows that it is a pure CT state at $\theta = 90°$, but it acquires some local character when the system deviates from orthogonality (Figure 2.7). Indeed, several local triplet states enter into play and including all of them would lead to an impractical ESM, prone to overfitting. On the other hand, a detailed modelling of high-energy triplet states is not strictly required, as the interest is in capturing the effect of their mixing on T_1. A four-state model is therefore set up, that, besides the three states $|N\rangle$, $|Z\rangle$ and $|T\rangle$, described above, also includes an effective local triplet state $|L\rangle$ whose energy, $2k$ is a free fitting parameter. As for the L-T mixing matrix element, β, the same angular dependence is assumed as for τ, setting $\beta(\theta) = \beta_0|\cos\theta|$ (Figure 2.4). The relevant Hamiltonian, on the $|N\rangle$, $|Z\rangle$, $|T\rangle$ and $|L\rangle$ basis, reads:

$$\hat{\mathcal{H}} = \begin{pmatrix} 0 & -\tau_0|\sin\delta| & V_{soc} & 0 \\ -\tau_0|\sin\delta| & 2z & 0 & W_{soc} \\ V_{soc} & 0 & 2z & -\beta_0|\sin\delta| \\ 0 & W_{soc} & -\beta_0|\sin\delta| & 2k \end{pmatrix} +$$
$$+ a_2\delta^2 + a_4\delta^4 \quad (2.3)$$
$$= \mathcal{H}_{el}(\delta) + a_2\delta^2 + a^4\delta^4$$

The spin-orbit coupling elements, V_{SOC} and W_{SOC}, are very small and do not appreciably affect the calculated potential energy curves. To reproduce TD-DFT results, model parameters are set to the values in Table 2.1. The agreement is very satisfactory (Figure 2.3c), suggesting that the proposed ESM properly captures the low-energy physics of the system. Quite interestingly, the lowest triplet state, the one relevant to TADF, has a pure CT character at $90°$, but it acquires a partial local character at its equilibrium geometry

(Figure 2.3g), as also confirmed by the analysis of the evolution with the dihedral angle of the natural transition orbitals calculated for T_1 state in Figure 2.7.

Since in the ground state equilibrium geometry the states S_0 and T_1 practically coincide with $|N\rangle$ and $|T\rangle$, respectively, $V_{soc} = 3.84 \times 10^{-4}$ eV is set equal to the TD-DFT value for the spin-orbit coupling between S_0 and T_1 states. Finally, the value of $W_{soc} = 1.74 \times 10^{-4}$ eV is adjusted as to best reproduce the θ-dependence of the S_1-T_1 SOC (Figure 2.3f and black line in Figure 2.8). In this case, it is implicitly imposed that V_{SOC} and W_{SOC} have the same sign. However, while the absolute signs of V_{SOC} and W_{SOC} is irrelevant, having the two with the same or opposite sign leads to different results. The red curves in Figure 2.8 are obtained imposing opposite sign for the two SOC matrix elements: it is clear that results are untenable as they lead to a monotonous increase of $|\langle S_1| \mathcal{H}_{SOC} |T_1\rangle|^2$ with $|\delta|$.

Figure 2.7: Natural transition orbitals calculated for T_1 state for different θ values.

2.3.3 Validating the model against steady-state spectra

In this section, the model parametrized against TD-DFT is validated by comparison against experimental spectra reported in Section D.1. Towards this aim, the model must be extended to account for electron-vibration coupling and for solvation effects, as to address the observed vibronic structure and solvatochromism. As already discussed in Section 1.6, ESMs for D-A dyes describe electron-vibration coupling in terms of a single effective coordinate Q that accounts for the different geometry of the neutral and charge-separated diabatic states.[11, 39, 132] For DMAC-TRZ, the frequency of the effective coordinate is easily estimated as $\omega_v \sim 0.18$ eV from the partially resolved vibronic structure of optical spectra in non-polar solvents (Figure D.3). The strength of the coupling is measured by the vibrational relaxation energy, ϵ_v, the energy gained by the charge separated (either Z or T) states upon

Table 2.1: ESM parameters extracted from the fit of the potential energy curves in Figure 2.3c

z (eV)	1.72
τ_0 (eV)	0.75
k (eV)	1.96
β_0 (eV)	0.85
a_2 (eV)	6.00×10^{-5}
a_4 (eV)	1.43×10^{-7}

Figure 2.8: The square modulus of the $\langle S_1| \mathcal{H}_{SOC} |T_1\rangle$ as a function of δ. Black circles show TD-DFT results. The black line show the best fit obtained setting $V_{SOC} = 3.84 \times 10^{-4}$ eV and $W_{SOC} = 1.74 \times 10^{-4}$ eV. Red lines show results for the same V_{SOC} value, but for negative W_{SOC}. Specifically: $W_{SOC} = -1.5 \times 10^{-4}$ eV (continuous line), $W_{SOC} = -1.0 \times 10^{-4}$ eV (dotted line), $W_{SOC} = -0.5 \times 10^{-4}$ eV (dashed line), $W_{SOC} = -0.1 \times 10^{-4}$ eV (dot-dashed line).

4: The vibrational relaxation energy, ϵ_v, is estimated through DFT energy calculations on the isolated donor (D) and acceptor (A) and the respective ionized species, D$^+$ and A$^-$:

$$\epsilon_v = \left(E_{D^+}^{(D)} + E_{A^-}^{(A)}\right) - \left(E_{D^+}^{(D^+)} + E_{A^-}^{(A^-)}\right)$$

where $E_i^{(j)}$ is the energy of i in in the equilibrium structure of j (See Table 2.2). Calculations involving the open-shell systems D$^+$ and A$^-$ adopted unrestricted M06-2X/6-31G(d).

	SCF Energy (a.u.)
$E_{D^+}^{(D)}$	-634.873448021
$E_{D^+}^{(D^+)}$	-634.875775452
$E_{A^-}^{(A)}$	-973.174499157
$E_{A^-}^{(A^-)}$	-973.178453857

Table 2.2: SCF energies of D$^+$ and A$^-$ used to estimate ϵ_v.

relaxation. A value of $\epsilon_v \sim 0.17$ eV is extracted from DFT energies of the isolated D and D$^+$ and A and A$^-$ species.[4]

Introducing electron-vibration coupling, the molecular Hamiltonian is written as

$$\hat{\mathcal{H}}_{mol} = \hat{\mathcal{H}} + \left[-\sqrt{\hbar\omega_v\epsilon_v}\,\hat{Q}\left(|Z\rangle\langle Z| + |T\rangle\langle T|\right) + \frac{\hbar\omega_v}{4}\left(\hat{Q}^2 + \hat{P}^2\right)\right] \tag{2.4}$$

Where $\mathcal{H}$ is the Hamiltonian in eq. 2.3 and the square bracket groups the vibrational terms, $\hat{P}$ being the momentum operator associated to the coordinate $\hat{Q}$.

The reaction field model, discussed in Section 1.2, is adopted to account for interactions between DMAC-TRZ and the surrounding environment, that is described as a continuum elastic medium that responds to the presence of a solute molecule generating at the solute location an electric field, called the reaction field, whose equilibrium value is proportional to the solute dipole moment. As extensively discussed in Section 1.2, two components of the reaction field must be considered, a fast component associated to the electronic polarizability of the solvent and a slow component, of interest for polar solvents, associated with the orientational motion of the solvent molecules. The fast solvation component can be treated in the antiadiabatic approximation (Section 1.4) leading to a renormalization of the z parameter.[9] In the hypothesis that the solute occupies a spherical cavity of radius a inside the solvent, the renormalized z reads:

$$z \rightarrow z - \frac{\mu_0^2}{8\pi\varepsilon_0 a^3}\frac{\eta^2 - 1}{2\eta^2 + 1} \tag{2.5}$$

where ε_0 is the vacuum dielectric constant, η is the solvent refractive index at optical frequencies, a is the cavity radius and μ_0 is the dipole moment associated with zwitterionic (Z and T) states. This corresponds exactly to eq. 1.33 derived in the case of the generic ESM, with $\epsilon_{el} = \mu_0^2 r_{el}/2 = \frac{\mu_0^2}{4\pi\varepsilon_0 a^3}\frac{\eta^2-1}{2\eta^2+1}$ being the electronic solvent relaxation energy.

The Onsager radius is set to $a = 6.44$ Å (0.5 Å larger than the radius corresponding to the computed molecular volume inside a contour of 0.001 electrons/Bohr^3 density).[14] In order to estimate μ_0, the dependence of the excited states with CT character (S$_1$ and T$_1$) on an applied external electric field is exploited, as shown in Figure 2.3e. More precisely, to get rid of the small F-dependence of the ground and local excited states, a value of $\mu_0 \sim 22.71$ D is estimated from a linear fit of the S$_1$ and T$_1$ transition energies.

The slow component of the reaction field F_{or} enters the model as a slow coordinate and can be treated in the adiabatic approximation.

The total Hamiltonian then reads

$$\hat{\mathcal{H}}_{tot} = \hat{\mathcal{H}}^{\eta}_{mol} + \left[-\mu_0 F_{or} \left(|Z\rangle \langle Z| + |T\rangle \langle T| \right) + \frac{1}{2r_{or}} F^2_{or} \right] \quad (2.6)$$

where $\hat{\mathcal{H}}^{\eta}_{mol}$ is the molecular Hamiltonian in Eq. 2.4 with renormalized z as in Eq. 2.5 to account for fast solvation, and the square bracket collects polar solvation terms, with r_{or} defined as

$$r_{or} = \frac{2}{4\pi\epsilon_0 a^3} \left[\frac{\epsilon_{st} - 1}{2\epsilon_{st} + 1} - \frac{\eta^2 - 1}{2\eta^2 + 1} \right] \quad (2.7)$$

where ϵ_{st} is the static dielectric constant of the solvent. The values of η and ϵ_{st} of the solvents of interest are listed in Table 2.3.

The above equations, derived in Ref. [37], were extensively adopted to describe linear and non-linear spectral properties of polar dyes in different environments. In particular, the relation between the restoring force for F_{or} and the relaxation energy, $\epsilon_{or} = \frac{\mu_0^2}{2} r_{or}$ is fixed by imposing that, in each state, the equilibrium F_{or} is proportional to the molecular dipole moment, and in turn proportional to the weight of the zwitterionic states, $|T\rangle$ and $|Z\rangle$:

$$(F_{or})_{eq} = 2\epsilon_{or} \langle |Z\rangle \langle Z| + |T\rangle \langle T| \rangle \quad (2.8)$$

The model Hamiltonian in Eq. 2.6 is solved for fixed F_{or} and δ values, writing the corresponding Hamiltonian matrix on the basis obtained as the direct product of the 4-dimensional electronic basis states times the first M states of the harmonic oscillator associated to the vibrational coordinate $\hat{Q}$.[5] The Hamiltonian matrix is then diagonalized numerically to get vibronic eigenstates. Absorption and fluorescence spectra are computed as described in Appendix A, assigning to each vibronic transition a Gaussian bandshape with a half-width at half-maximum of $\Gamma = 0.08$ eV. Spectra calculated for different F_{or} and δ values are then summed over accounting for their Boltzmann weight with reference to the energy of the ground state for absorption spectra, and of the lowest singlet and triplet states for fluorescence and phosphorescence spectra, respectively.[133]

Calculated absorption and fluorescence spectra in solvents of different polarity are shown in the central panel of Figure 2.9a, while the central panel of Figure 2.9b shows computed fluorescence and fluorescence excitation spectra of DMAC-TRZ in frozen 2MeTHF at 77 K. Absorption and excitation spectra agree well with experimental results (Figure D.3 or top panels of Figure 2.9a and Figure 2.9b) showing negligible solvatochromism. Emission spectra qualitatively agree with experiment, reproducing the observed solvatochromism and the bandshape evolution with solvent

solvent	ϵ_{opt}	ϵ_{st}
Cyclohexane	2.03	2.03
Toluene	2.24	2.38
Chloroform	2.09	4.81
2MeTHF	1.98	6.97
2MeTHF (77K)[a]	2.03	30.5

Table 2.3: Solvent dielectric properties at ambient conditions. The required dielectric parameters for the solvents are taken from the literature (except for 2MeTHF at 77 K) and are listed in Table 2.3.

a: literature data for ϵ_{st} and ϵ_{opt} of glassy 2MeTHF at 77 K are not available. Since the refractive index of organic solvents increases linearly upon decreasing temperature,[136], a value of $\epsilon^{2MeTHF}_{opt}(77\,\text{K}) = 2.016$ is set. As for the static dielectric constant, the effective polarity of 2MeTHF increases with decreasing temperature and, for glassy 2MeTHF at 77 K it is comparable to that of liquid EtOH or DMF,[137] so $\epsilon^{2MeTHF}_{st}(77\,\text{K}) = 30.5$.

5: Typically $M = 10$ ensures convergence.
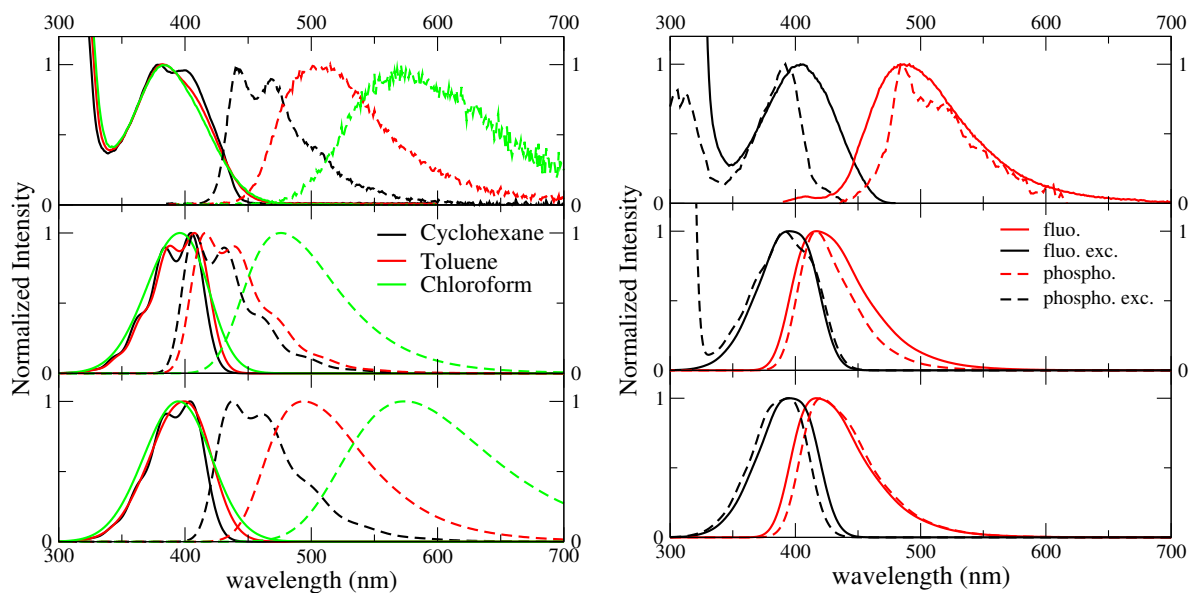
(a) Normalized absorption and fluorescence spectra (continuous and dashed lines, respectively) of DMAC-TRZ in different solvents. Top panel: experimental data as in Figure D.3. Middle panel: calculated spectra (298 K) with ϵ_{or} estimated using eq. 2.7 . Bottom panel: calculated spectra (298 K) adjusting ϵ_{or} as free fitting parameter: $\epsilon_{or}^{\text{Cyclohexane}}$=0.10 eV; $\epsilon_{or}^{\text{Toluene}}$=0.22 eV; $\epsilon_{or}^{\text{Chloroform}}$=0.40 eV, and assigning a HWHM of Γ = 0.03 eV to each transition.

(b) Emission and excitation spectra of DMAC-TRZ in frozen 2MeTHF. Top panel: experimental spectra as in Figure D.3. Middle panel: calculated spectra as in Figure 4(b) main text. Bottom panel: the same as in the middle panel, but with phosphorescence spectra calculated only accounting for the contribution from the CT state.

Figure 2.9: Comparison between theoretical and experimental spectra in (a) liquid and (b) frozen solvent.

polarity. The Stokes shift is however underestimated with respect to experiment, possibly suggesting the presence of other sources of conformational disorder. Quantitative agreement can be obtained if ϵ_{or} is treated as an adjustable parameter, accounting for all relaxation phenomena and relaxing the crude approximation of a spherical solvent cavity (Figure 2.3a).

The calculation of phosphorescence and phosphorescence excitation spectra is more delicate. Phosphorescence is a forbidden process that occurs because spin-orbit coupling generates a very small mixing of singlet and triplet states. As a result, the triplet state *borrows* tiny intensity from the singlet states. The lowest triplet state in DMAC-TRZ is described as the CT triplet plus a minor but non-neglibibile contribution from a local triplet state. Phosphorescence intensity then has a contribution from the (tiny) transition dipole moments associated with CT and LE triplets. Since the transition dipole moments associated with CT states are orders of magnitude smaller than the transition dipole moments associated with LE states, the contribution to phosphorescence from the LE state is assumed to dominate over the contribution from the CT state. This hypothesis is also supported by experimental observation of a decrease of the emission anisotropy at
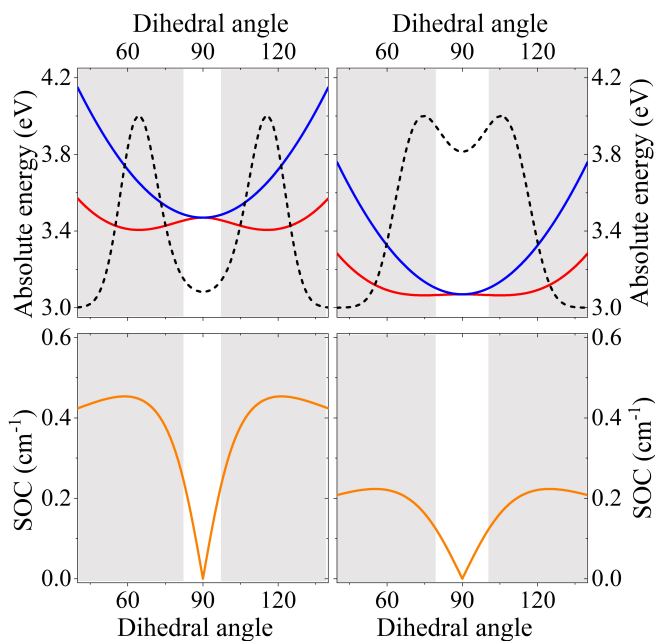
Figure 2.10: Comparison of ESM model results for DMAC-TRZ in the gas phase (left) and in a non-polar matrix with refractive index η = 2 (right). Top panels show the θ-dependence of the energies of the lowest excited singlet (blue) and triplet (red) states. The dotted line show the Boltzmann distribution calculated for the lowest triplet state. Bottom panels show the θ-dependence of the spin-orbit coupling between the lowest excited singlet and triplet states. The shaded areas mark the regions where the singlet-triplet gap is larger than thermal energy at ambient conditions.

very long delay times (Figure D.4a). Accordingly, phosphorescence and phosphorescence excitation spectra in Figure 2.9b (middle panel) are calculated only accounting for the LE contribution to the transition dipole moment. Spectra calculated accounting only for the CT contribution in Figure 2.9b (bottom panel) are in any case very similar. Calculated spectra in Figure 2.9b (middle and bottom panels), referring to glassy 2MeTHF matrix at 77 K, compare well with experimental results (Figure D.3 or top panel of Figure 2.9b). As discussed in the previous section for absorption and fluorescence in liquid solvents, the calculated Stokes shifts are again somewhat underestimated, but a good agreement with experimental results in Figure D.4a is obtained in terms of bandshape and band positions. Phosphorescence intensity is not addressed since it is not accessible experimentally.

The effect of polar solvation on steady state optical spectra of polar dyes are well documented experimentally,[7] well understood in terms of simple solvation models[7, 37, 39, 138] and are reliably addressed in current implementations of continuum solvation models in quantum chemical calculations.[19, 81, 139] On the other hand, as discussed in Chapter 1, the role of the electronic polarizability of the solvent (including liquid solvents and rigid matrices) is more delicate. The marginal variability of the refractive index in common organic matrices makes an experimental analysis very difficult, while available implementations of continuum solvation models in quantum chemical approaches do not treat the corresponding solvation contribution properly, as discussed in the previous Chapter.[9] However a sound understanding of the effects of the

environmental polarizability on TADF-dyes is important in order to concurrently optimize the dye in its matrix, in the so called *smart matrix* approach. Specifically, the important information extracted from quantum chemical calculations for a dye in the gas phase cannot be transferred directly to a solvated dye, not even to a dye in a comparatively simple environment like a non-polar solvent.

To illustrate this issue we estimate how the properties of DMAC-TRZ vary when going from gas phase to a non-polar matrix. To this aim, a non-polar matrix with $\eta = 2$ is taken as and upper limit, with typical refractive index of common organic matrices in the 1.5 - 1.7 range.

Specifically, Figure 2.10 shows the evolution with the dihedral angle, θ, of the energy of the first excited triplet and singlet and of the corresponding spin-orbit coupling. The most apparent effect of the solvent polarizability is a considerable stabilization of CT states. However, the most important effect of the environmental polarizability is expected on the properties that govern TADF. Indeed, since environmental effects are minor for LE states, the energy gap between CT and LE triplet increases, so that overall the spin-orbit coupling decreases, an effect that is clearly unfavorable for TADF applications. There is however another effect of the environmental polarizability: the potential energy curve associated to the lowest triplet is flatter in the matrix than in gas phase. Accordingly, a larger region is found where the singlet-triplet gap is thermally-accessible (the shaded areas in the figure mark the inaccessible regions, those where the gap is larger than thermal energy at ambient conditions). Even more important, because of the shallower potential energy curve for the lowest triplet state, the distribution of θ equilibrated to the lowest triplet state is much broader in the matrix than in the gas phase. This is relevant, since TADF occurs from the equilibrated lowest triplet state and in gas-phase the population of conformations with thermally accessible RISC is marginal, while it becomes sizable in the matrix. Therefore, the overall effect of the solvent polarizability is difficult to assess from a purely qualitative analysis, due to the competition between the decrease of the relevant SOC, and the widening of the thermally-accessible population. In the following section, the effect of the solvent polarizability is quantitatively assessed, through estimates of the rates of interest to the TADF process.

2.4 Calculation of rate constants

The role of molecular vibrations in the TADF process was recognized since the early stages of theoretical research in the field. Indeed, it is well accepted since the 60s, with the work of Marcus,

that non-radiative electron transfer processes occur due to the coupling between the electronic and vibrational degrees of freedom (including molecular vibrations and polar solvation).[36]

In Section 2.3.2, the solution of the molecular Hamiltonian in Eq. 2.4 is obtained treating the vibrational coordinate, Q, in a non-adiabatic approach, while the conformational coordinate, δ is treated in the adiabatic approximation as a classical coordinate. In other terms, the kinetic energy associated with the δ coordinate is neglected, and the coupled electronic-vibrational Hamiltonian is solved for fixed δ values. This approximation is perfectly adequate to address optical spectra, since relevant electronic energies are order of magnitudes larger than conformational energies. However, the tiny singlet-triplet gap of TADF dyes makes the adiabatic treatment of the conformational degree of freedom untenable to address RISC and ISC processes.

Therefore, a full non-adiabatic calculation is set up, rewriting the molecular Hamiltonian for DMAC-TRZ in Eq. 2.4 as

$$\hat{\mathcal{H}}_{mol} = \hat{\mathcal{H}}_{el} + \frac{\hbar\omega_c}{4}\left(\hat{\delta}^2 + \hat{P_c}^2\right) + a_4\hat{\delta}^4 + \frac{\hbar\omega_v}{4}\left(\hat{Q}^2 + \hat{P_v}^2\right) \quad (2.9)$$

where $\hat{\mathcal{H}}_{el}$ is the δ-independent part of electronic Hamiltonian defined in eq. 2.3, and the expansion coefficient a_2 in the restoring potential associated to δ is related to the frequency of the mode $\hbar\omega_c$ as $a_2 = \hbar\omega_c/4$. Moreover, the momentum, $\hat{P_c}$, associated to the conformational coordinate δ, is introduced to account explicitly for the kinetic energy of the δ mode. The Hamiltonian in eq. 2.9 is written on the basis obtained as the direct product of the four electronic diabatic states times the eigenstates of the harmonic oscillator associated with the vibrational coordinate times the eigenstates of the harmonic part of the potential associated with the conformational motion. To this aim, the dimensionless conformational coordinate $\hat{\delta}$ is expressed in second quantization as

$$\hat{\delta} = (\hat{a}^\dagger + \hat{a}) \quad (2.10)$$

where $\hat{a}^\dagger$ ($\hat{a}$) is the creation (annihilation) operator of a vibrational quantum. In the implementation of the calculation, in order to write the Hamiltonian in terms of the creation and annihilation operators, $|\sin(\delta)|$ is expanded up to the third order, to be consistent with the quartic expansion of the potential.[6] Specifically:

$$\sin\delta \sim \delta + \frac{1}{6}\delta^3 \quad (2.11)$$

6: The sign of the mixing matrix elements, τ and β is irrelevant and the absolute value in Eq. 2.3 can be neglected.

Of course, the infinite harmonic oscillator basis associated with δ and Q must be truncated to a large enough number of states as to get convergence on the quantities of interest. As for vibrational

states, the relevant number of states is reasonably small, but the very small frequency associated with the conformational mode requires using a very large number of states, 500-1000, leading to a large overall dimension.[7]

7: Generally, the vibrational basis associated with Q is truncated to 10 bosonic states, while the one associated to δ is truncated to 500-1000 states, for an overall basis dimension of $20000 - 40000$.

2.4.1 RISC and ISC rates

Having a model for DMAC-TRZ and a complete non-adiabatic solution of the relevant Hamiltonian, the calculation of the relaxation rates can now be faced. An elegant approach relies on open quantum systems, coupling the molecular system to a thermal bath, to simulate the energy degradation of the system due to the interaction with the environment. The Redfield bath, a bath of harmonic oscillators, would nicely do the job, allowing to estimate all relaxation energies in a single shot, as discussed for a simpler system in ref. [118]. However the presence of a vibrational and a conformational coordinate, with distinctively different frequencies would require the introduction of two different coupling channels between the molecule and the bath, one for each coordinate. Accordingly, two different spectral densities should be introduced: the relative strength of the couplings and the specific form of the two spectral densities would affect calculated rates in an uncontrolled way. In the lack of specific information on the two spectral densities, this approach cannot provide reliable estimates of the rates of interest for TADF. Therefore, here a step by step approach is adopted, first discussing estimates of RISC and ISC rates and then, in the next section, addressing radiative rates.

RISC and ISC processes are driven by the tiny SOC interactions that can be treated perturbatively. The unperturbed states are therefore obtained from the non-adiabatic diagonalization of the molecular Hamiltonian in Eq. 2.6, setting V_{SOC} and W_{SOC} to zero. In these conditions, the singlet and triplet subspaces are decoupled and the two problems can be treated separately. Red and black lines in Figure 2.11 show the energy levels relevant to the vibronic states in the T_1 and S_1 manifolds, respectively. Since internal conversion is a very fast process (with typical relaxation times $\sim 100\,\mathrm{fs}$), RISC is assumed to occur from the thermally equilibrated T_1 states, the relevant distribution being shown in the right panel of Figure 2.11. The Fermi golden rule (FGR) can then be used to calculate the rate of the transition between states i and j in the two subspaces:

$$v_{ij} = \frac{2\pi}{\hbar} \left| \langle i | \hat{H}_{SOC} | j \rangle \right|^2 S_{ij} \tag{2.12}$$

where $\hat{\mathcal{H}}_{SOC}$ is the SOC part of the Hamiltonian in Eq. 2.6. The energy conserving Dirac-δ in the FGR expression[4] is replaced by S_{ij}, to account for a finite spread in energy of each state, or,
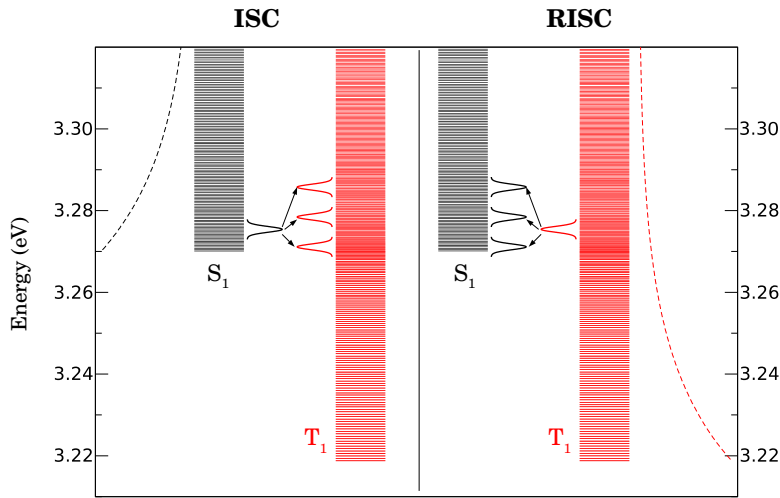
Figure 2.11: A schematic view of the non-adiabatic calculation of ISC (left panel) and RISC (right panel). Red and black lines show the energy levels of the vibronic eigenstates of T_1 and S_1, respectively. In the left panel, the gaussian shape assigned to a specific vibronic state in the S_1 manifold is shown, and the arrows indicate the transition to specific vibronic eigenstates in the T_1 manifold. The global ISC rate is calculated summing on all S_1 eigenstates, accounting for their thermal population (black dashed line in the left panel). RISC rates (right panel) are calculated in a similar way, but summing on all T_1 eigenstates, accounting for their thermal population (red dashed line in the right panel).

equivalently, for the finite lifetime of each state. Specifically, each state is assigned a Gaussian lineshape, whose width, σ, is related to the inverse relaxation time τ_r as follows:

$$\sigma = \frac{1}{2\pi\sqrt{2\ln 2}\,\tau_r} \qquad (2.13)$$

and S_{ij} measures the overlap between the two Gaussians. ISC rates are calculated along the same lines, but starting with vibronic eigenstates in the S_1 manifold, whose thermal distribution is shown as a black dashed line in the left panel.

Figure 2.12 shows RISC and ISC rates calculated as a function of temperature assigning three different values to the lifetime of the vibronic eigenstates: 50 fs, 100 fs and 200 fs, spanning the relevant range. Calculated rates moderately increase with decreasing relaxation time (increasing the width of the energy interval assigned to each vibronic state), but the observed variation is modest. Therefore, results obtained for the intermediate 100 fs relaxation time are discussed in the following Sections. As expected, the RISC rate decreases fast upon decreasing temperature, while ISC rate moderately increases. The singlet triplet gap, ΔE_{ST}, measured as the energy difference between the lowest vibronic state in each subspace, amounts to 0.0513 eV. The microscopic reversibility condition relates the RISC and ISC rates: the dashed line in Figure 2.11 shows the RISC rate evaluated from the ISC rate upon imposing the microscopic reversibility condition:

$$k_{RISC} = \exp\left\{-\frac{\Delta E_{ST}}{k_B T}\right\} k_{ISC} \qquad (2.14)$$

where k_B is the Boltzmann constant. The rates computed using

Figure 2.12: Temperature dependence of calculated RISC and ISC rates. Blue, black and red symbols refer to results obtained imposing a relaxation time for vibronic eigenstates $\tau_r = 50$ fs, 100 fs and 200 fs, respectively. Black open symbols show RISC rates calculated from ISC rates, upon imposing the reversibility condition.
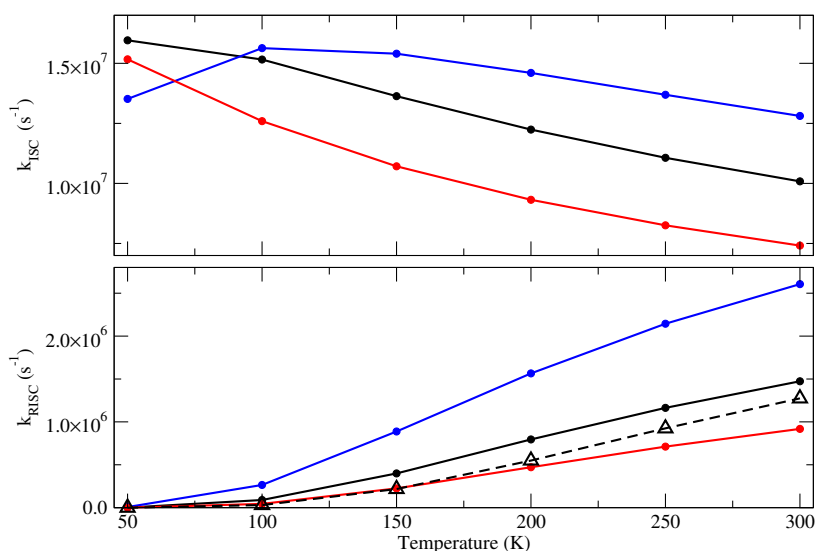
Figure 2.13: Temperature dependence of RISC and ISC rates calculated with model parameters in Table 2.1 (black curve), and multiplying by a factor of 2 either the vibrational frequency ω_v (blue curve) or the a_4 parameter (red curve).
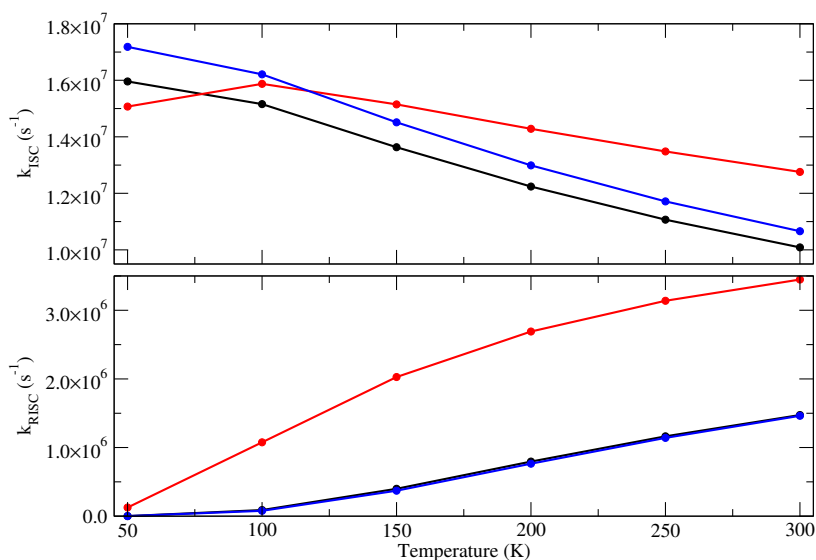
the non-adiabatic FGR approach marginally deviate from the reversibility condition, suggesting that, while the proposed model is very simple, as it only accounts for a single low-frequency mode, the spacing between vibronic level is small enough to accommodate a thermodynamic behavior.

Figure 2.13 shows the temperature dependence of the RISC and ISC rates calculated with the standard model (black symbols) and imposing hardened vibrational or conformational frequencies (blue and black symbols, respectively). The effect on ISC rates is modest, but a hardened frequency of the conformational mode favors RISC, in good qualitative agreement with recent experimental results.[140]

More interesting and intriguing is the dependence of RISC and ISC rates on the energy of the $|L\rangle$ state, as defined by the parameter k. Results in Figure 2.14 show a fairly complex and non-monotonic behavior, suggesting that optimizing the ISC and RISC rates requires
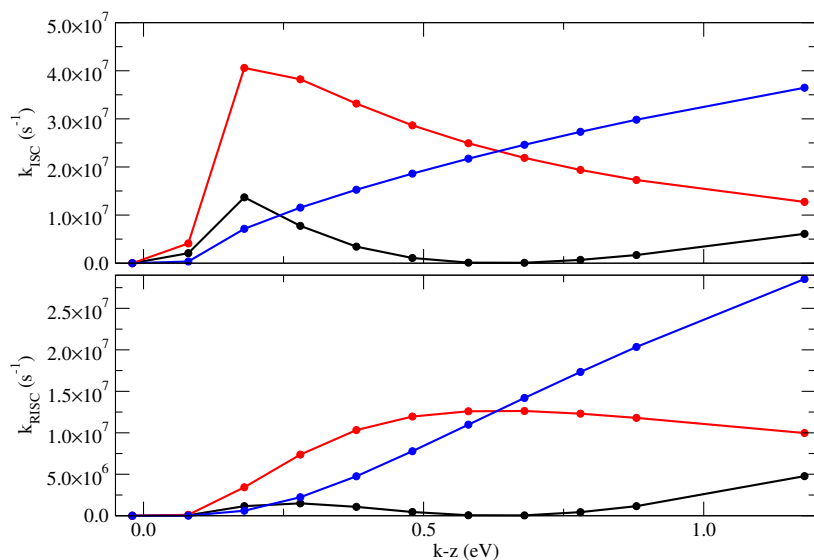
Figure 2.14: The dependence of the RISC and ISC rates calculated for the standard model (black symbols) and by setting either V_{SOC} or W_{SOC} to zero (blue and red symbols, respectively).

a fine tuning of the position of the local excited state, in a way that may strongly depend on the details of the molecular system at hand. Indeed this behaviour, and specifically the valley observed in either RISC and ISC rates at $k \sim 2.35$ eV, originates from the competing contribution from the two SOC channels, mixing N and T states and W_{SOC}, mixing Z and L states, as made evident by results obtained imposing either $V_{SOC} = 0$ or $W_{SOC} = 0$ (red and blue lines in Figure 2.14).

2.4.2 Radiative rates

Fluorescence is an allowed radiative process, occurring from the relaxed excited singlet, S_1 towards vibronic states in the S_0 manifold. The probability of the fluorescence process from state i to state f is calculated again using the FGR, as follows:[4]

$$k_{fi} = \frac{\omega_{fi}^3 \mu_{fi}^2}{3\pi\epsilon_0 \hbar c^3} \qquad (2.15)$$

where ω_{fi} and μ_{fi} are the transition frequency and dipole moment, respectively.

The above equation can be exploited in two different approaches to the fluorescence rate. In the first approach, the complete non-adiabatic diagonalization of the Hamiltonian in Eq. 2.6 identifies i and f into vibronic states (accounting for both vibrational and conformational motions) of the S_1 and S_0 manifold, respectively. The overall contribution of the fluorescence rate from state i in k_{fluo} is then obtained summing over all decay rates towards the f states in the vibronic manifold of S_0. Finally, the overall fluorescence rate is obtained accounting for the thermal distribution of the i states in the equilibrated S_1 manifold. This approach is fairly expensive,

since the full non-adiabatic Hamiltonian must be diagonalized and, to get convergence, it requires including $\sim$ 10 vibrational states and $\sim$ 600 conformational states. Of course calculations may be limited to the two electronic states in the singlet subspace, but the total basis is fairly large, with $\sim 10^4$ states. In an easier approach the conformational mode is dealt with in the adiabatic approximation: neglecting the kinetic energy of the conformational motion, the vibronic Hamiltonian accounting for the coupled electronic and vibrational motions is diagonalized for fixed values of the conformational coordinate δ. The calculation implies the diagonalization of the vibronic Hamiltonian on a basis with dimension $\sim$ 20 on a grid of δ values. For each δ only the lowest eigenstate of the S_1 vibronic manifold, the fluorescent state, is populated (the vibrational energy is very large versus thermal energy). For each δ value, the rate from Eq. 2.15 is summed over the f vibronic states in the S_0 manifold to get the corresponding fluorescence rate, that is finally averaged over the thermal distribution accounting for the δ-dependence of the fluorescent state energy. As expected, since fluorescence occurs between states separated by large energy gaps, the non-adiabatic and adiabatic approaches yield the same results.

The temperature-dependence of calculated fluorescence rates is reported in the bottom panel of Figure 2.17: the calculated rate, of the order of $10^6 \, \text{s}^{-1}$, is fairly small, as expected for S_1 state with dominant CT character. Its decrease with decreasing temperature can be rationalized since the S_1 equilibrium geometry has $\delta = 0$, where the transition dipole moment and hence the radiative rates vanish. As temperature increases, states with finite δ are progressively populated, leading to a progressive increase of the fluorescence rate.

2.4.3 The Marcus model

The Marcus equation is often adopted to calculate RISC rates.[80, 108, 141] However, attention must be payed to the basic approximation underlying the Marcus model. Specifically, the original Marcus model[36, 142] or its generalization to include high frequency molecular vibrations (Marcus-Levich-Jortner, MLJ model[143, 144]), apply to the calculation of transfer rates between two diabatic states, whose energy depends on one or more vibrational and/or conformational and/or solvation coordinates. Relevant potential energy surfaces are usually set as harmonic, with the same frequency but displaced minima (spin-boson model with linear coupling). But the most stringent approximation is that the matrix element that mixes the two diabatic states is constant.[142] However, when applied to RISC rates calculations, the Marcus model is exploited

with reference to adiabatic singlet and triplet states as obtained from quantum chemical calculations. In the adiabatic picture the state-to-state FGR, at the heart of the Marcus model, requires the calculation of the following matrix elements:

$$\langle\psi_i(r,Q)\chi_{i,v}(Q)|\hat{\mathcal{H}}^{SOC}|\psi_f(r,Q)\chi_{f,u}(Q)\rangle=\langle\chi_{i,v}(Q)|\mathcal{H}_{if}^{SOC}(Q)|\chi_{f,u}(Q)\rangle \qquad (2.16)$$

where $\psi_{i/f}(r,Q)$ is the electronic wavefunction relevant to the initial/final state and $\chi_{i/f,v/u}$ is the v/uth vibrational wavefunction relevant to the i/f electronic manifold. The electronic wavefunction describes the motion of electronic coordinates r, and parametrically depends on the nuclear coordinates Q, while the vibrational wavefunctions only depend on Q. In the second term of the above equation an integral over the electronic coordinates allows to define the relevant matrix element of the interaction Hamiltonian:

$$\mathcal{H}_{if}^{SOC}(Q) = \langle\psi_i(r,Q)|\mathcal{H}^{SOC}|\psi_f(r,Q)\rangle_r \qquad (2.17)$$

where $\langle...\rangle_r$ stands for the integral on the electronic coordinates. If $\mathcal{H}_{if}^{SOC}(Q)$ is weakly dependent on Q it can be Taylor-expanded around the equilibrium geometry. The zeroth order term (the Condon term) brings the problem back to the Q-independent interactions characteristic of the Marcus model, so that the Marcus or MLJ equations can be safely applied. However if the Q dependence of $\mathcal{H}_{if}^{SOC}(Q)$ cannot be disregarded, the factorization of the electronic and vibrational problems is more delicate and leads to additional terms (Herzberg-Teller, etc. . .) well beyond the Marcus model.

In the case of DMAC-TRZ as modelled in this Chapter, the Marcus approach relies on the adiabatic solution of the molecular Hamiltonian in Eq. 2.6. The diagonalization of the adiabatic Hamiltonian leads to δ and Q-dependent energies for the four electronic states. Figure 2.15 shows the resulting potential energy surfaces for the S_1 and T_1 states. The two surfaces are degenerate at $\delta = 0°$ where the SOC vanishes, $|\langle S_1|H_{SOC}|T_1\rangle| = 0$. The equilibrium position for the triplet state is found at $\delta = 22°$ and $Q = 1.68$ with energy $E_T = 3.2217$ eV. The singlet minimum is found at $\delta = 0°$ and $Q = 1.92$ with energy $E_S = 3.2700$ eV. The singlet-triplet minimum $\Delta E_{ST} = 0.0485$ eV coincides with the relaxation energy and the activation energy, so that

$$k_{RISC} = \frac{2\pi}{\hbar} \frac{|\langle S_1|H_{SOC}|T_1\rangle|^2}{\sqrt{4\pi\Delta_{ST}k_BT}} \exp\left\{-\frac{\Delta E_{ST}}{k_BT}\right\} \qquad (2.18)$$

where k_B is the Boltzmann constant. Corresponding ISC rates are then estimated imposing the detailed balance. The delicate point is the SOC matrix elements.[56, 80] Indeed the Marcus model is defined on diabatic states, with constant interaction.
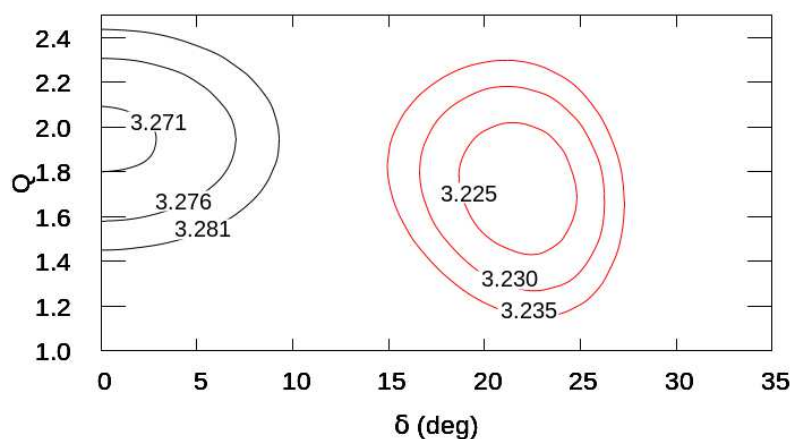
Figure 2.15: Contour plots of the adiabatic potential energy surfaces (eV) relevant to T_1 (red) and S_1 (black) states.
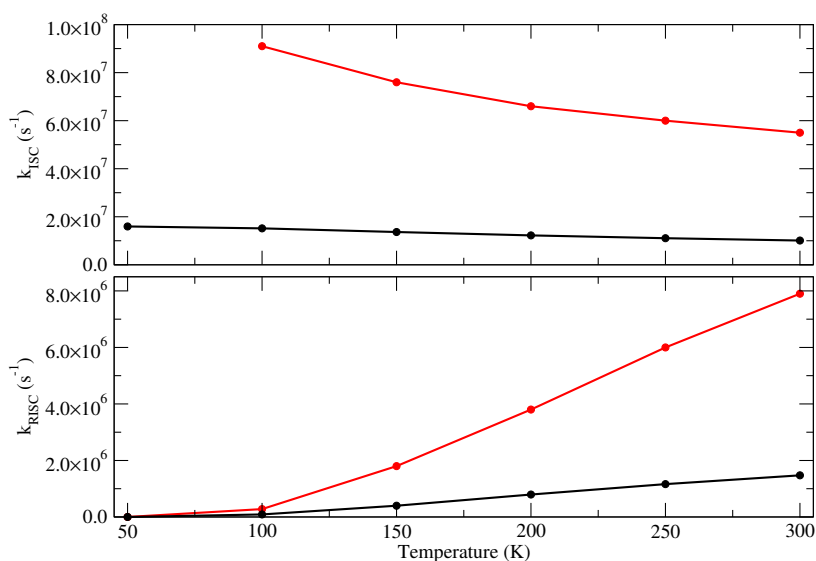
Figure 2.16: The temperature dependence of the RISC and ISC rates calculated for the standard model (black symbols) and in the Marcus model fixing the SOC matrix elements to the value relevant to the equilibrium geometry for the triplet state (red symbols). Setting the SOC matrix element to the value relevant to the singlet-triplet crossing point both RISC and ISC rate would vanish.

Here instead, the model is applied to the adiabatic states and $|\langle S_1| H_{SOC} |T_1\rangle|$ varies with the molecular geometry. Specifically, at the crossing point $|\langle S_1| H_{SOC} |T_1\rangle| = 0$, while at the equilibrium geometry for the triplet state $|\langle S_1| H_{SOC} |T_1\rangle| = 2.66 \times 10^{-5}$ eV. Of course the RISC rate vanishes exactly if the SOC is fixed at the value relevant to the crossing point. Figure 2.16 shows RISC rates calculated with the above equation setting the SOC matrix element to the value calculated at the triplet geometry.

In TADF systems, and specifically in DMAC-TRZ (see Figure 2.8), H_{if}^{SOC} shows a quite impressive δ-dependence as it vanishes at $\delta = 0$, where the singlet-triplet gap closes, and becomes sizeable at intermediate angles and specifically at the triplet equilibrium geometry. Applying the Marcus or MLJ expressions in these conditions represents a strong approximation, explaining the observation in recent literature of wildly different results for RISC rates estimates. Indeed, fixing the $H_{if}^{SOC}(Q)$ to the value relevant to $\delta = 0$ (or in any case to the value obtained where the singlet-triplet gap vanishes) leads to vanishing RISC rates.[141] On the opposite, if

the SOC is set to the value relevant to the equilibrium geometry for the triplet state as in ref. [80] and [145], sizable RISC rates are obtained, that for the specific case of DMAC-TRZ are roughly one order of magnitude larger than in our non-adiabatic calculation (Figure 2.16).

The importance of properly accounting for spin-vibronic terms, well beyond the Marcus or MLJ models, has been very clearly expressed by Penfold *et al.*[146] In their approach, using a diabatic basis, with Q independent SOC among basis states, they regain the Q-dependence of the adiabatic SOC matrix elements accounting for the non-adiabatic mixing of different diabatic states, getting closed formulas thanks to a perturbative treatment. In our essential state model[29] the mixing between the CT and the LE triplets, is parametrized to reproduce the adiabatic Q-dependent SOC interaction and singlet-triplet gap, as obtained from TD-DFT.

2.5 TADF and medium polarizability

TADF phenomena involve molecular excitation in the visible portion of the electromagnetic spectrum. As discussed in Chapter 1, the dielectric response of a generic matrix can therefore be partitioned in two contributions with distinctively different dynamics. The electronic degrees of freedom of the matrix are characterized by timescale in the far-UV region, faster than the molecular degrees of freedom of interest. On the opposite, vibrational and orientational motions of the matrix are much slower. These slow motions only contribute to the dielectric response of the medium in polar matrices, whose role on the photophysics of DMAC-TRZ is analyzed in detail in Section 2.6. In this Section, only the effect of the fast dielectric response is addressed.

Matrices of interest for OLED applications have ε_{opt} spanning a very narrow range comprised between 2.6 and 3.0. Setting the cavity radius to the Onsager radius as done in Section 2.3.3, the renormalized z varies between 1.57 eV and 1.55 eV. Figure 2.17 shows the temperature-dependent rates (ISC, RISC, radiative) calculated in the gas phase ($z = 1.72$ eV) and for the two limiting values of the effective $z = 1.57$ eV and 1.55 eV. Radiative rates are marginally affected by the matrix polarizability, while both RISC and ISC rates decrease considerably when going from gas phase to the matrix, suggesting that gas-phase computational results must be considered with care. On the other hand, the variability of ε_{opt} in common organic media is very limited, so that addressing the effects of the medium polarizability from the experimental perspective is difficult.

Figure 2.17: Temperature dependence of calculated ISC, RISC and fluorescence rates. Black symbols refer to gas phase results ($\varepsilon_{opt} = 1$), blue, and red symbols refer to results for matrices with $\varepsilon_{opt} = 2.6$ and 3.0, respectively. RISC and ISC rates are obtained setting $\tau_r = 100\,\text{fs}$. Normalized non-radiative rates calculated for different ε_{opt} are superimposed in the scale of the figure.
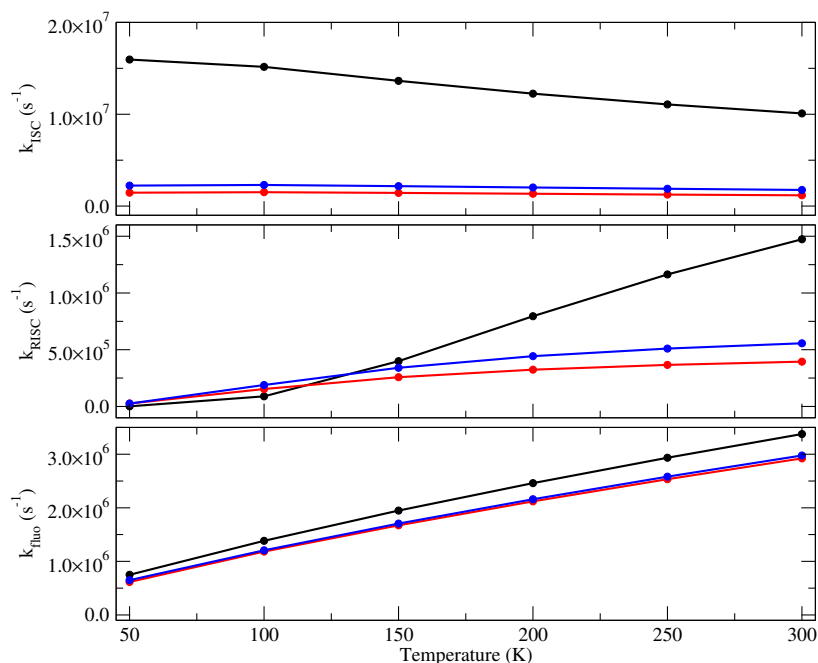
As discussed in Section 2.3.1, RISC and ISC rates are calculated based on SOC matrix elements computed using the Breit-Pauli Hamiltonian as implemented in the ORCA 4.1.[127, 128] Out of the three spin states, finite SOC is computed for only one state, so that a single channel is available for either ISC or RISC. Calculated rates refer to this channel. However, in the hypothesis that the population of the three triplet states is instantaneously equilibrated, the effective RISC rate, to be compared with experiment, must be divided by a factor of 3.[147] Accordingly, the effective RISC rate for DMAC-TRZ in a non-polar matrix is estimated in the $7 \times 10^4 - 2 \times 10^5\,\text{s}^{-1}$ range, in line with experimental results falling in the range $2 - 5 \times 10^5\,\text{s}^{-1}$ in non polar matrices (Zeonex and UGH) as well as in toluene solution.[148] ISC rates are estimated of the order of $2 \times 10^6\,\text{s}^{-1}$ approximately one order of magnitude smaller than experimental results ($\sim 2 \times 10^7\,\text{s}^{-1}$). Calculated radiative rates $\sim 2 \times 10^6\,\text{s}^{-1}$ are again roughly one order of magnitude smaller than the experimental fluorescence rates, that are however also affected by the non-radiative decay. In any case, the overall agreement is satisactory, considering that a model is exploited, defined and parametrized against TD-DFT results and validated against absorption an fluorescence spectra (Section 2.3.2).[29]

2.6 Disorder and polarity in condensed phase

A dye inserted in a dielectric medium (a solvent or a matrix) is affected by the electric potential generated by the medium in response to the presence of the dye. Solvatochromism, i.e. the dependence of the spectral properties of dyes on the solvent, is

the most obvious manifestation of the phenomenon.[7] Models accounting for normal and inverse solvatochromism in polar dyes are known since decades[7, 149] and more detailed treatments also accounting for the evolution of spectral bandshapes have been proposed.[37, 39, 150] In TADF dyes, the phenomena are more complex, since not just the spectra depend on the dielectric properties of the medium,[45, 111] but the ST gap and the SOC interactions are also affected with important and highly non-trivial consequences on the TADF photophysics.[108, 145, 151] To make the issue more complex, delayed fluorescence occurs on very long timescales that, in solid matrices, are possibly comparable to the matrix relaxation times, resulting in a highly non-trivial interplay of interactions.

In this section, the role of a polar environment on the photophysics of TADF is addressed. Relevant degrees of freedom include orientational, conformational and vibrational modes of the environment, that are slow and can be treated in the adiabatic approximation. In the reaction field framework, this amounts to neglecting the kinetic energy associated with F_{or}, in the Hamitonian in eq. 2.6 that describes the dye in a dielectric environment. In DMAC-TRZ the S_0 state is largely neutral and at the equilibrium $F_{or} \sim 0$ in all solvents or matrices. In S_1 instead the molecular dipole moment is large and a sizable equilibrium F_{or} value is expected, that increases with the polarity of the medium (at least as long as the environment can relax after the photoexcitation of the dye). There is however another important effect of polar solvation. Indeed at finite temperature, not just the F_{or}-equilibrated state is populated, but a distribution of F_{or} is expected that can be calculated in terms of a Boltzmann distribution of F_{or}-dependent energies. This distribution is responsible for inhomogeneous broadening phenomena in polar solvents.[37, 39] Indeed in non-polar or weakly polar solvents ϵ_{or} is close to zero, so that the restoring force for F_{or} is very large, leading to narrow distributions around the equilibrium: inhomogeneous broadening due to polar solvation is marginal in these conditions, explaining the partially resolved structure of CT absorption and fluorescence bands of polar dyes in non-polar environments.[39] As the solvent polarity increases, the F_{or}-restoring force decreases and the resulting broader F_{or}-distributions are responsible for the gradual broadening of CT absorption and emission bands with increasing the polarity of the environment.[39] In the specific case of DMAC-TRZ with a largely neutral ground state the distribution is always centered around $F_{or} \sim 0$, but it becomes broader and broader with increasing ϵ_{or}, spanning regions with positive and negative F_{or} (Figure 2.18). S_1 and T_1 states have similar polarity and similar distributions centered at F_{or} values that increase with ϵ_{or}.
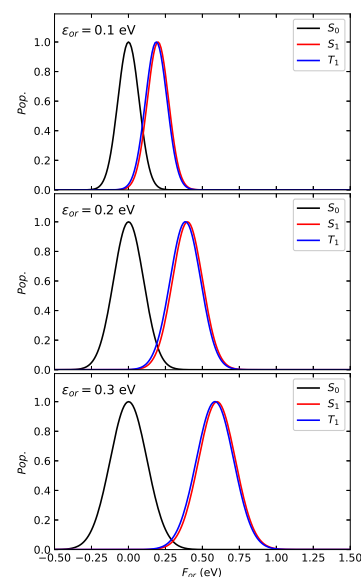
Figure 2.18: F_{or}-dependent distributions of S_0, S_1 and T_1 states of DMAC-TRZ in hypotetical solvents with $\epsilon_{el} = 0$ and ϵ_{or} as specified in each panel.

2.6.1 TADF in liquid solvents

The numerically exact, non-adiabatic solution of the molecular Hamiltonian $\mathcal{H}_{mol}^{\eta}$ in Eq. 2.9 is obtained diagonalizing the Hamiltonian matrix written on the basis direct product of the four diabatic states times the eigenstates of the harmonic oscillators associated with the vibrational and conformation motions.[111] Of course, the oscillator basis must be large enough to reach convergence. As for the vibrational mode, 10-20 basis states are enough, but the very low frequency of the conformational mode requires 600 or more states, for an overall dimension exceeding 20,000 states.

Once the Hamiltonian is diagonalized, the transition frequencies and dipole moments among the vibronic states (the Hamiltonian eigenstates) are calculated to address optical spectra. Specifically, to calculate absorption spectra the lowest vibronic states of the ground state manifold are populated accounting for the Boltzmann distribution. Accordingly, F_{or}-dependent energy and F_{or}-dependent absorption are obtained. Finally, the global absorption spectrum is obtained averaging F_{or}-dependent spectra accounting for the Boltzmann distribution relevant to the F_{or} dependent energy.

To address fluorescence, it must be recognized that in liquid solvents the dynamics associated with slow solvation typically occur in the picosecond time window and is therefore not experimentally accessible through standard time-resolved emission techniques.[8] In any case, solvent relaxation is much faster than fluorescence lifetimes (typically in the nanosecond regime) and steady state fluorescence is dominated by the signal from the excited dye surrounded by the equilibrated solvent. Therefore, the calculation of fluorescence spectra goes along the same lines as absorption spectra, but accounting, for each F_{or}, for the emission resulting from each vibronic state in the excited singlet subspace and averaging over the relevant F_{or} distribution.

Figure 2.9a shows calculated spectra for DMAC-TRZ in different solvents. Table 2.4 lists, for the three solvents, the values of ϵ_{el}, obtained from Eq. 2.5, and of ϵ_{or}, adjusted to best reproduce experimental spectra.[9] While not perfect, the agreement with the experiment is good, in view of the simplicity of the adopted model. Specifically, calculated absorption spectra do not account for high frequency absorption bands that, partly superimposed to the low-frequency band may alter its shape. Absorption spectra calculated treating the conformational mode in the adiabatic approximation coincide with the spectra in Figure 2.9a. Indeed, even if the non-adiabatic calculation does not rely on a static δ-distribution, it implicitly accounts for the disorder on the (dynamical) δ variable (Figure 2.19).[10]

8: To this aim, studies on the early solvation dynamics have been performed using pump-probe techniques, as in ref. [152]

9: To this aim, the solvent relaxation energy ϵ_{or} is considered as a free fit parameter, as done in the bottom panel of Figure 2.9a

10: The area normalized populations of S_0, S_1 and T_1 (Figure 2.19) are calculated as a function of δ for different values of F_{or} at 300 K, accounting for δ as either an adiabatic or a non-diabatic mode.
In the adiabatic limit, the distribution is obtained as

$$P_i(\delta) = \frac{\exp\left(-\frac{E_i(\delta)}{k_b T}\right)}{\int_{-\infty}^{+\infty} d\delta \exp\left(-\frac{E_i(\delta)}{k_b T}\right)}$$

where $E_i(\delta)$ is the potential energy surface, with i running on S_0, S_1 and T_1, the lowest vibronic eigenstates of each respective manifold.
In the non-adiabatic limit, a generic eigenfunction k of eq. 2.9 is:

$$\Psi_k(r,Q,\delta) = \sum_{i,v,p} c_{kivp} \phi_i(r) \chi_v(Q) f_p(\delta)$$

where $c_i v p$ is the coefficient. $\phi_i(r)$ is an electronic basis function and $\chi_v(Q)(f_p(\delta))$ is the vibrational wave function associated to the Q (δ) mode. The non-adiabatic distributions (dotted lines) are computed as:

$$P(\delta) = \sum_k p_k \sum_{ivpp'} c_{kivp}^* c_{kivp'} f_{ivp}^*(\delta) f_{ivp'}(\delta)$$

where

$$p_k = \exp\left(\frac{E_k}{k_b T}\right) / \sum_k \exp\left(\frac{E_k}{k_b T}\right)$$

is the population of the k-th non-adiabatic eigenstate in the manifold of interest.

The adiabatic treatment of δ, that works well for absorption and fluorescence spectra, fails when applied to RISC and ISC calculations since the singlet-triplet gap is comparable to conformational energies. Therefore, as discussed in Section 2.4.1, the complete non-adiabatic Hamiltonian is diagonalized for each F_{or} value and rates among each pair of vibronic states are calculated using the state-by-state Fermi golden rule.[111] The overall rate is finally obtained as the thermal average over the initial state population (the lowest triplet state for RISC and the lowest excited singlet state for ISC). Again the calculations are repeated for different values of F_{or}, to get F_{or}-dependent RISC and ISC rates, relevant results being shown as red and black dashed lines in the three panels of Figure 2.20.

In liquid solvents, the orientational relaxation times are faster than all photophysical processes of interest (fluorescence, non-radiative decay, RISC and ISC). Accordingly, the solvent is always equilibrated with the solute and the overall rate for the generic process from state i to state f can be calculated as the thermal average over the F_{or} distribution equilibrated to the i state.[142] The overall k_{RISC} rate in each solvent is then calculated summing over the F_{or} dependent RISC rates, weighted by the F_{or} distribution equilibrated to T_1. The same calculation is done for the ISC rates, accounting for the F_{or} distribution relevant to S_1 state. Continuous lines in Figure 2.20 show the F_{or}-distribution relevant to T_1 (the S_1 distribution being marginally different). Upon increasing the solvent polarity, the distribution moves towards F_{or} values where both RISC and ISC rates increase, explaining the overall increase of both rates upon increasing the solvent polarity.

Table 2.4 compares calculated RISC and ISC rates with experimental RISC, ISC and fluorescence rates obtained from the biexponential fit of the integrated luminescence intensity measured from diluted (0.8 mM) degassed solutions of DMAC-TRZ in methylcyclohexane, toluene and chloroform (Figure D.9). RISC rates are well in line with experimental results, showing a progressive increase with the solvent polarity. As for ISC, the rates are somewhat underestimated in non-polar solvents and a steady increase of ISC rates is predicted with the solvent polarity, while experimental results point to a marginal dependence of ISC rates on the solvent polarity. Indeed, the model proposed for DMAC-TRZ, and used here as a basis to compute rates, accounts for two effective molecular modes implicitly assuming that the most relevant relaxation mode for both RISC and ISC is the dihedral torsion angle δ. The different trend between between experimental and computed ISC rates with solvent polarity may hint at other efficient relaxation pathways for the $S_1 \rightarrow T_1$ transition, that may involve other molecular motions or electronic states that are not explicitly taken into account in the
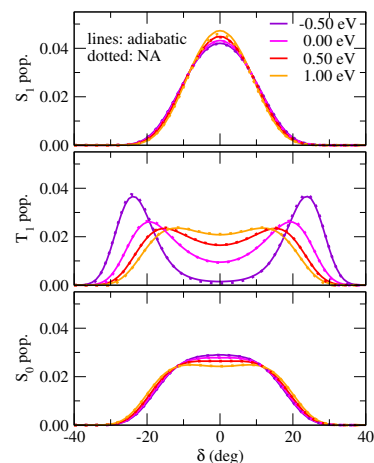
Figure 2.19: Distributions as a function of δ of the S_1, T_1 and S_0 states, accounting for δ as a adiabatic mode (continuous lines) and a non-adiabatic mode (dotted lines), for different values of an external field.

Table 2.4: Solvent parameters (from Ref. [45]), and estimated k_{RISC} and k_{ISC} (s^{-1} units).

	Cyclohexane	Toluene	Chloroform
ϵ_{el} (eV)	0.246	0.242	0.253
ϵ_{or} (eV)	0.10	0.22	0.40
k_{RISC}	4.87×10^4	3.10×10^5	2.19×10^6
k_{RISC}^{exp}	6.05×10^4	2.71×10^5	2.69×10^6
k_{ISC}	4.18×10^5	1.78×10^6	1.11×10^7
k_{ISC}^{exp}	1.33×10^7	2.63×10^7	1.77×10^7

Figure 2.20: Normalized triplet distribution of DMAC-TRZ vs F_{or} (continuous lines) in cyclohexane, toluene and chloroform, superimposed to k_{ISC} and k_{RISC} (red and black dashed lines respectively).
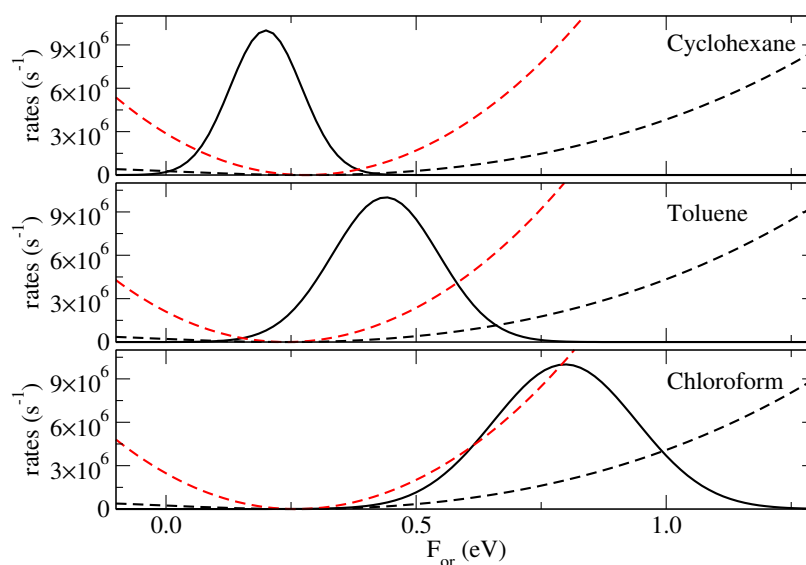
model.

Since in solution all molecular and solvent relaxation processes are much faster than photophysical processes of inerest, emission spectra do not show any appreciable time-dependence (Figure D.8), and the luminescence intensity decay follows a well-behaved biexponential curve, the tail observed at long delays in toluene being ascribed to phosphorescence (Figure D.9).

2.6.2 TADF in organic matrices

Conformational and polar disorder   The photophysics of TADF dyes dispersed in organic matrices (see Figure 2.21 for representative structures) is far more complex than in liquid solutions. Fairly extensive studies are available for DMAC-TRZ in several matrices (Figure D.11).[148] Time resolved emission spectra of DMAC-TRZ in organic amorphous matrices measured at room temperature show a redshift in the first 80-90 ns (prompt fluorescence regime). The magnitude of this initial redshift increases with the host polarity. Moreover, the emission spectrum measured at the first accessible time, $t \sim 2.3$ ns, moves to the red with the host polarity, suggesting a partial host rearrangement in a time scale not experimentally accessible. During delayed fluorescence, the

Figure 2.21: Kekulè structures of the hosts considered in this section.

emission band strongly blueshifts in DPEPO, weakly blueshifts in Zeonex and mCPCN and does not move in mCBPCN (Figure D.11). Moreover, in all matrices a clear non-exponential tail is observed in the time evolution of the emission intensity. This complex behavior points to inhomogeneous broadening effects as well as to a complex interplay between the concurrent dynamics of processes that include fluorescence, phosphorescence, non-radiative decay, RISC, ISC, the conformational motion and the dynamics of the matrix itself. Quite interestingly, non-exponential decays are typically observed in dynamical processes where different species concur to the observed fluorescence or when a slow dynamical process affects the system dynamics.[153–155]

There are two main sources of quasi-static disorder for dyes in matrices. In the first place, the conformational motion of the dye is hindered in rigid matrices and a static distribution of the dihedral angle must be accounted for, rather than a dynamic distribution, as it was the case in liquid solutions. Moreover, in polar matrices, static disorder in the local electric field generated by the configuration of polar groups in the matrix molecules around the dye is an important source of inhomogeneous broadening. In this subsection, the two sources of disorder are addressed separately, in order to understand their role. In the next subsection, the complete system is described in an effort to address experimental data.

Organic matrices are rigid structures that do not allow for the full conformational relaxation of the dye upon relaxation.[54, 56] Moreover, the dye entrapped in the matrix may be frozen in non-equilibrium geometries. To account for the reduced conformational freedom of the dye inside the matrix, the conformational potential in Eq. 2.9 is modified. Specifically, the quartic constant a_4 is set to zero, restoring the harmonic potential, which represents a good approximation for small amplitude motions. Moreover, a stiff potential with a larger ω_c than in solution is imposed. To account for conformational disorder, for each dye in the matrix, small oscillations of the dihedral angle around different equilibrium positions are assumed, so that the conformational potential reads:

$$\frac{\hbar\omega_c}{4}(\delta - \delta_0)^2 \tag{2.19}$$

Gaussian distributions of δ_0 are assumed, in line with results from molecular dynamics calculations,[59] and, to account for the matrix rigidity, the distribution is maintained frozen upon excitation. In the following, results are reported for $\omega_c = 4.0 \times 10^{-3}$ eV, that corresponds to average δ oscillations of about ±3° at ambient temperature. Rates computed for different values of ω_c are shown in Appendix E. Varying ω_c leads to small variations of ISC and RISC rates (Figure E.1), which marginally affect the overall simulation

reported in the next subsection.

Dielectric disorder is more subtle. In liquid solvents the main contributions to polar solvation arises from the tumbling of the polar molecules around the solute. This orientational motion is very fast in liquid solvents (picosecond timescale) but it becomes slow and possibly totally hindered inside the solid matrices of interest. However, partial rearrangements (torsion of small groups or lateral chains, vibrational relaxation) can still occur in matrices in the timescale of interest for the TADF photophysics. Indeed, in polymeric matrices the so-called β-relaxation, related to rotation of polar group around C-C bonds, is typically observed in the nanosecond timescale.[156, 157] Moreover, the vibrational contribution, recently estimated for several matrices from *ab initio* vibrational intensities, accounts for approximately one unit of the dielectric constant and is definitely related to comparatively fast vibrational motions.[158] Accordingly, the orientational reaction field due to polar solvation in matrices is partitioned in two components. The first one is a dynamic component F_{or}^{dyn} that, after photoexcitation, will readjust in response to the charge distribution in the dye in a timescale spanning the fist few nanoseconds, shorter than the timescale of interest for RISC and ISC processes. A second static component F_{or}^{st} will instead be considered frozen, at least in the timescale of interest. While showing different dynamics, and then affecting the time-resolved properties in different ways, at each specific time the properties of the system are defined by the total reaction field $F_{or} = F_{or}^{st} + F_{or}^{dyn}$.

The F_{or} and δ_0-dependent RISC and ISC rates are calculated following the same strategy discussed in section 2.4.1, setting $\epsilon_{el} = 0.28\,\text{eV}$ for all matrices. The radiative rate k_{rad} is finally calculated as a function of F_{or} using eq. 2.15.[4] The color maps in Figure 2.22 show the δ_0 and F_{or} dependence of the singlet-triplet gap and of the rates of RISC ISC and radiative decay. As expected, sizable RISC rates are only calculated in a narrow region of δ_0 whose width varies with F_{or}, but never extends beyond $\delta_0 = \pm 20°$. This region corresponds to the region where the fluorescence rate is minimal. The fluorescence rate shows a monotonic behavior vs F_{or}, while both the RISC and ISC rates show a well-pronounced minimum at $F_{or} \sim 0.3\,\text{eV}$. The other rates entering the dynamical model in Figure 2.4 are set to constant values. Specifically, the non-radiative rate is set as $k_{nr} = 5 \times 10^7\,\text{s}^{-1}$ and the phosphorescence rate as $k_{ph} = 1 \times 10^3\,\text{s}^{-1}$.
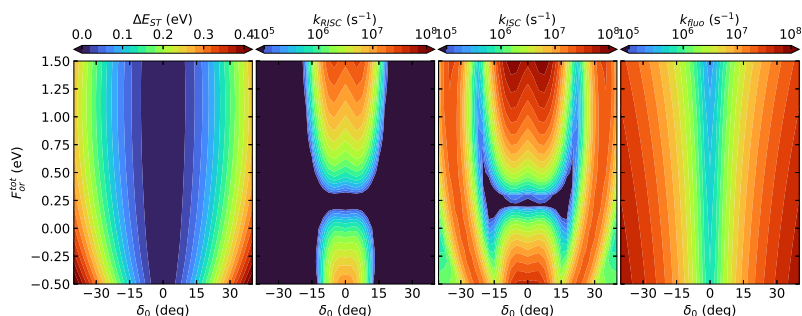
Figure 2.22: The color maps show as a function of F_{or} and δ_0 the singlet triplet gap (leftmost panel) and in a logarithmic scale the calculated rates for $\hbar\omega_c = 4.0 \times 10^{-3}$ eV

Figure 2.23 shows fluorescence spectra calculated for different F_{or} values, each row corresponding to results obtained for different δ_0 values. Normalized spectra are shown, since k_{rad} in Figure 2.22 conveys information about the probability of the fluorescence process. The spectra markedly redshift upon increasing F_{or}, moving from ~ 400 nm to ~ 750 nm. This is of course due to the lowering of the energy of S_1 state, an almost pure CT state, with the field. The concomitant widening of the band is simply related to the choice of showing the spectra against the wavelength. The dihedral angle has a smaller effect on the spectra than F_{or}, but it largely affects the rates (Figure 2.22).

It must be pointed out that neither the rates in Figure 2.22 nor the spectra in Figure 2.23 can be compared directly with experimental data. Indeed, either in solution or inside an organic matrix, conformational and dielectric disorder is present, so that to estimate rates and spectra one must average F_{or} and δ_0-dependent quantities accounting for the relevant δ_0 and F_{or} distributions. Specifically, to simulate the complex photophysics of DMAC-TRZ in matrices, an instantaneous excitation at $t = 0$ is assumed and the time-resolved photophysics of the system is calculated as governed by the dynamical model in Figure 2.4. The calculation is non-trivial due to inhomogeneous broadening and even more due to the presence of a dynamic component of the reaction field.

Therefore, time-resolved emission spectra in organic matrices are computed defining a grid on the static coordinates.[11] In each point of the grid, the time-dependent populations of S_0, S_1 and T_1 states are calculated integrating the dynamical equations:

$$\begin{cases} [\dot{S_1}] = -\left(k_{nr} + k_{fluo}\right)[S_1] + k_{RISC}[T_1] \\ [\dot{T_1}] = k_{ISC}[S_1] - \left(k_{RISC} + k_{phospho}\right)[T_1] \\ [\dot{S_0}] = \left(k_{fluo} + k_{nr}\right)[S_1] + k_{phospho}[T_1] \end{cases} \quad (2.20)$$

where, in the cases where $\epsilon_{or}^{dyn} > 0$, in each point of the grid the rates are obtained as thermal averages over the F_{or}^{dyn} distribution.

Figure 2.23: Normalized fluorescence spectra. In each row, referring to a different δ_0 value, spectra calculated for different F_{or} are shown, colour-coded as defined in the legend.

11: In this case, an equally-spaced monodimensional grid of δ_0 values is used. Analogously, when the role of F_{or} is discussed, a monodimensional grid of F_{or}^{st} values is accounted for. Finally, when the two static modes are both taken into account, a two-dimensional grid on the $\{F_{or}^{st}, \delta_0\}$ space is considered. In all case, uniform spacings of $\Delta F_{or}^{st} = 0.10$ eV and $\Delta\delta_0 = 2.5°$ are used

The integration is performed using the fourth order Runge-Kutta method. Time-resolved emission spectra are then obtained summing relevant (F_{or} and δ_0 dependent) spectra weighted for the instantaneous population of the S_1 state.

To start with, a hypothetical, non-polar medium is considered, where the orientational components of the reaction field vanish. Conformational disorder is then the only source of inhomogeneous broadening. Results in Figure 2.24 are obtained setting a Gaussian distribution of dihedral angles with a standard deviation $\sigma = 15°$. While arbitrary, this distribution compares favorably with the distribution of conformations obtained by a molecular dynamics simulations of DMAC-TRZ in an organic matrix.[59] For comparison, Figure E.2 shows results for a broader distribution.

Panel (b) in Figure 2.24 shows the evolution of the singlet populations calculated for selected δ_0 values. As expected, for large angles ($\delta_0 > 15°$) the singlet population decays with a single exponential, associated with prompt fluorescence. For smaller dihedral angles, the typical biexponential decay is observed, with delayed fluorescence showing up at long times. The largest RISC rates are seen at small angles, indeed k_{RISC} of similar magnitude are calculated for $\delta_0 = 0$ and 5 degrees. The sizable k_{RISC} value calculated at $\delta_0 = 0$ (i.e. fully orthogonal D and A) strikingly contrasts with the widespread Marcus estimate of RISC rates. Indeed, the SOC matrix element connecting the singlet and triplet states vanishes at $\delta_0 = 0°$, i.e. in the orthogonal conformation, so that the Marcus RISC rate should vanish there. However, the Marcus equation applies in the hypothesis that the SOC matrix element is independent of δ, while in DMAC-TRZ (and more generally in TADF dyes) it shows a large δ-dependence. In these conditions, the non-Condon terms, neglected in the Marcus model, give a large contribution to RISC.[111]

Panel (c) shows the overall singlet population (proportional to the fluorescence intensity) calculated as a function of time, accounting for the initial Gaussian δ_0-distribution shown in panel (a). Independent dynamics are calculated in each point on a grid in the δ_0-distribution in panel (b) and are then summed up accounting for the evolving singlet population in each point. The most striking result is the non-exponential decay at long times that is safely ascribed to the inhomogeneous broadening due to the static distribution of the dihedral angle.

Panel (e) shows corresponding time-dependent emission spectra. Here and in the following, the $t = 0$ spectrum is shown, i.e. the spectrum calculated before any relaxation takes place. This spectrum is not experimentally accessible, but it serves as a reference to understand how big the effect of the relaxation is in the different
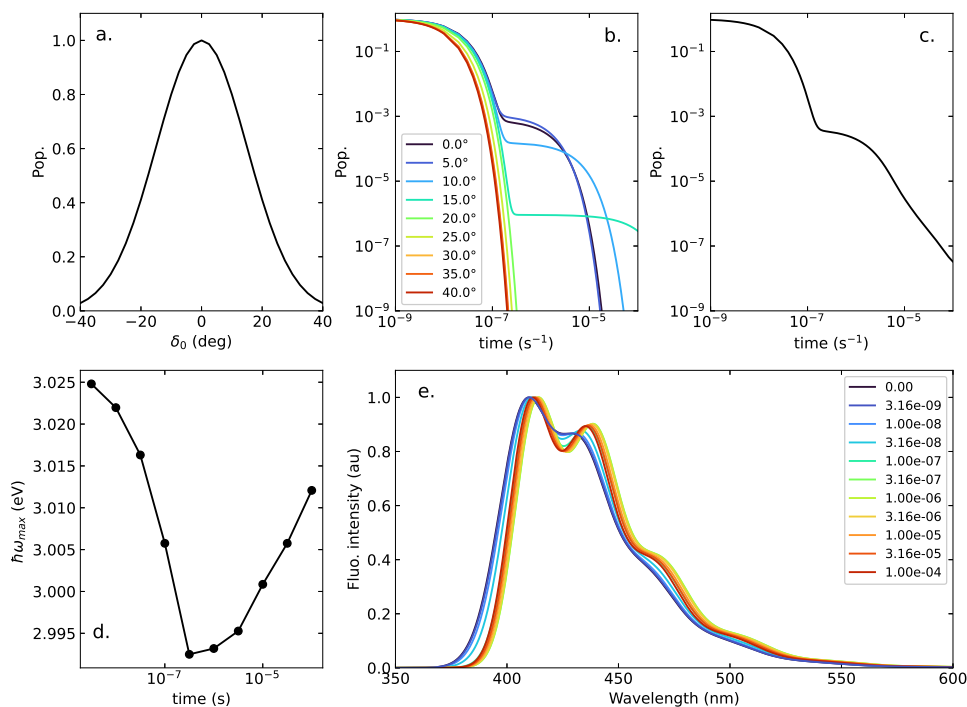
Figure 2.24: The photophysics of DMAC-TRZ in a hypothetical strictly non-polar matrix. (a) the δ_0 static gaussian distribution, with standard deviation of $\sigma = 15°$. (b) the population of the singlet state (proportional to the fluorescence intensity) as a function of time, calculated for selected δ_0 values. (c) the time evolution of the overall singlet state population. (d) the evolution with time of the frequency of the maximum of the fluorescence spectrum. (e) time-resolved fluorescence spectra.

environments. The spectra in Figure 2.24e show a resolved vibronic structure, as expected for an ideal non-polar matrix. The spectra show only marginal shifts in frequency, in line with the minor effect of the dihedral angle on the position of fluorescence spectra, as best appreciated by the data in panel (d) that shows how the maximum of the emission band evolves with time. Results for broader δ_0 distributions are shown in Figure E.2.

Accounting for the dielectric disorder is trickier, as both static and dynamic components must be considered. Figure 2.25 shows results for a hypothetical matrix with $\delta_0 = 0$ and no conformational disorder. As for the static dielectric contribution, a small value is set for the relevant relaxation energy, $\epsilon_{or}^{st} = 0.05$ eV: Figure 2.25a shows the corresponding F_{or}^{st} distribution. RISC occurs from T_1 and ISC from S_1. However, the F_{or} distributions relevant to the two states are very similar, so that for each $(F_{or}^{st}, F_{or}^{dyn})$ values, the distribution is equilibrated to the triplet state, and the rates are averaged along this distribution. Then, for each F_{or}^{st}, the specific dynamics are computed, as shown in Figure 2.25b. The first observation is that TADF becomes more efficient at large fields, even if the global effect of the orientational field is smaller than the effect of the angle. The resulting smaller inhomogeneous broadening reflects in a quasi-biexponential decay of the singlet state population in Figure 2.25c. Therefore, the non-exponential tail seen at long
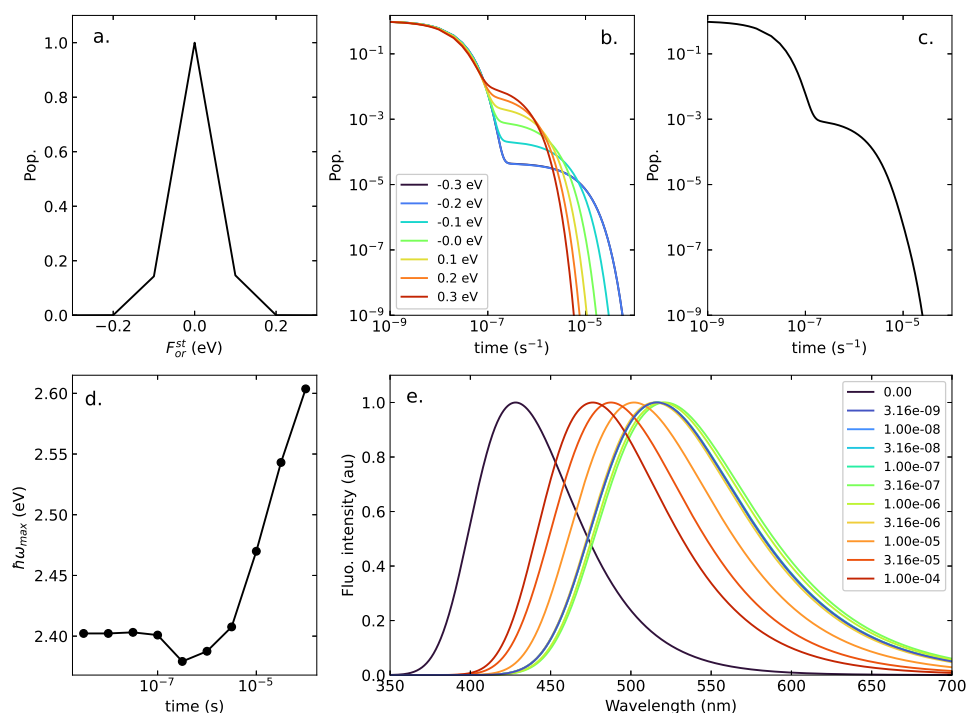
Figure 2.25: The photophysics of DMAC-TRZ in a hypothetical polar matrix with $\epsilon_{or}^{dyn} = 0.25$ eV and $\epsilon_{or}^{st} = 0.05$ eV and without conformational disorder $\delta_0 = 0$. (a) the static F_{or}^{st} distribution. (b) the population of the singlet state as a function of time, calculated for selected F_{or}^{st} values. (c) the time evolution of the overall singlet state population. (d) the evolution with time of the frequency of the maximum of the fluorescence spectrum. (e) time-resolved fluorescence spectra.

times in the experimental emission intensity arises mainly from conformational disorder.

Due to dielectric disorder, time-resolved emission spectra in Figure 2.25e are broad and the vibronic structure is lost. The $t = 0$ spectrum, calculated before the relaxation of the dynamic component of the orientational field, has no experimental counterpart. The first experimentally accessible spectra, typically at few nanoseconds, are collected when the dynamical component of the dielectric field is partially or totally relaxed. In the lack of specific information about the timescale of the dielectric relaxation, the calculated spectra at $t = 0$ and $t \sim 3.16 \times 10^{-9}$ s refer to a system where the dynamical component of the reaction field is unrelaxed and fully relaxed, respectively. The spectral shifts that follow are due to dielectric disorder. As shown in panel Figure 2.25d, minor shifts of the maximum of the emission band are observed during prompt fluorescence. A large redshift is observed at the onset of delayed fluorescence. The anomalous very large blueshift observed at long times, is due to the dominance of states with a large negative F_{or}^{st}, showing largely blueshifted band.

In conclusion, two sources of inhomogeneous broadening must be considered to understand the TADF photophysics in organic matrices: conformational disorder that mainly governs the redshift dur-

ing prompt fluorescence and the appearance of a non-exponential decay tail, and static dielectric disorder that mainly contributes to the spectral shifts during delayed fluorescence. The dynamic dielectric component instead mainly affects the position and shape of emission spectra.

Experimental validation   A detailed comparison with experiment requires specific estimates of matrix parameters. In the lack of dielectric relaxation data for relevant matrices, steady-state spectra of DMAC-TRZ give useful information. Top panel of Figure 2.26 shows steady-state absorption and emission spectra of DMAC-TRZ in different matrices (from Ref. [148]). Absorption spectra are marginally solvatochromic, as expected for a dye with a largely neutral ground state:[7, 37, 39] due to the negligible dipole moment of the dye in the ground state, the reaction field distribution is centered around zero, irrespective of the solvent polarity. Instead, emission spectra progressively redshift with increasing the matrix polarity from Zeonex, to mCBPCN, mCPCN and DPEPO. In DMAC-TRZ the delayed fluorescence represents a marginal fraction (less than 1%) of the emitted light and steady-state spectra are dominated by prompt fluorescence (see Figure D.10). The progressive redshift of the emission band with increasing matrix polarity demonstrates that within the time-window of prompt fluorescence the matrix readjusts at least partially in response to the variation of the dye polarity upon photoexcitation, lowering the excited state energy. Steady-state spectra in Figure 2.26 can then be fitted as in the bottom panel of Figure 2.26 to estimate ϵ_{or}^{dyn} for each matrix, as shown in Table 2.5.
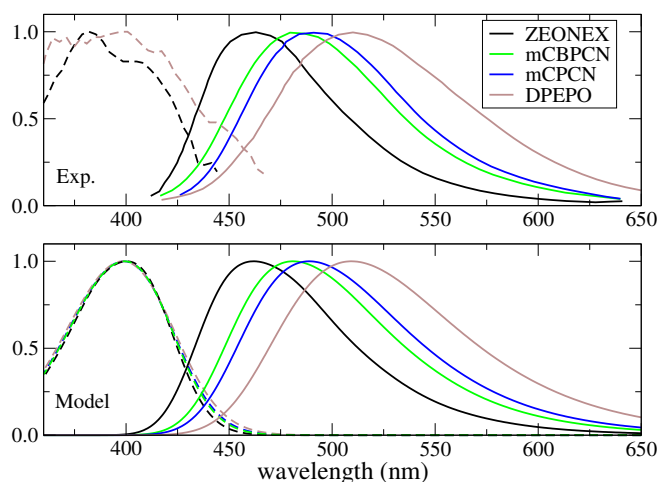
Figure 2.26: Top: experimental absorption (dashed lines) and emission spectra (continuous lines) of DMAC-TRZ in different matrices (from Ref. [148]). Bottom: theoretical absorption (dashed lines) and emission spectra (continuous lines) computed using the solvent parameters as in Table 2.5.

The parametrization of ϵ_{or}^{st} is more delicate. The amount of static disorder depends on the matrix and its preparation (efficiency of packing, freedom to rearrange, amount of disorder, etc...) and on the specific emitter-matrix interaction (uniformity of the

	ZEONEX	mCBPCN	mCPCN	DPEPO
ϵ_{el} (eV)	0.28	0.28	0.28	0.28
ϵ_{or}^{dyn} (eV)	0.13	0.18	0.20	0.25
ϵ_{or}^{st} (eV)	0.01	0.001	0.05	0.05
k_{RISC} (s^{-1})	9.4×10^4	2.9×10^5	4.4×10^5	6.9×10^5
k_{RISC}^{exp} (s^{-1})	1.7×10^5	9.3×10^5	9.6×10^5	1.1×10^6

Figure 2.27: Simulation of the photophysics of DMAC-TRZ in Zeonex matrix, assuming a gaussian distribution for δ_0 with $\sigma = 15°$ (results for a wider distribution and for different ω_c are shown in Appendix E (Figure E.5, E.6, E.9). (a) time-evolution of the singlet population (b) time-evolution of the maximum of the fluorescence spectra (c) time-resolved emission spectra. Time expressed in seconds.
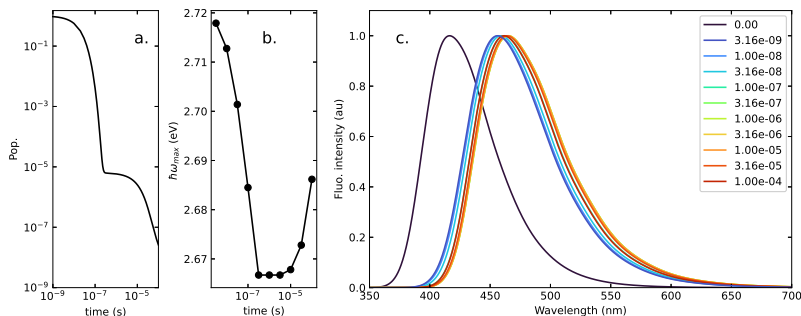
distribution of cavity shape and size).[108, 160] Therefore, ϵ_{or}^{st} is introduced as a free fitting parameter. In all spectra, the δ_0 distribution is set as a Gaussian centered at $\delta = 0$ and with width $\sigma = 15°$ (Figure 2.24a). Results for a broader distribution are shown in Appendix E.

To begin with, results relevant to the Zeonex matrix (Figure 2.27) are discussed. Zeonex is non-polar, but, as discussed above, a small dynamical contribution to ϵ_{or} must be introduced. Since the precise timescale of the relevant dynamics, that may be comprised between few picosecond to few nanosecond, is unknown, the initial dynamics is not simulated. The black curve in Figure 2.27c, shown for reference, refers to the emission spectrum at time zero, originating from the population in the left panel of Figure 2.28, that corresponds to a system where no matrix relaxation has yet occurred. This spectrum is not experimentally accessible and only defines an upper limit for the early time emission spectrum. All other spectra are calculated allowing the dynamical part of the dielectric field to rearrange to the relevant equilibrium distribution (right panel of Figure 2.28). Calculated spectra agree well with the experiment (Figure D.11),[148] showing marginal frequency shifts in time, while the decay curve shows the characteristic non-exponential tail.

Results for DPEPO matrix in Figure 2.29 also agree well with experiment (Figure D.11).[148] The presence of a sizable static dielectric disorder (Figure 2.30) is responsible for a sizable redshift of the emission band, while the conformational disorder defines the non-exponential tail of the emission decay at long time.

The good agreement between calculated and experimental results
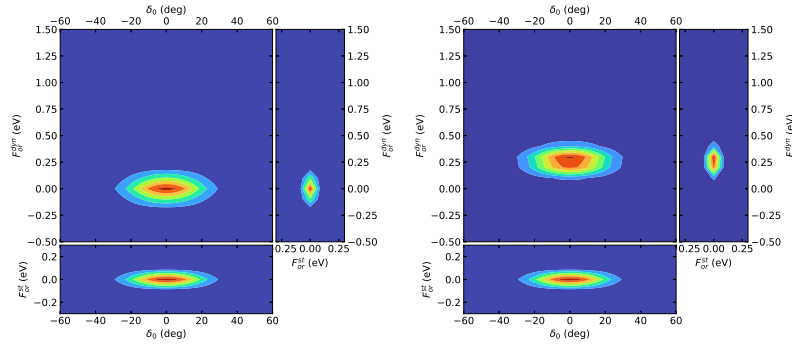
Figure 2.28: Projection of the S_1 population of DMAC-TRZ in Zeonex on the planes spanned by the δ_0, F_{or}^{st} and F_{or}^{dyn} coordinates. Left: immediately after excitation. Right: after the dielectric relaxation along F_{or}^{dyn}.
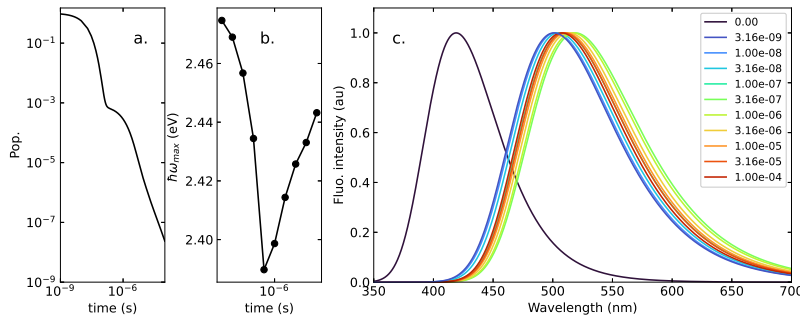
Figure 2.29: Simulation of the photophysics of DMAC-TRZ in DPEPO matrix, assuming a gaussian distribution for δ_0 with $\sigma = 15°$ (results for a wider distribution and for different ω_c are shown in Appendix E, Figure E.7, E.8, E.10). (a) time-evolution of the singlet population (b) time-evolution of the maximum of the fluorescence spectra (c) time-resolved emission spectra. Time expressed in seconds.

collected at room temperature in non polar (zeonex) and polar (DPEPO) matrices validates the model and specifically confirms the role of conformational and polar disorder in the definition of the intriguing spectral behavior of DMAC-TRZ in matrices. Similar results can be obtained in other matrices as well, but a detailed modeling of matrices requires specific hypothesis on the distribution of the dihedral angle, that, in the lack of detailed information, is maintained fixed in all calculation to a Gaussian centered at $\delta_0 = 0$ and $\sigma = 15°$. Similarly, an educated guess is made for the amount of static polar disorder. The amount of conformational and polar disorder actually depends not only on the specific matrix, but also on the sample preparation, hindering a detailed modelization. Simulating temperature effects is also very delicate: polar and conformation disorder are affected by temperature, and the dielectric properties of the matrix itself are temperature dependent.
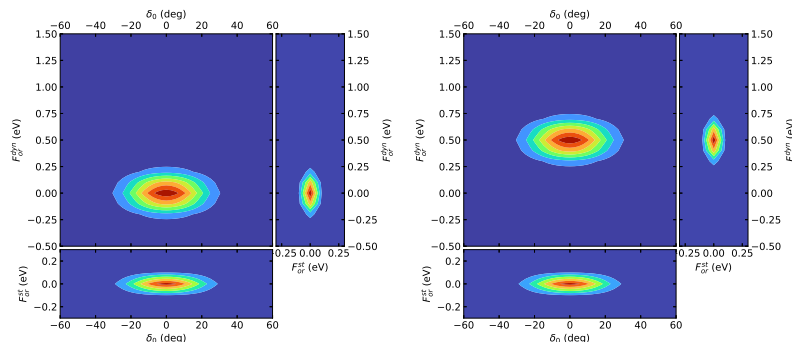
Figure 2.30: Projection of the S_1 population of DMAC-TRZ in DPEPO on the planes spanned by the δ_0, F_{or}^{st} and F_{or}^{dyn} coordinates. Left: immediately after excitation. Right: after the dielectric relaxation along F_{or}^{dyn}.

2.7 Conclusions

In this chapter, a thorough theoretical analysis of DMAC-TRZ, a prototypical dye for TADF applications, is given and supported by experimental characterization (Appendix D). Experimental results unambiguously demonstrate that a state with predominant CT nature is responsible for fluorescence and delayed fluorescence. Phosphorescence occurs in the same spectral region as fluorescence, from a triplet state with dominant CT character. Extensive gas-phase TD-DFT calculations, run in the presence of an applied electric field and for different conformations, confirm the experimental analysis and are exploited to build and parametrize a reliable ESM for DMAC-TRZ. The model accounts for few electronic states, as needed to describe the low-energy properties of the dye, for the coupling to a molecular vibration, needed to simulate the vibronic structure of absorption and fluorescence bands, and for the conformational degrees of freedom associated with the torsional angle that modulates spin-orbit coupling. In Section 2.3.3, environmental effects are addressed to simulate steady-state spectral properties in liquid solution and frozen solvent, accounting for the different role of polar solvation and of the electronic polarizability of the environment. The resulting picture, extensively validated against experiment, offers a sturdy and flexible toy model to investigate TADF.

The approach proposed here for a specific dye is general and can be applied to set up reliable few-state models for other dyes, including multipolar dyes, with multiple D and A groups. The enormous variability of the properties of these dyes, depending on the number and strength of the D and A groups, on bridging units and geometry,[161] calls for the definition of practical models to define reliable structure-properties relationships for the large and technologically relevant family of TADF dyes. The power of few-state models stays in the possibility to account for a large number of interactions that range from vibrational coupling, to be treated in a truly non-adiabatic approach, conformational motion, that can be treated adiabatically to address optical spectra (Section 2.3.3) or non-adiabatically to address ISC and RISC rates (Section 2.4.1), and the interaction with the local environment, accounting for both the dielectric response in terms of polarizability and polarity, and the rigidity, that enter into play when TADF dyes are dispersed in amorphous organic matrices.

In principle, the model also sets the basis to build an open-quantum model[118, 162] for TADF dyes able to address ISC and RISC processes, together with other competitive relaxation processes without introducing additional approximations. However, the definition of spectral densities, governing the coupling between the

system and the bath, is challenging and at present mostly arbitrary. To this aim, classical molecular dynamics offers a promising tool towards the calculation of spectral densities. However, current approaches stem from the field of photosynthetic complexes, so that the system to be coupled with the bath is purely electronic.[163] As discussed at length in this Chapter, molecular modes must be explicitly modelled in TADF dyes, and a highly non-trivial work is needed to properly define the spectral density entering the model for TADF.

Instead of relying on open quantum system approaches, in Section 2.4.1 an alternative approach to the calculation of the rates is proposed, relying on the direct diagonalization of the non-adiabatic Hamiltonian in the singlet and triplet subspaces and the calculation of state-by-tate rates using Fermi's golden rule. The effective model developed for DMAC-TRZ opens the way to a nominally exact calculation of RISC, ISC and radiative rates fully accounting for anharmonicity and non-adiabaticity. It also allows to investigate the effects of a fine-tuning of model parameters. For example it is shown that a softening of the conformational modes has detrimental effects on TADF. Surprising results are also obtained in terms of the dependence of ISC and RISC rates as a function of the relative energies of the $|Z\rangle$ and $|L\rangle$ states, that is highly non-monotonic, suggesting that the common principle of minimizing the energy gap between ^{3}LE and ^{1}CT states may not always lead to an increase of RISC and ISC.

More importantly, we are in the position to address environmental effects on TADF systems. TADF is governed by a subtle interplay of singlet and triplets, LE and CT states: environmental effects, and specifically the medium polarity and polarizability have different effects on the different states affecting the singlet-triplet gap as well as the mixing between the LE and CT triplets with large effects on SOC. A rationalization of these highly non trivial effects is however difficult as several protocols are presently available leading to contrasting results, as recently well illustrated by Mewes.[145] The origin of the contrasting results for environmental effects on TADF (and more generally on the definition of spectral properties of molecules in condensed media) can be traced back to the improper treatment of the medium polarizability. Specifically, either continuum solvation models (including PCM, COSMO, etc. . .) or atomistic solvation models treat the environmental polarizability in an adiabatic approach, solving the molecular Hamiltonian for fixed environmental charges.[9, 29] This approximation is well suited for polar solvation, related to very slow degrees of freedom, but fails when applied to the environmental polarizability, related to the very fast electronic motion in the medium. This leads to a variety of solvation models, none of which is able to properly

address the effect of the medium polarizability. The problem is overcome here adopting an antiadiabatic approach to address the medium polarizability.[9]

In Section 2.5, the role of the matrix polarizability is addressed, as measured by the refractive index at the optical frequencies. The marginal variability of the refractive index in common organic solvents and matrices suggests that it is impossible to optimize the TADF behavior of a dye acting on the medium refractive index. However it is extremely important to recognize that when going from gas phase to an organic medium, the large variation of the refractive index has enormous effects on the energies of the excited state and more generally on TADF. It is therefore of little use to compare results obtained from gas-phase calculations with experimental data in condensed phases. As already recognized by Mewes[145], indeed, RISC rates may vary by orders of magnitude when going from gas phase to a non-polar organic medium. Quite interestingly, for DMAC-TRZ, RISC and ISC rates decrease by approximately one order of magnitude when going from gas phase to the organic medium, even if the singlet triplet gap decreases. The reason for less effective RISC in the medium can be traced back to the stabilisation of CT states, that leading to a decoupling of the CT and LE triplet and hence to a decrease of SOC. Quite interestingly, the opposite behavior is observed by Mewes, with RISC rates increasing by a few order of magnitude from gas phase to condensed media. Apart from the use of a different solvation model, we believe that this contrasting result is indeed related to the different nature of excited states in the molecules investigated by Mewes with respect to DMAC-TRZ.[145] In the molecules investigated by Mewes,[145] in fact, in gas phase, the LE triplet lays lower in energy than the CT triplet, but the order is reversed in non-polar matrices, leading to a large amplification of RISC when accounting for the medium polarizability.

In section 2.6, the model developed in Section 2.3.2 and the approach proposed to calculate the rates described in Section 2.11, are exploited in an effort to paint a comprehensive picture that rationalizes in a single unifying theoretical scheme the TADF photophysics of the dye dispersed in liquid solvents and in organic matrices of different polarity.

As already discussed, polarizability and polarity effects are related to degrees of freedom with distinctively different timescales, and must be treated accordingly.[9] Polarizability, related to the fast electronic degrees of freedom of the medium, alters the molecular properties but is not a source of inhomogeneity. The environmental polarity instead, associated to slow vibrational and conformational motions, is a powerful source of inhomogeneity. In liquid solvents, the dielectric relaxation is faster than prompt fluorescence and is

easily addressed, with inhomogeneous broadening phenomena only showing up in the progressive broadening of spectral features with the solvent polarity.

In organic matrices the problem is much more complex. Spectra collected in diluted samples are discussed, where we can neglect aggregation phenomena as well as self-absorption, also in view of the small extinction coefficient of DMAC-TRZ. Spectral diffusion due to energy transfer can also be excluded at these concentrations. Optical spectra collected in these conditions then clearly show that organic matrices do relax in the timescale of prompt fluorescence. Of course, this relaxation is only partial and is most probably slower than in liquid solvents, but, the progressive redshift of steady-state emission spectra with the matrix polarity (Figure 2.26) offers a clear indication in this direction.

More delicate are the two sources of static disorder, related to dielectric disorder in polar matrices and to conformational disorder.[164, 165] These two sources of disorder concur to define highly non-trivial inhomogeneous broadening phenomena in the TADF photophysics in organic matrices: the non-exponential tail of the emission decay at long delays is essentially due to conformational disorder. The complex temporal evolution of the spectra position and shape is due to the intertwined effect of static conformational and dielectric disorder.

Overall, the excellent agreement with experimental data suggests that the proposed model fully addresses the basic physics of TADF, and is able to capture the subtle interplay between electronic, spin, vibrational and conformational degrees of freedom of the molecule embedded in a polar and polarizable (partially) rigid matrix, as to explain subtle dynamical phenomena.

This work sets a solid basis for a detailed modeling of TADF-OLED, offering reliable information about the variation of the RISC, ISC and fluorescence rates with the local environment and opening a new perspective about the need to account for static and dynamic conformational and dielectric disorder whose highly non-trivial effects must be properly addressed to govern the device behavior.

Conclusions and future outlook

The problem of assessing the effect of the surrounding environment on the properties of a molecule is ubiquitous in materials science. Moreover, in the field of optical spectroscopy, with the exception of crystals and liquid crystals, dyes are typically dispersed in a disordered environment, be it a liquid solvent, an amorphous matrix of organic molecules, or a biological environment. To describe these systems, implicit solvation models proved particularly valuable, allowing for the prediction of the properties of solvated dyes at a moderate computational cost. This thesis discusses the behaviour of organic dyes in condensed phase, focusing the attention on dyes capable of thermally-activated delayed fluorescence (TADF). TADF is a rare phenomenon that occurs in systems where singlet and triplet states sit very close in energy (the gaps being comparable to the thermal energy), so that a system in an excited triplet state can undergo a spin-crossover process, called RISC, and be converted in an emissive singlet state. The main application for TADF dyes is as emitters in OLED, where the TADF activity can be exploited to harvest light from the triplet population of excitons, to overcome the limit of 25% internal quantum efficiency dictated by spin recombination statistics. In OLEDs, TADF dyes are dispersed in amorphous matrices, and understanding how the matrix affects the properties of the dye is not only interesting for basic research, but is also desirable for the optimization of the device, as the performance of the dye may be enhanced or deteriorated by the environment in which the dye is dispersed.

In this thesis, and in particular in Chapter 1, a very fundamental issue is addressed: the response of electronic degrees of freedom of the environment, i.e. the medium polarizability, to electronic transitions occurring in the solute. Electronic solvation is not only a general topic, but also an ubiquitous one, as the environment electronic degrees of freedom are ever present, so that the properties of the solute are expected to be altered when going from gas phase, where calculations are reliable, to condensed phase. In this work, the electronic solvent degrees of freedom are coupled to the solute electronic degrees of freedom in an antiadiabatic approach. In contrast, current implementations of quantum-classical solvation models adopt the adiabatic approximation to electronic solvation, leading to the proliferation of approximation schemes, that often lead to spurious results, as is the case of some TADF emitters, where a negative singlet-triplet gap is predicted (Section 1.5), or in symmetric systems, where spurious symmetry breaking phenomena are wrongly predicted (Section 1.6). The antiadiabatic approach presented in this work is built on the well-known reaction field model. The reaction field model relies on several approximations: (1) the solvent is a continuum elastic medium (2) the solute is treated as a point dipole occupying a cavity; and (3) the solute-solvent interaction is truncated to the dipolar term. An antiadiabatic approach that goes beyond the limits of the reaction field model is therefore desirable to study atomistic systems in realistic surroundings, described either as a continuum with solute-adapted cavity or explicitly with molecular mechanics. Specifically, there are some cases where the reaction field model is expected to fail, such as for solutes with large dimensions, that cannot be described as point dipoles, and ionic species, where the monopole term is the leading term in the multipole expansion. In collaboration with Dr. Gabriele D'Avino, we are developing an antiadiabatic approach that can be applied on atomistic systems.

In Chapter 2, TADF is directly addressed by modelling a prototypical TADF emitter, DMAC-TRZ. An essential state model that accounts for four electronic states, a vibrational mode and a conformational

mode is parametrized on *first principle* calculations and validated against experiment. The model is extended to account for dielectric solvation adopting the reaction field model and the antiadiabatic and adiabatic approximation for electronic and orientational degrees of freedom of the environment respectively. An approach to the calculation of RISC and ISC that relies on the full non-adiabatic solution of the model Hamiltonian is developed, that overcomes the limits of the Marcus and Marcus-Levich-Jortner models. Finally, the role of the environment is tackled considering two regimes: the liquid solvent regime, and the amorphous matrix regime. Orientational dynamics in liquid solvents is straightforward, as it occurs on a timescale much faster than RISC, ISC and radiative decay. Amorphous matrices are instead more complex, as two mechanisms affect the properties of the emitter and must be taken into account. (1) Solid state solvation is due to the dielectric response of the matrix spanning different timescales: the rotation of the host molecules is hindered, but small conformational changes can still undergo on timescales comparable or faster than RISC, ISC and radiative decay. (2) The rigidity of the matrix can hinder some internal motions of the emitter, leading to conformational disorder. Both solid state solvation and matrix rigidity must be taken into account to properly address the photophysics of DMAC-TRZ in matrices. The model proposed to address TADF in solution and amorphous matrices, validated against experiment for DMAC-TRZ will be applied to other TADF systems also with the support of MD simulations to more accurately address the role of the matrix rigidity.

Details on the calculation of steady-state spectra | A

In this appendix, the calculation of absorption and emission spectra is discussed. The approach is generic and applies for the calculation of spectra involving transitions between purely electronic states, as well as vibronic states.

A Gaussian bandshape with half-width at half maximum, $\Gamma = \sqrt{2\ln 2}\sigma$ is assigned to each transition to simulate homogeneous broadening that originates from the finite lifetime of excited states and intrinsic instrumental factors. The extinction coefficient (ϵ) and fluorescence intensity (I) are computed as a function of the wavenumber ($\tilde{\nu}$ in cm^{-1}) as:

$$\epsilon\left(\tilde{\nu}\right) = \frac{10\pi N_A \tilde{\nu}}{3\ln 10 \hbar c \epsilon_0} \frac{1}{\sqrt{2\pi}\sigma} \sum_n \mu_{gn}^2 \exp\left[-\frac{1}{2}\left(\frac{\tilde{\nu}_{gn} - \tilde{\nu}}{\sigma}\right)^2\right] \qquad \text{(A.1)}$$

$$I\left(\tilde{\nu}\right) \propto \tilde{\nu}^3 \frac{1}{\sqrt{2\pi}\sigma} \sum_n \mu_{fn}^2 \exp\left[-\frac{1}{2}\left(\frac{\tilde{\nu}_{fn} - \tilde{\nu}}{\sigma}\right)^2\right] \qquad \text{(A.2)}$$

where N_A is the Avogadro's number, c is the speed of light, ϵ_0 is the vacuum permittivity, $\tilde{\nu}_{in}$ and μ_{in} are the transition wavenumber and transition dipole moment associated to the transition between vibronic states i and n. In absorption, $i = g$ is the ground state and the summation runs over all other eigenstates. In fluorescence $i = f$ is the fluorescent state and the summation runs over all the eigenstates having lower energy than the fluorescent state. The fluorescent state is generally chosen as the first excited singlet with a sizeable transition dipole moment towards the ground state. When the transition dipole moment is vanishing, as for TADF dyes where $\rho \rightarrow 0$, the fluorescent state is chosen as the first excited state with a sizeable $\langle \hat{\rho} \rangle$. Phosphorescence spectra are computed using eq. A.2, where f is the phosphorescent state, chosen as the lowest triplet state.

If the chormophore is dissolved in a polar solvent, this process is repeated for each value of $F_{or}^{(i)}$ where i counts the components of the orientational field, being $i = 1$ for linear molecules, or $i = 1, 2$ for bent quadrupolar or octupolar dyes. Finally, the spectrum is obtained as the weighted sum of the F_{or}-dependent spectra, accounting for the Bolzmann F_{or}-distribution relevant to the ground or fluorescent states for absorption and fluoresecence spectra, respectively.

Quantum chemical techniques | **B**

B.0.1 Density functional theory

Density Functional Theory (DFT) is an alternative approach to older computational methods, such as Hartree-Fock and post-HF theories. DFT gained popularity mainly because of its low computational cost when compared to the accuracy of the results. DFT only addresses the ground state, but its time-dependent extension, TD-DFT, also gives information on excited states (see Section B.0.2.

The theoretical basis of DFT was set well before its practical implementation, with the Hohenberg-Kohn theorems stating that (1) the energy of the ground state is a unique functional of the electron density and (2) the exact electron density of the ground state minimizes the energy functional:

$$E_0 = E[\rho_0] \tag{B.1}$$

$$E[\rho_0] \leqslant E[\tilde{\rho}] \tag{B.2}$$

where ρ_0 and $\tilde{\rho}$ are the exact and approximate electron densities of the ground state, respectively. The energy functional is expressed as

$$E[\rho] = V_{ne}[\rho] + T[\rho] + V_{ee}[\rho] \tag{B.3}$$

where $V_{ne}[\rho]$ is the functional that describes the interaction potential between electrons and nuclei, $T[\rho]$ is the kinetic energy functional and $V_{ee}[\rho]$ is the electron-electron interaction functional. The last two terms are problematic to compute and are grouped in the Hohenberg-Kohn functional, $F_{HK}[\rho]$, that is to be determined. The approximate solution is given by the Kohn-Sham method which introduces an auxiliary system (AS) of non-interacting electrons, whose wavefunction, Ψ_{KS} is a single Slater determinant of spin orbitals χ_i:

$$\Psi_{KS} = \frac{1}{\sqrt{N}} \det |\chi_1(\mathbf{x}_1), \chi_2(\mathbf{x}_2), \dots, \chi_N(\mathbf{x}_N)| \tag{B.4}$$

with known electron density, $\rho_s(\mathbf{x})$ and kinetic energy T_s:

$$\rho_s(\mathbf{x}) = \sum_{i=1}^{N} |\chi_i(\mathbf{r})|^2 \tag{B.5}$$

$$T_s = \langle \Psi_{KS}| \hat{T} |\Psi_{KS} \rangle. \tag{B.6}$$

where N is the total number of electrons. The independent electrons of the AS are solution of an effective single-electron Hamiltonian,

$\hat{h}_{KS}$, as follows

$$\hat{h}_{KS} = \frac{1}{2}\nabla^2 - v_{KS}(\mathbf{r}) \tag{B.7}$$

where the single-electron potential, $v_{KS}(\mathbf{r})$, is determined in order to make ρ_s equal to the electron density of the real system made up of multually interacting electrons.

The energy of the real system can be expressed as

$$E^{KS}[\rho] = T_s[\rho] + V_{ne}[\rho] + J[\rho] + E_{XC}[\rho] \tag{B.8}$$

where the first three terms are known and represent respectively the kinetic energy of AS, the electron-nuclei potential energy and the classical electron-electron repulsion energy. The last term is given by

$$E_{XC}[\rho] = (T[\rho] - T_s[\rho]) + (E_{ee}[\rho] - J[\rho]) \tag{B.9}$$

and includes Coulomb and exchange correlation terms (second term) as well as the kinetic correlation energy (first term), that is often negligible. The energy of the AS is variationally minimized by determining the appropriate set of orthogonal orbitals, via an iterative procedure to obtain the Kohn-Sham orbitals. The Kohn-Sham Hamiltonian in eq. B.7 can be expressed as

$$\hat{h}_{KS} = T_s[\rho] + v_{ne}[\rho] + \sum_{i}^{N} J_i[\rho] + v_{XC}[\rho] \tag{B.10}$$

where the effective potential operator has been written in terms of the nuclear contribution, the classical electron repulsion and the exchange-correlation potential, obtained as the derivative of $E_{XC}[\rho]$ with respect to the electron density. While the first three terms of eq. B.10 are known, the expression for the functional $E_{XC}[\rho]$ and consequently $v_{XC}[\rho]$ are unknown.

Therefore, when performing a DFT calculations, one must select a specific functional, as well as the basis set for the expansion of molecular orbitals. Regardless of the type of functional, $E_{XC}[\rho]$ is expressed as

$$E_{XC}[\rho] = E_X[\rho] + E_C[\rho] \tag{B.11}$$

where $E_X[\rho]$ and $E_C[\rho]$ account for the correlation of electrons with parallel and antiparallel spin, respectively. A more detailed discussion on density functionals used for studying TADF emitters is given in Section 2.3.1.

B.0.2 Time-Dependent density functional theory

To address excited states a time-dependent version of the Hohenberg-Kohn theorems, the Runge-Gross theorem, has been formulated, paving the way to the TD-DFT calculations [166]. Its derivation is beyond the scope of this work, we just mention that it has a similar meaning as the first Hohenberg-Kohn theorem [119]. Specifically the Runge-Gross theorem states that (a) the time-dependent wave function is a functional of the electron density and therefore (b) the expectation values of quantum mechanical operators are functionals of the electron density. A time-dependent AS of non-interacting electrons is defined and it is described by a single Slater determinant, $\Phi(\mathbf{r}, t)$. The relevant density is

$$\rho_s(\mathbf{r}, t) = \sum_i^N |\phi_i(\mathbf{r}, t)|^2 \tag{B.12}$$

where $\phi(\mathbf{r}, t)$ are the spin-orbitals, solutions to the time-dependent Kohn-Sham equations

$$i\frac{\partial}{\partial t}\phi_i(\mathbf{r}, t) = \left(-\frac{\nabla^2}{2} + v_{ext}(\mathbf{r}, t) + v_H[\rho](\mathbf{r}, t) + v_{XC}[\rho](\mathbf{r}, t)\right)\phi_i(\mathbf{r}, t) \tag{B.13}$$

where $v_{ext}(\mathbf{r}, t)$ is the external potential, $v_H[\rho](\mathbf{r}, t)$ is the Hartree potential, that includes the electron-nuclei and electron-electron classical interaction and $v_{XC}[\rho](\mathbf{r}, t)$ is the exchange-correlation potential, that has similar meaning to the one in eq. B.10, collecting all exchange and correlation effects; it is expressed as

$$v_{XC}[\rho](\mathbf{r}, t) = \frac{\partial A_{XC}[\rho]}{\partial \rho(\mathbf{r}, t)} \tag{B.14}$$

where $A_{XC}[\rho]$ is the unknown exchange-correlation action functional, often referred to as *xc kernel*. The *adiabatic local density approximation* (ALDA) is based on the assumption that the density varies slowly with time, allowing the use of the same exchange correlation functionals used in time-independent DFT.

When the time-dependent perturbation is treated in the linear response limit, the excitation energies and transition densities are obtained as eigenvalues and eigenvectors of the following non-Hermitian eigenvalue equation (derivation in [119]):

$$\begin{bmatrix} \mathbf{A} & \mathbf{B} \\ \mathbf{B^*} & \mathbf{A^*} \end{bmatrix}\begin{bmatrix} \mathbf{X} \\ \mathbf{Y} \end{bmatrix} = \omega\begin{bmatrix} 1 & 0 \\ 0 & -1 \end{bmatrix}\begin{bmatrix} \mathbf{X} \\ \mathbf{Y} \end{bmatrix} \tag{B.15}$$

The matrix elements of $\mathbf{A}$ and $\mathbf{B}$ are expressed in the Mulliken notation with the indices i, j referring to occupied spin-orbitals,

and a, b referring to virtual orbitals:

$$
\begin{aligned}
A_{ia,bj} &= \delta_{i,j}\delta_{a,b}(\epsilon_a - \epsilon_i) + (ia|jb) + (ia|f_{XC}|jb) \\
B_{ia,jb} &= (ia|bj) + (ia|f_{XC}|bj).
\end{aligned}
\tag{B.16}
$$

The leading term of the **A** matrix is the energy difference of orbitals a and i, the second and first terms of **A** and **B** respectively are the two-electron integrals derived from the linear response of the Coulomb and exchange operators, while the last terms correspond to the linear response of the xc potential to the perturbation. In the case of hybrid functionals such as the ones discussed in Section 2.3.1, the time-dependent Kohn-Sham operators include a component, c_{HF}, of Hartree-Fock exchange in the xc potential and eq B.16 can be written as

$$
\begin{aligned}
A_{ia,bj} =&\, \delta_{i,j}\delta_{a,b}(\epsilon_a - \epsilon_i) + (ia|jb) - c_{HF}(ij|ab) \\
&+ (1 - c_{HF})(ia|f_{XC}|jb) \\
B_{ia,jb} =&\, (ia|bj) - c_{HF}(ib|aj) + (1 - c_{HF})(ia|f_{XC}|bj).
\end{aligned}
\tag{B.17}
$$

The above equation is general and applies to pure TD-DFT when $c_{HF} = 0$ and to time-dependent Hartree-Fock when $c_{HF} = 1$.

In the Tamm-Dancoff approximation (TDA-DFT) the **B** matrix is neglected leading to an Hermitian eigenvalue equation:

$$
\mathbf{AX} = \omega_{TDA}\mathbf{X}
\tag{B.18}
$$

that is the TD-DFT analogous of the Configuration Interaction Singles (CIS) method in Hartree-Fock. Generally, the Tamm-Dancoff approximation works reasonably well in TD-DFT since the neglected terms, **B** and **Y**, are a measure of missing correlation in the ground state, that in DFT is already (partially) included by the exchange-correlation functional. TDA-DFT is widely adopeted for calculations on TADF dyes [108] because it cures triplet instabilities, allowing improved values for transition energy of triplet states [167]. Moreover in the case of CT transitions, the effect of the approximation is negligible, since for charge-separated states the spatial overlap $\phi_i(\mathbf{r})\phi_a(\mathbf{r})$ tends to vanish, making $B_{ia,jb} \simeq 0$ [30]. For all TD-DFT calculations of this work, the Tamm-Dancoff approximation has been imposed.

B.0.3 Long range ω-tuned functional

TD-DFT calculations based on different functionals lead to wildly different results for the excitation spectrum of TADF dyes, particularly with reference to the ΔE_{ST} value and, more generally, in terms of relative order of CT and local excited (LE) states.[168] Range-separated exchange functionals were suggested to solve

the issue. In this approach, the range-separated parameter (ω) is optimally tuned to to get the exact exchange (eX) according to the interelectron distance, r_{12}:[168]

$$\frac{1}{r_{12}} = \frac{1 - [\alpha + \beta\,\mathrm{erf}(\omega \cdot r_{12})]}{r_{12}} + \frac{\alpha + \beta\,\mathrm{erf}(\omega \cdot r_{12})}{r_{12}} = SR + LR$$

(B.19)

where $\mathrm{erf}(x) = \frac{2}{\sqrt{x}} \int_0^x \exp\left(-t^2\right) dt$ and ω is range-tuning parameter.

The first term is the short-range (SR) component which is evaluated by DFT derived from local-density or generalized-gradient approximations. The second term is the long-range (LR) component which is evaluated by Hatree-Fock (HF). The α parameter quantifies the amount of eX in the SR limit, and $\alpha + \beta$ quantifies the amount of eX in the LR limit. The range-separation parameter ω defines the inverse distance at which exchange terms switch from DFT to HF. For any functional, $0 \le \alpha \le 1$, $0 \le \beta \le 1$ and $0 \le \alpha + \beta \le 1$. We use CAM-B3LYP ($\alpha = 0.19$, $\alpha + \beta = 0.65$), M06-2X (56% eX), B3LYP (20% eX) and LC-ωPBE ($\alpha = 0$, $\alpha + \beta = 1$) for comparison.[168, 169] By deafult LC-ωPBE has a ω value of 0.4 Bohr^{-1}.[170, 171] Now we tune this parameter to get the optimal ω (ω^*) using LC-ωPBE functional.

Baer *et al.* proposed a nonempirical method to get optimal ω by enforcing Koopman's theorem,[172] stating that the negative HOMO energy, $-\epsilon_H(N)$, of the N-electron system should be equal to the molecular vertical ionization potential, $IP(N)$.

$$-\epsilon_H^\omega(N) = IP^\omega(N) \qquad (B.20)$$

Since, TADF molecules are donor-acceptor systems, it is useful to focus on ionization potential (related to donor component) as well as on electron affinity (related to acceptor component). The vertical electron affinity of N-electron system, $EA(N)$ should be equal to the negative energy of HOMO energy of anion system, $-\epsilon_H(N + 1)$.

$$-\epsilon_H^\omega(N + 1) = EA^\omega(N) \qquad (B.21)$$

In optimal range-separated method, the goal is to minimize $J(\omega)$ defined as:

$$J(\omega) = |\epsilon_H^\omega(N) + IP^\omega(N)| + |\epsilon_H^\omega(N + 1) + EA^\omega(N)| \qquad (B.22)$$

We have performed our study using LC-ωPBE and found 19.5% as optimal ω for the ground state equlibrium structure. We find the optimal ω gives qualitatively similar result with M06-2X compared to CAM-B3LYP and B3LYP for relative position among LE and CT states.

Dihedral angle	ω
90°	0.195
75°	0.195
60°	0.190
45°	0.185

Table B.1: Optimal ω values estimated for different geometries
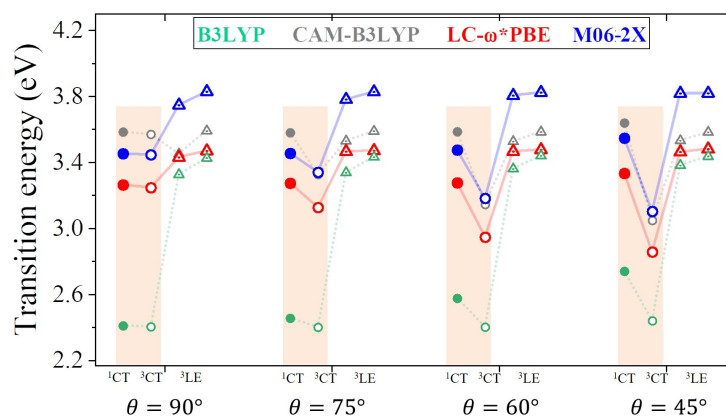
Figure B.1: Excitation energies of the four lowest excited states calculated with different functionals and for different θ values.

Optimal ω is geometry dependent.[173] The dihedral angle of ground state equilibrium structure is 90°. We calculated the optimal ω for dihedral angles of 75°, 60°, 45° and compare with other functionals. Optimal ω values are listed in Table B.1 and plots for transition energy calculated for different dihedral angles and functionals are shown in Fig. B.1.

Computational analysis of TADF dyes (A1, A2, B1, B2, C1, C2)

C

In this appendix, computational details for the systems described in Section 1.5 (Figure 1.7) are presented.

Molecular Orbitals Analysis
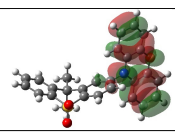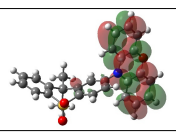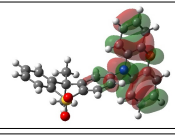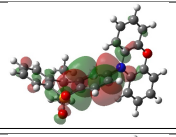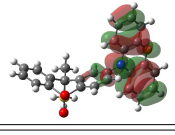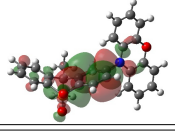
State	HONTO		LUNTO	HONTO-1	LUNTO+1
^3LE_D 3.389 eV		$\xrightarrow{0.931}$			
^3CT 3.487 eV		$\xrightarrow{0.996}$			
^1CT 3.504 eV		$\xrightarrow{0.998}$			

Figure C.1: NTOs of **A1** molecule.
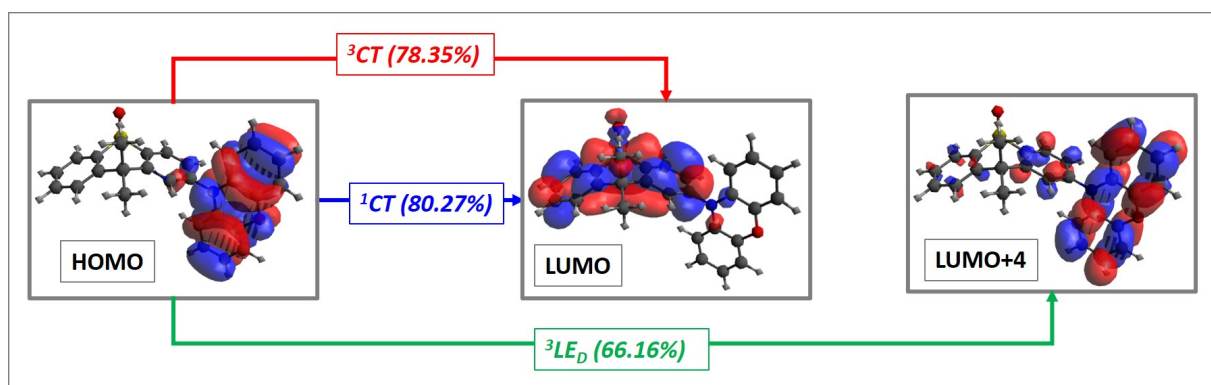
Figure C.2: Molecular Orbitals of **A1**

State	HONTO		LUNTO	HONTO-1		LUNTO+1
$^3\mathrm{LE_D}$ 3.389 eV		0.506 $\longrightarrow$			0.428 $\longrightarrow$	
$^3\mathrm{LE_D}$ 3.390 eV		0.494 $\longrightarrow$			0.439 $\longrightarrow$	
$^3\mathrm{CT}$ 3.416 eV		0.702 $\longrightarrow$			0.281 $\longrightarrow$	
$^3\mathrm{CT}$ 3.421 eV		0.707 $\longrightarrow$			0.280 $\longrightarrow$	
$^1\mathrm{CT}$ 3.428 eV		0.745 $\longrightarrow$			0.253 $\longrightarrow$	
$^1\mathrm{CT}$ 3.436 eV		0.738 $\longrightarrow$			0.261 $\longrightarrow$	

Figure C.3: NTOs of **A2** molecule (DPO-TXO2).

103
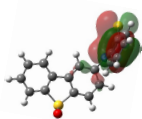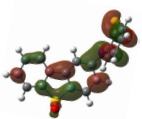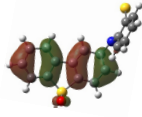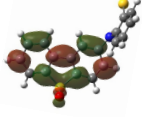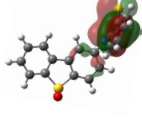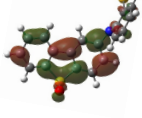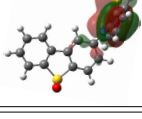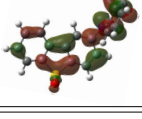
State	HONTO	LUNTO	HONTO-1	LUNTO+1
^{3}CT 3.493 eV		0.942		
^{3}LE$_A$ 3.604 eV		0.911		
^{1}CT 3.607 eV		0.994		
^{3}LE$_D$ 3.753 eV		0.913		

Figure C.4: NTOs of **B1** molecule.
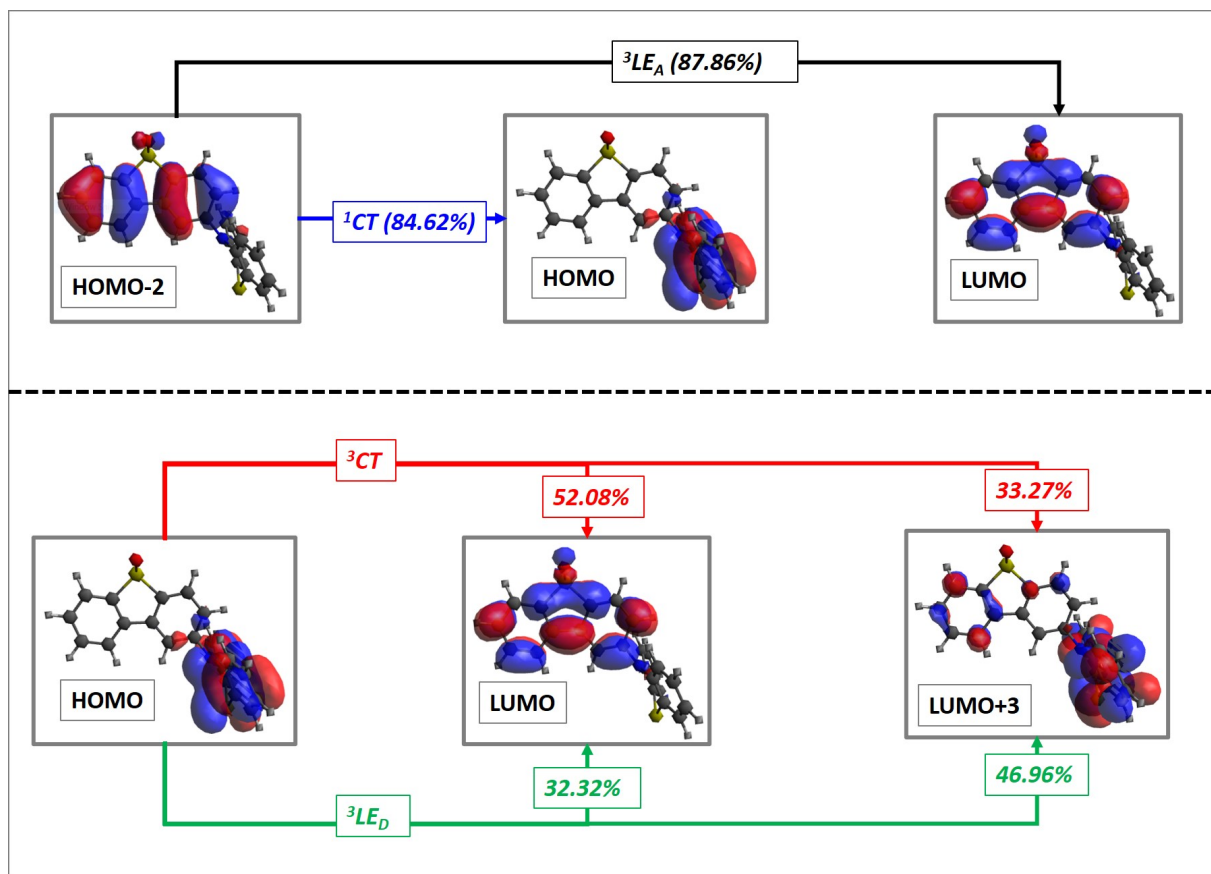
Figure C.5: Molecular Orbitals of **B1**

State	HONTO	LUNTO	HONTO-1	LUNTO+1
^{3}CT 3.407 eV		$\xrightarrow{0.810}$		$\xrightarrow{0.157}$
^{3}CT 3.415 eV		$\xrightarrow{0.802}$		$\xrightarrow{0.165}$
^{1}CT 3.473 eV		$\xrightarrow{0.913}$		
^{1}CT 3.484 eV		$\xrightarrow{0.910}$		
^{3}LE$_A$ 3.580 eV		$\xrightarrow{0.909}$		
^{3}LE$_D$ 3.702 eV		$\xrightarrow{0.554}$		$\xrightarrow{0.345}$
^{3}LE$_D$ 3.705 eV		$\xrightarrow{0.559}$		$\xrightarrow{0.342}$

Figure C.6: NTOs of **B2** molecule.
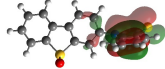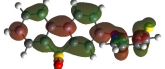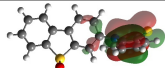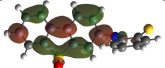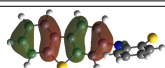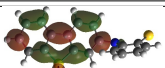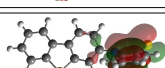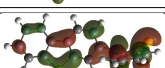
State	HONTO	LUNTO	HONTO-1	LUNTO+1
^{3}CT 3.514 eV		$\xrightarrow{0.961}$		
^{1}CT 3.559 eV		$\xrightarrow{0.996}$		
^{3}LE$_A$ 3.582 eV		$\xrightarrow{0.914}$		
^{3}LE$_D$ 3.662 eV		$\xrightarrow{0.913}$		

Figure C.7: NTOs of **C1** molecule.
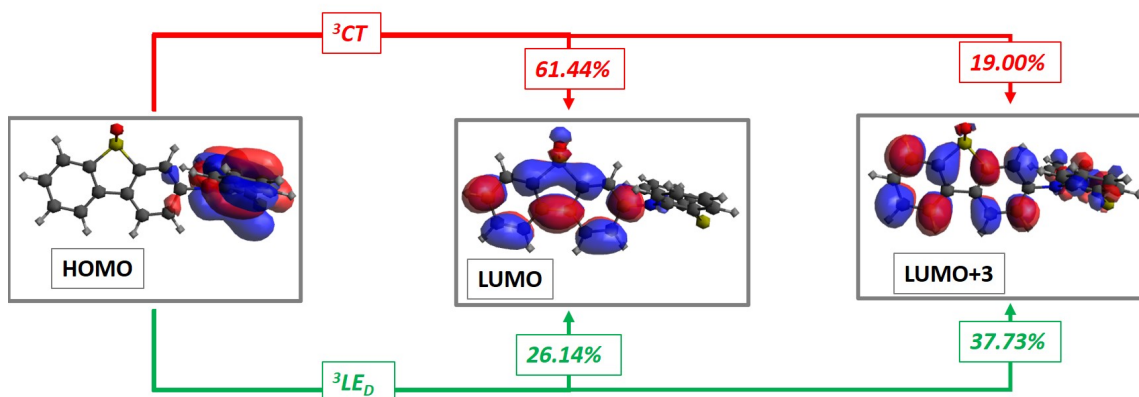
Figure C.8: Molecular Orbitals of **C1**
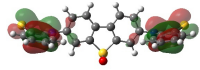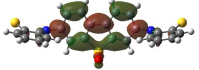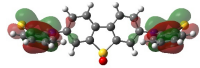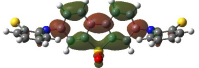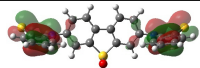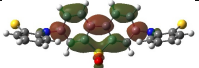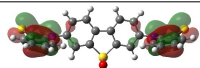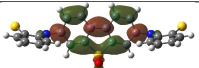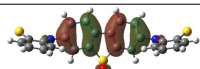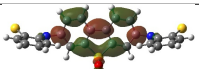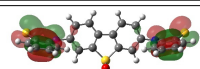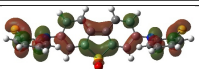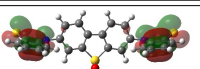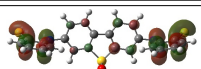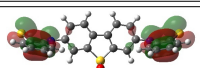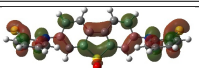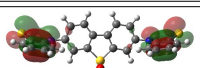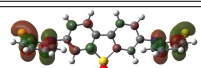
State	HONTO		LUNTO	HONTO-1		LUNTO+1
^{3}CT 3.420 eV		$\xrightarrow{0.888}$				
^{3}CT 3.438 eV		$\xrightarrow{0.877}$				
^{1}CT 3.445 eV		$\xrightarrow{0.934}$				
^{1}CT 3.465 eV		$\xrightarrow{0.932}$				
^{3}LE$_A$ 3.549 eV		$\xrightarrow{0.914}$				
^{3}LE$_D$ 3.636 eV		$\xrightarrow{0.535}$			$\xrightarrow{0.374}$	
^{3}LE$_D$ 3.640 eV		$\xrightarrow{0.538}$			$\xrightarrow{0.372}$	

Figure C.9: NTOs of **C2** molecule.

Additional TD-DFT results

Selected TD-DFT results for the considered dyes (gas-phase result, M06-2X/6-31G(d)). TD-DFT analysis are obtained using GAUSSIAN16 B.01.[14] Transition dipole moment (TDM) and permanent dipole moments (PDM) of excited states are obtained using MULTIWFN software.[174]

Table C.1: TD-DFT outputs for **A1** and **A2**. Molecules are shown with axis alongside (hydrogens are hided for simplicity).
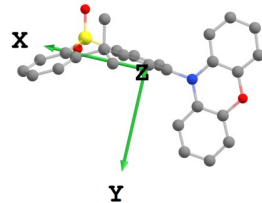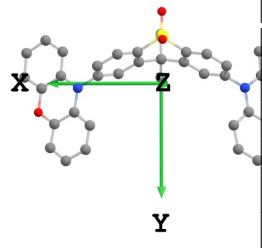
A1	Excitation Energy (eV)	PDM (Debye) (x y z)	TDM (Debye) (x y z)
S_0	–	(0.037, 2.413, 4.056)	–
^1CT	3.389	(-17.686, 4.430, 7.033)	(-0.559, 0.041, 0.069)
^3CT	3.487	(-17.214, 4.325, 6.945)	
^3LE_D	3.389	(0.147, 2.402, 4.080)	

A2	Excitation Energy (eV)	PDM (Debye) (x, y, z)	TDM (Debye) (x, y, z)
S_0	–	(0.000, 2.179, -2.226)	–
^1CT	3.428	(0.085, 10.628, -8.565)	(-0.731, 0.000, 0.001)
	3.436	(-0.085, 10.638, -8.555)	(0.003, -0.313, 0.250)
^3CT	3.416	(0.038, 9.261, -7.625)	
	3.421	(-0.022, 9.612, -7.862)	
^3LE_D	3.389	(0.039, 3.319, -3.061)	
	3.390	(-0.054, 2.961, -2.801)	

Table C.2: TD-DFT outputs for **B1** and **B2**. Molecules are shown with axis alongside (hydrogens are hided for simplicity).

B1	Excitation Energy (eV)	PDM (Debye) (x y z)	TDM (Debye) (x y z)
S_0	–	(-2.501, 0.000, 2.647)	
^1CT	3.607	(1.570, 0.000, 22.306)	(0.000, -0.048, 0.000)
^3CT	3.493	(-1.028, 0.000, 12.950)	
^3LE_A	3.604	(-3.039, 0.000, 2.615)	
^3LE_D	3.753	(-0.734, 0.000, 12.745)	

B2	Excitation Energy (eV)	PDM (Debye) (x y z)	TDM (Debye) (x y z)
S_0	–	(1.673, 0.029, 0.000)	–
^1CT	3.473	(16.503, 1.970, 0.000)	(0.000, 0.000, 0.065)
	3.484	(16.570, -1.980, 0.000)	(0.000, 0.000, 0.001)
^3CT	3.407	(13.131, 1.465, 0.000)	
	3.415	(12.978, -1.420, 0.000)	
^3LE_A	3.580	(1.921, 0.013, 0.000)	
^3LE_D	3.702	(6.017, 0.433, 0.000)	
	3.705	(6.250, -0.433, 0.000)	

Table C.3: TD-DFT outputs for **C1** and **C2**. Molecules are shown with axis alongside (hydrogens are hided for simplicity).

C1	Excitation Energy (eV)	PDM (Debye) (x y z)	TDM (Debye) (x y z)
S_0	–	(2.157, -0.002, 4.834)	
^1CT	3.559	(-20.043, -0.001, 2.547)	(-0.002, -0.106, 0.000)
^3CT	3.514	(-13.705, -0.002, 3.461)	
^3LE_A	3.582	(2.283, -0.001, 4.985)	
^3LE_D	3.662	(-6.139, -0.002, 4.937)	

C2	Excitation Energy (eV)	PDM (Debye) (x y z)	TDM (Debye) (x y z)
S_0	–	(0.000, -0.001, -3.832)	–
^1CT	3.445	(-0.134, -0.001, -2.144)	(0.003, 0.000, 0.000)
	3.465	(0.134, -0.001, -2.192)	(0.000, 0.146, -0.001)
^3CT	3.420	(-0.140, -0.002, -2.373)	
	3.438	(0.141, -0.001, -2.468)	
^3LE_A	3.549	(0.001, 0.000, -3.883)	
^3LE_D	3.636	(-0.163, -0.002, -4.659)	
	3.640	(0.162, -0.002, -4.623)	

Spectroscopic characterization of DMAC-TRZ | D

D.1 Optical spectroscopy

Technical details [1] DMAC, TRZ and DMAC-TRZ were acquired from Merck, and used without further purification. Spectroscopic data were collected in solution using HPLC-grade solvents from Merck. Absorption spectra were recorded with a Perkin Elmer Lambda 650 spectrophotometer. Steady-state and time-resolved luminescence spectra (including anisotropy) were recorded on dilute solutions (absorbance lower than 0.1) with a FLS1000 Edinburgh Fluorometer equipped with a gated PMT detector. Low-temperature measurements were collected on glassy matrices of 2MeTHF at 77 K (the solvent was stored over molecular sieves for one night, and filtered before use), that were fastly cooled using an Oxford Instrument OptistatDN cryostat.

Room temperature absorption and fluorescence spectra of DMAC-TRZ, and of the two subunits, DMAC and TRZ (Figure D.3), dissolved in solvents of different polarity (cyclohexane, toluene, chloroform and DMSO) are shown in the central panels of Figure D.3 and relevant data are summarized in Table D.1. TRZ is not emissive at room temperature. Both DMAC and TRZ are transparent at $\lambda > 350$ nm, so that the weak DMAC-TRZ absorption band (molar extinction coefficient $\sim 2000 \, \text{Lmol}^{-1}\text{cm}^{-1}$, Table D.1) observed at 380 nm is safely assigned to a CT band. Its marginal solvatochromism points to a very small permanent dipole moment for DMAC-TRZ,[7] in line with a largely neutral ground state (i. e a ground state where the contribution from the charge-separated zwitterionic DMAC$^+$-TRZ$^-$ structure is negligible). On the opposite, DMAC-TRZ emission shows a large red-shift upon increasing the solvent polarity: the emission is therefore ascribed to a CT state, a state with a largely zwitterionic character and hence a large permanent dipole moment. The emission is safely ascribed to fluorescence, in view of its lifetime ~ 10 ns (Table D.1 and Figure D.2). Indeed an emission component with longer lifetime is observed, with a sizable weight in chloroform, suggesting a possible delayed fluorescence contribution, as also supported by time resolved emission spectra (Figure D.1) whose shape and position are time-independent.

The different emission bandshapes observed in polar and non-polar solvents are sometimes ascribed to an emissive state whose nature changes from LE to CT. This is easily ruled out by fluorescence excitation spectra (Figure D.5): it is clear that, in all solvents,
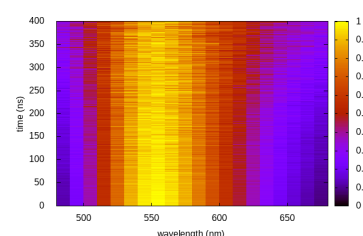
Figure D.1: Time resolved emission spectra of DMAC-TRZ in chloroform.
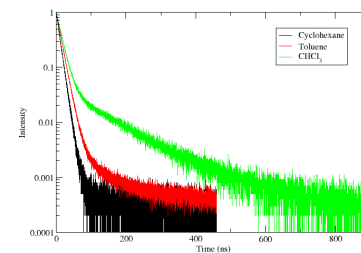
Figure D.2: Fluorescence intensity (excitation 375 nm, detection at the maximum of emission for each solvent) vs time for DMAC-TRZ in different solvents.

emission comes from the same CT state responsible for absorption. Indeed, the broadening of the emission band with increasing solvent polarity is due to the inhomogeneous broadening related to polar solvation.[39, 132, 175]
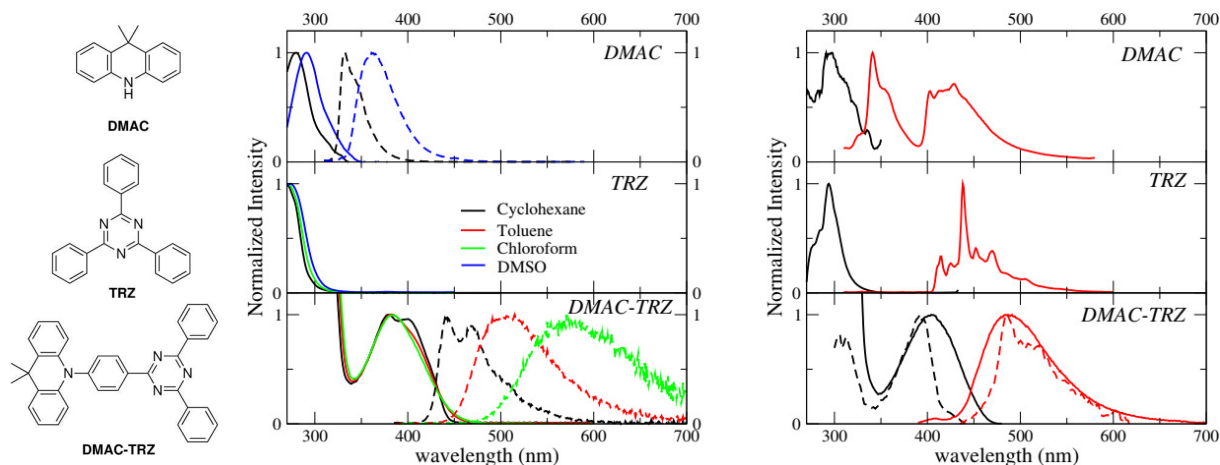
Figure D.3: Left: molecular structures of 9,9-dimethyl-9,10-dihydroacridine (DMAC), 2,4,6-triphenyl-1,3,5-triazine (TRZ) and DMAC-TRZ. Central panels: absorption (continuous lines) and emission spectra (dashed lines) of DMAC, TRZ and DMAC-TRZ in solvents of different polarity. Toluene, with a cut-off wavelength of 285 nm, is not suitable for DMAC and TRZ. Moreover, DMAC is not stable in chloroform, while the emission of DMAC-TRZ in DMSO is very weak. Right panels: excitation (black) and emission (red) spectra of DMAC-TRZ in 2MeTHF at 77 K. Dashed lines in the bottom panel report gated measurements, collected with a gate delay of 1 s and a gate width of 7 s.

To address long-lived emission, including delayed fluorescence and phosphorescence, spectra were collected in a glassy 2MeTHF matrix at 77 K, as shown in Figure D.3 (right panels). DMAC shows two separate emission bands: the short wavelength band (lifetime: 5.2 ns (38%) and 15.4 ns (62%) is due to fluorescence, while the long-wavelength band (lifetime 4 s) is ascribed to phosphorescence. A single long-lived emission (lifetime 1 s) is observed for TRZ, in the blue-green spectral region, again ascribed to phosphorescence. The emission observed for DMAC-TRZ at 485 nm, in a spectral region where neither DMAC nor TRZ emit, is clearly CT in nature. The emission decay (Figure D.4b) shows a short (of the order of ns) and a long (of the order of s) lifetime component in the same spectral region. Time resolved emission spectra are reported in Figure D.6. After a marginal red shift in the first few tenths of ns, the emission profile is constant in time over several order of magnitudes, as expected for TADF. Then, at ~0.1 s the emission bandshape narrows appreciably. Dashed lines in the bottom right panel of Figure D.3 show emission and excitation spectra obtained collecting photons reaching the detector 1 s after the excitation (gated measurements, collected with a gate delay of 1 s and a gate width of 7 s). These long-delayed emission spectra are again superimposed to steady-state emission, even if with narrower bandshape, suggesting either a delayed fluorescence (even if with an unusually long lifetime) or a phosphorescence occurring in the same spectral region as fluorescence. Irrespective of the nature of

Table D.1: Spectroscopic data of DMAC, TRZ and DMAC-TRZ
[a] maximum absorption wavelength, [b] maximum emission wavelength

Compound	Solvent	λ_{abs}[nm][a]	λ_{em}[nm][b]	Quantum Yield	Lifetime [ns]
DMAC	Cyclohexane	280	332	-	2.1 (10.1%) 3.9 (89.9%)
	DMSO	291	361	-	3.6 (4.6%) 7.8 (95.4%)
TRZ	Cyclohexane	269	-	-	-
	Chloroform	271	-	-	-
	DMSO	274	-	-	-
DMAC-TRZ	Cyclohexane	380	442	0.22	9.8 (99.6%) 84.5 (0.4%)
	Toluene	382	510	0.18	12.7 (97.5%) 62.1 (2.5%)
	Chloroform	382	571	0.23	14.4 (75%) 120.1 (25%)

this long-lived emission, the relevant excitation spectrum peaks in the same spectral region as the steady state excitation spectrum of DMAC-TRZ, i.e. in a region where neither DMAC nor TRZ show any absorption feature, demonstrating a dominant CT nature for the long-lived emission.

To gain more information on the nature of the long-lived states, Figure D.4a shows time resolved fluorescence anisotropy spectra collected up to 2 s. Anisotropy remains constant at ∼ 0.25 up to at least 10 ms, and then decreases. The constant and large value of the emission anisotropy over 6 orders of magnitude in time (from ns to ms), and the invariance of emission spectra in the same temporal windows (Figure D.6) unambiguously point to the observation of delayed fluorescence up to ∼ 10 ms. At longer times, the anisotropy decreases (Figure D.4a bottom panel), and the shape of emission spectra (but not their position) changes (Figure D.6, and Figure D.3), offering a clear evidence of the involvement of a different emissive state, corresponding to a very long-lived triplet state. As discussed above, this triplet state has a CT nature, since the corresponding excitation spectrum (black dashed line in Figure D.3) is distinctively red-shifted with respect to the absorption spectra of either DMAC or TRZ subunits. The marked decrease of the anisotropy for the phosphorescence signal can be understood in terms of a small mixing of the CT triplet state with an LE triplet. Transition dipole moments associated with (weak) CT transitions are orders of magnitude smaller than those relevant to LE states: even a weak LE contribution to the phosphorescent state would dominate the observed transition dipole moment, being therefore responsible for its rotation with respect to the CT direction.
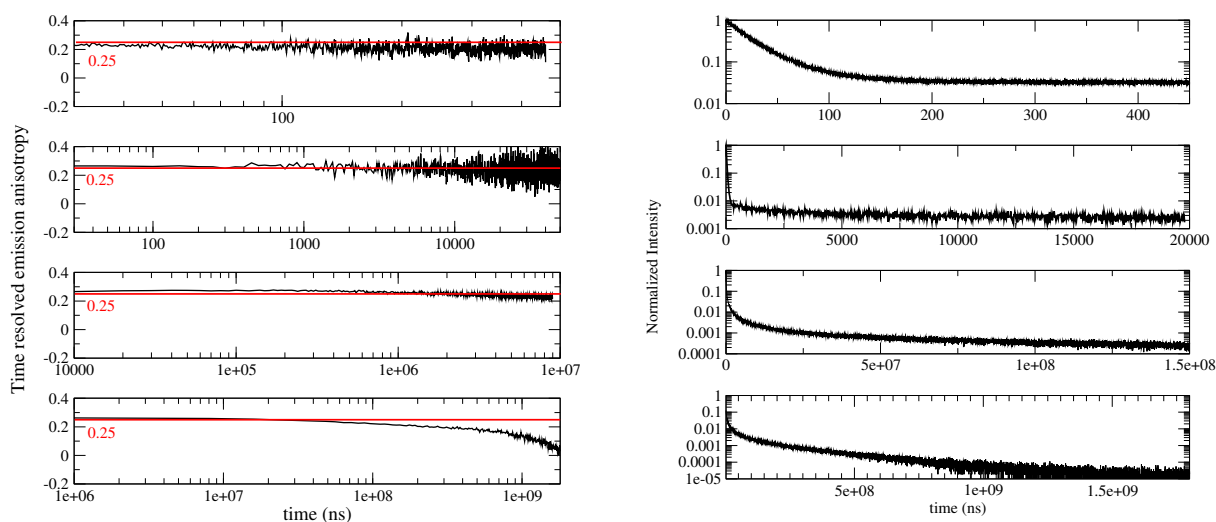
(a) Time-resolved anisotropy of DMAC-TRZ collected in 2MeTHF at 77 K in different time ranges (excitation wavelength 405 nm, emission wavelength 485 nm).

(b) Fluorescence intensity (excitation: 405 nm, emission 485 nm) collected for DMAC-TRZ in 2MeTHF at 77 K on different time ranges.

Figure D.4: Time-resolved fluoroescence decay and anisotropy of DMAC-TRZ in 2MeTHF at 77 K.
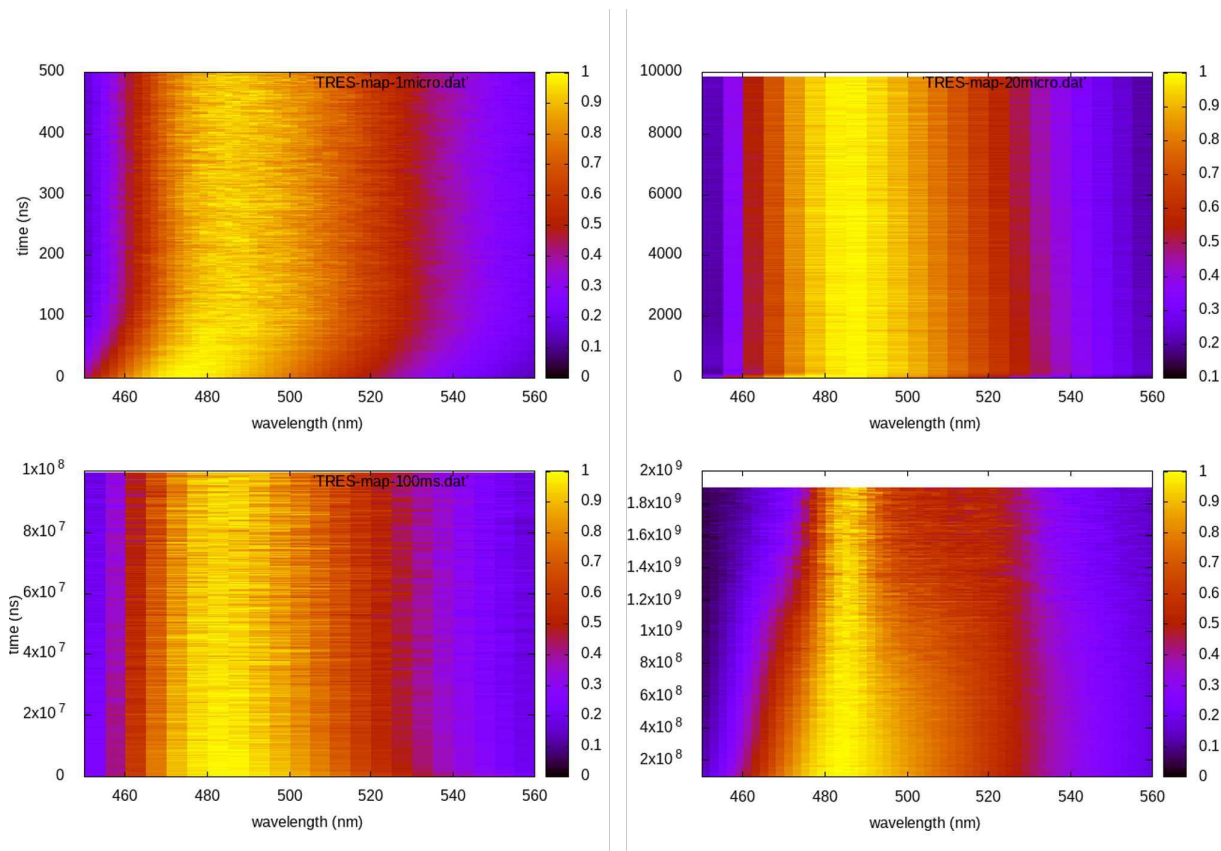
Figure D.6: Time resolved emission spectra of DMAC-TRZ in 2-Me-THF at 77K in different time ranges.

D.2 Spectroscopy in degassed environments

Technical details Degassed solutions of DMAC-TRZ for photophysical characterisation were prepared at 0.8 mM concentration in methylcyclohexane (MCH), toluene (PhMe), and chloroform (CHCl3). Degassed solutions were obtained by 5 freeze-pump-thaw cycles to remove all dissolved oxygen. Steady state emission spectra in Figure D.7 were acquired using a Horiba Jobin Yvon Fluorolog-3 spectrofluorometer. Time-resolved photoluminescence spectra in Figure D.8 and the luminescence decay profiles in Figure D.9 were recorded using an ultra-fast 4 PICOS iCCD camera (Stanford Computer Optics) with a pulsed (10 Hz) Nd:YAG laser (EKSPLA-SL312) excitation source at 355 nm.[2]

As discussed in the previous section (D.1), optical spectroscopy in solution and frozen solvent is valuable to characterize the low-energy electronic states involved in the TADF process in terms of their relative energy and nature. In particular, liquid solvent measurements performed at ambient conditions allow the characterization of the singlet manifold, while measurements in frozen solvent, performed at 77 K are exploited to acquire information on the lowest triplet excited state, by means of its phosphorescence. Indeed, phosphorescence in DMAC-TRZ can only be observed in low temperature regime, where radiationless decay pathways and RISC are hindered.

Regardless, the direct determination of the TADF efficiency requires degassed samples to avoid triplet quenching due to the presence of dissolved oxygen.

As shown in Figure D.7, steady-state photoluminescence in degassed liquid solvents (methylcyclohexane, toluene and chloroform) shows strong positive solvatochromism, with spectra that are superimposable to the fluorescence spectra measured in non-degassed environment (Figure D.3). Time resolved emission spectra (Figure D.8) in liquid solvents are time-invariant and the emission decays (Figure D.9 show the typical behaviour of TADF emitters, characterized by a the prompt fluorescence regime, in the tens of nanoseconds time range, and a delayed fluorescence regime, up to the microseconds. Moreover, the emission decays follow a biexponential behaviour, suggesting high sample homogeneity.

Figure D.10 and D.11, collect spectra collected at room temperature in 1% w/w concentrated degassed films of DMAC-TRZ in ZEONEX, mCBPCN, mCPCN or DPEPO, prepared as in Ref. [148]. Steady-state absorption, emission, excitation spectra (top and middle panels of Figure D.10) show negligible absorption/exictation solvatochromism, and positive emission solvatochromism. The progressive redshift of the emission band with increasing matrix
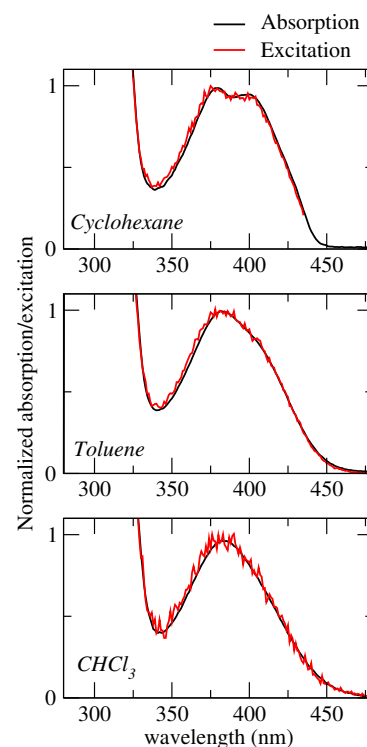
Figure D.5: Absorption and fluorescence excitation spectra of DMAC-TRZ in different solvents.

2: The measurements in this Section have been performed by the group of prof. A. P. Monkman in Durham University.
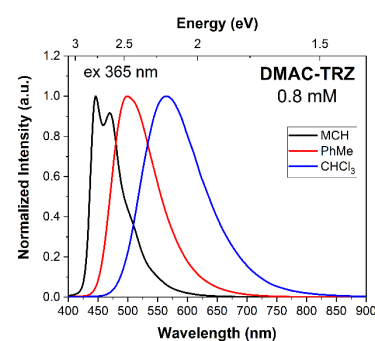
Figure D.7: Photoluminescence spectra of DMAC-TRZ in methylcyclohexane (MCH), toluene (PhMe) and chloroform (CHCl$_3$) at 0.8 mM concentration. All measurements were performed at room temperature, using a 365 nm excitation source.
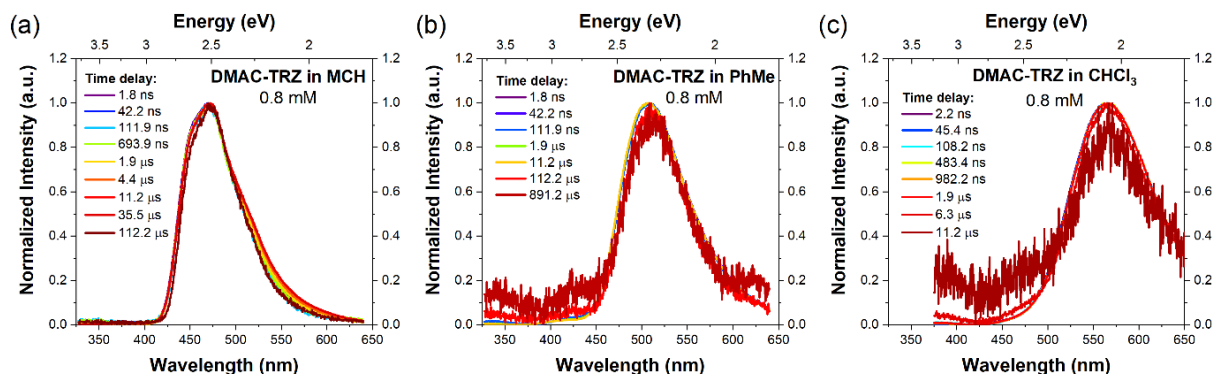
Figure D.8: Time resolved emission spectra of DMAC-TRZ in (a) methylcyclohexane (MCH), (b) toluene (MePh) and (c) chloroform ($CHCl_3$) solutions. All measurements were performed in degassed solutions at room temperature, using a 355 nm excitation source.
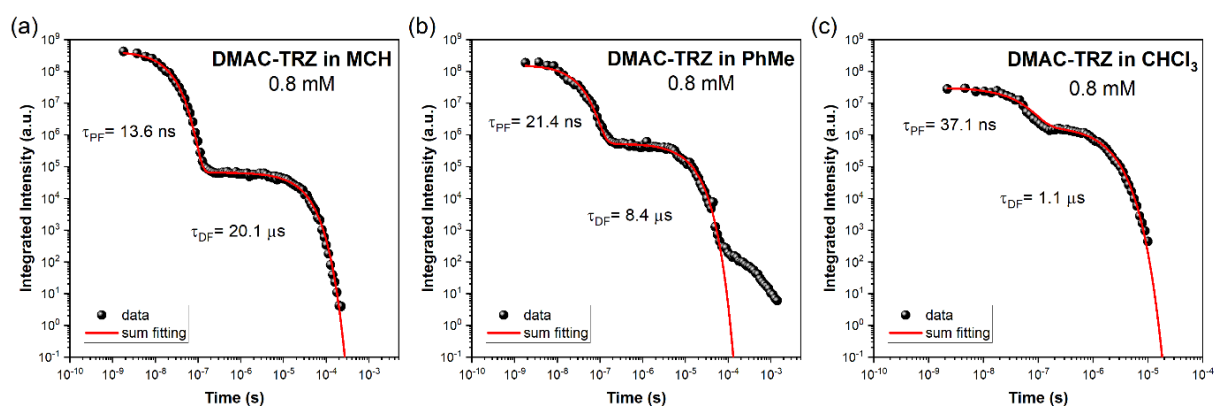

Figure D.9: Kinetic decays of DMAC-TRZ in (a) methylcyclohexane (MCH), (b) toluene (MePh) and (c) chloroform ($CHCl_3$) solutions, at 0.8 mM concentration. All measurements were performed in degassed solutions at room temperature, using a 355 nm excitation source. The data are fitted using a biexponential function.

polarity demonstrates that within the time-window of prompt fluorescence the matrix readjusts at least partially in response to the variation of the dye polarity upon photoexcitation, lowering the excited state energy. Time-resolved spectra and emission intensity (Figure D.11) show clear signs of disorder in condensed phase. Emission decays show a peculiar non-eponential tail at long times (microseconds), while TRES show the same qualitative behaviour in all matrices, a blueshift during prompt fluroescence, and a redshift during delayed fluorescence. The quantitative differences observed in different matrices are due to the interplay between matrix rigidity and polarity, as thoroughly discussed in Section 2.6.
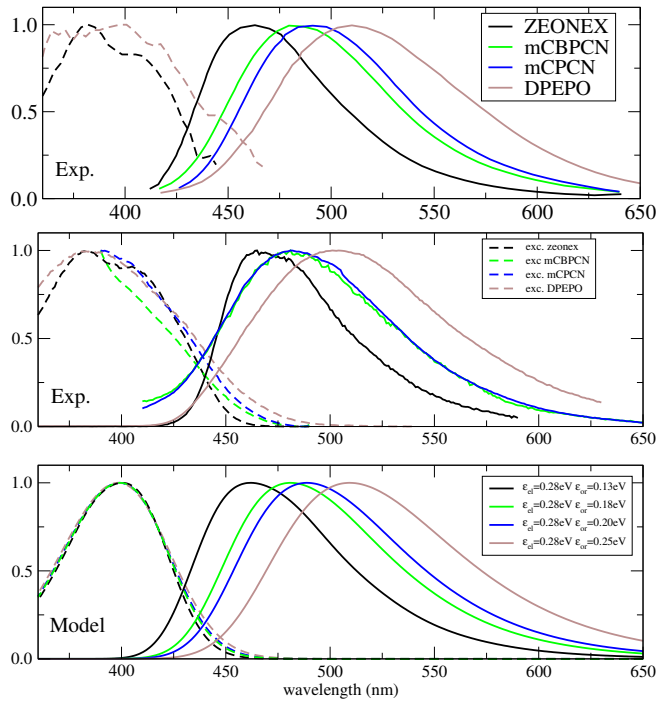
Figure D.10: Top panel: experimental absorption (dashed lines) and emission spectra (continuous lines) of DMAC-TRZ in different matrices from Ref. [148]. Middle panel: experimental excitation (dashed lines) and emission spectra (continuous lines) measured in ambient conditions. Bottom panel: theoretical absorption (dashed) and emission (continuous) spectra computed using the solvent parameters as in legend. The marginal differences between experimental emission spectra collected in degassed (top) and ambient conditions (middle) can be ascribed to a contribution from the host material.
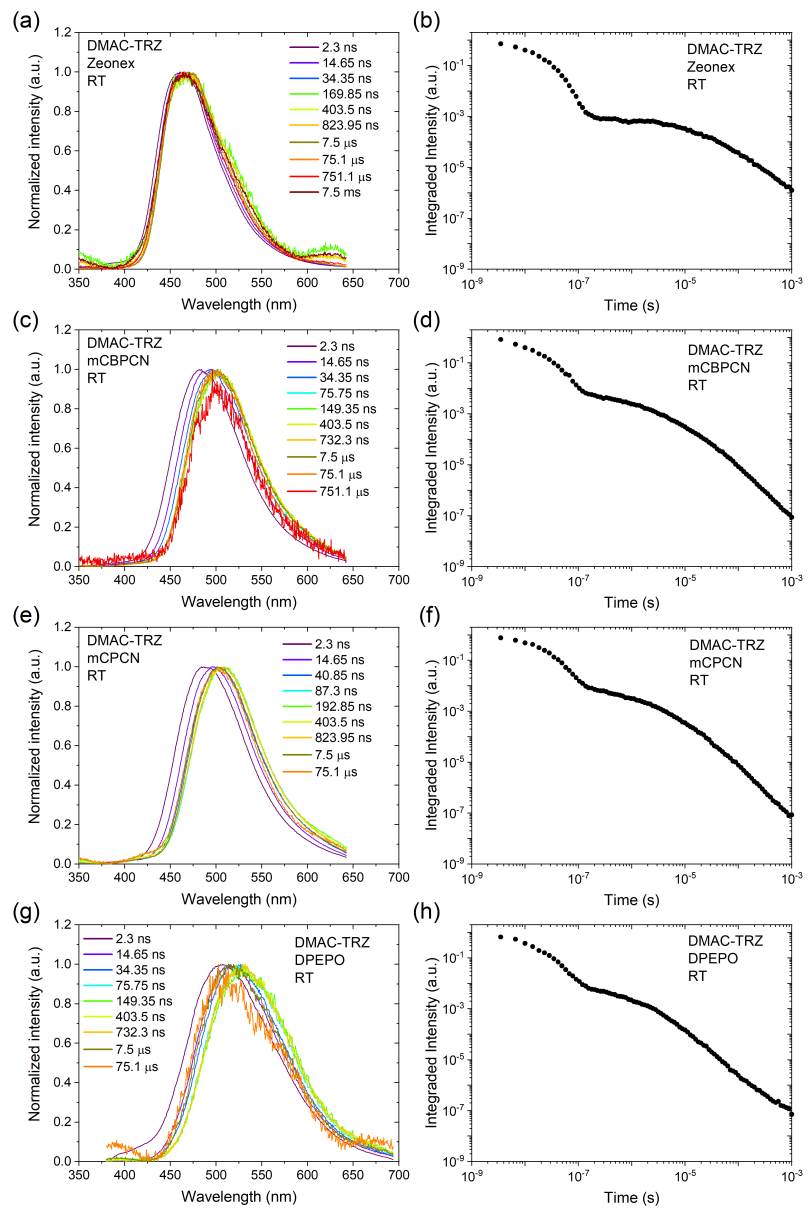
Figure D.11: Room temperature experimental time-resolved emission (left column) and emission decay (right column) of DMAC-TRZ in different matrices at 1% w/w concentration from Ref. [148].

Additional details on the simulation time-resolved spectra of DMAC-TRZ

E

In this appendix, additional details for the simulations of DMAC-TRZ in amorphous matrices discussed in Section 2.6 are collected.

$\hbar\omega_c$ (eV)	Zeonex	mCBPCN	mCPCN	DPEPO
2×10^{-3}	7.9×10^4	2.4×10^5	3.8×10^5	5.9×10^5
4×10^{-3}	9.4×10^4	2.9×10^5	4.4×10^5	6.9×10^5
8×10^{-3}	1.2×10^5	3.4×10^5	4.9×10^5	7.4×10^5

Table E.1: Computed k_{RISC} values (s^{-1}) of DMAC-TRZ in amorphous matrices for different values of $\hbar\omega_c$
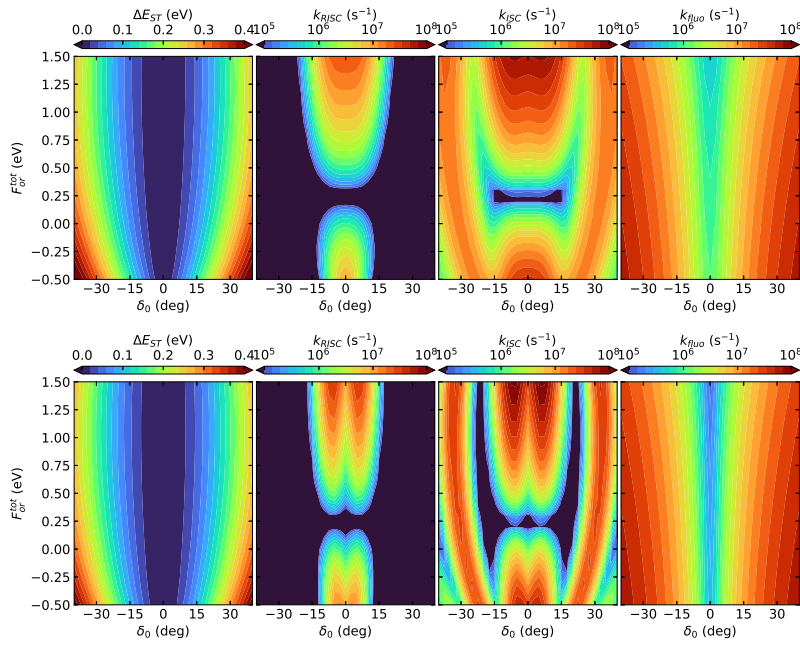
Figure E.1: The color maps show as a function of F_{or} and δ_0 the singlet triplet gap (leftmost panel) and in a logarithmic scale the the calculated rates for $\hbar\omega_c = 2.0 \times 10^{-3}$ eV (top) and $\hbar\omega_c = 8.0 \times 10^{-3}$ eV (bottom). To be compared with results in Fig. 2.22 for $\hbar\omega_c = 4.0 \times 10^{-3}$ eV.
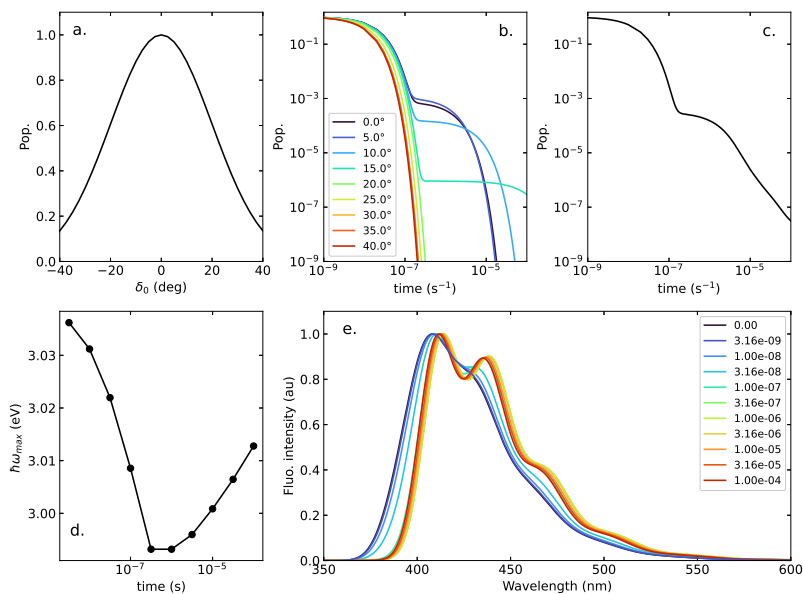
Figure E.2: Same as Fig. 2.24, but using a broader distribution ($\sigma = 20°$) to simulate a higher degree of conformational disorder.
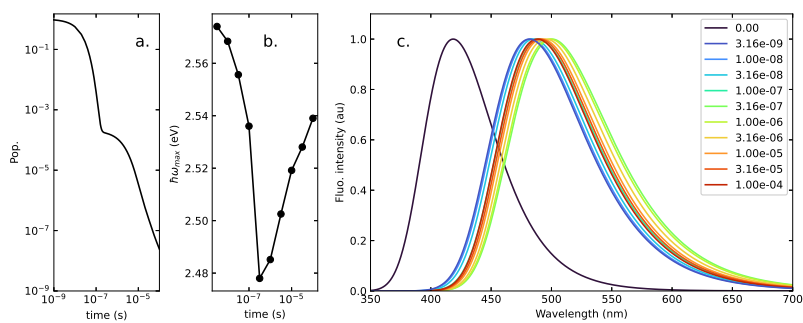
Figure E.3: Simulation of the photophysics of DMAC-TRZ in mCPCN matrix. (a) time-evolution of the singlet population (b) time-evolution of the maximum of the fluorescence spectra (c) time-resolved emission spectra. Time expressed in seconds.
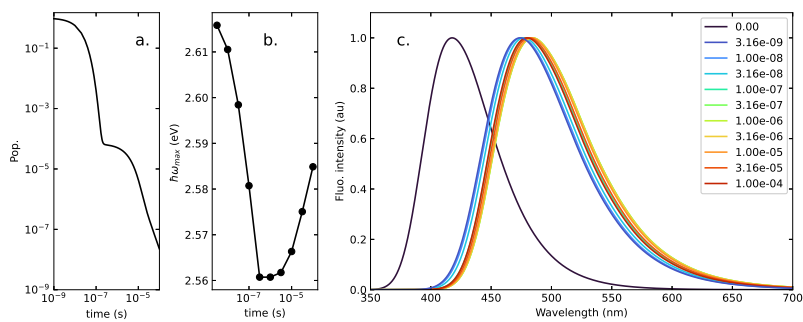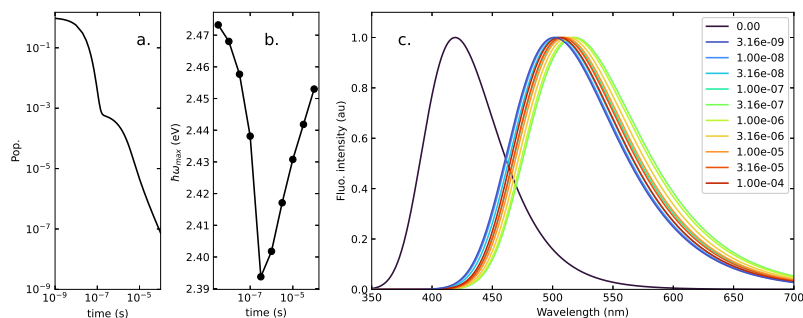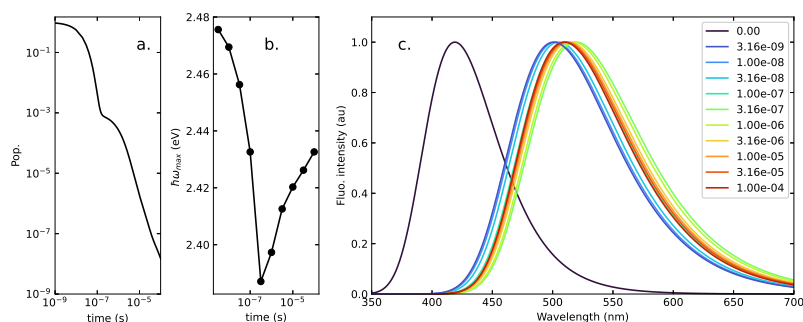

Figure E.4: Simulation of the photophysics of DMAC-TRZ in mCBPCN matrix. (a) time-evolution of the singlet population (b) time-evolution of the maximum of the fluorescence spectra (c) time-resolved emission spectra. Time expressed in seconds.
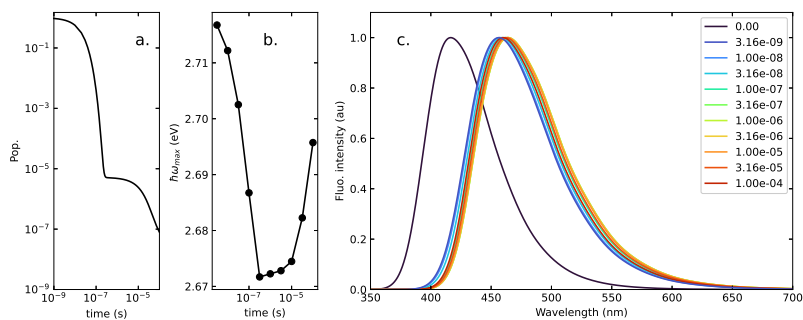
Figure E.5: Simulation of the photophysics of DMAC-TRZ in Zeonex matrix, with $\hbar\omega_c = 2.0 \times 10^{-3}$ eV. (a) time-evolution of the singlet population (b) time-evolution of the maximum of the fluorescence spectra (c) time-resolved emission spectra. Time expressed in seconds.
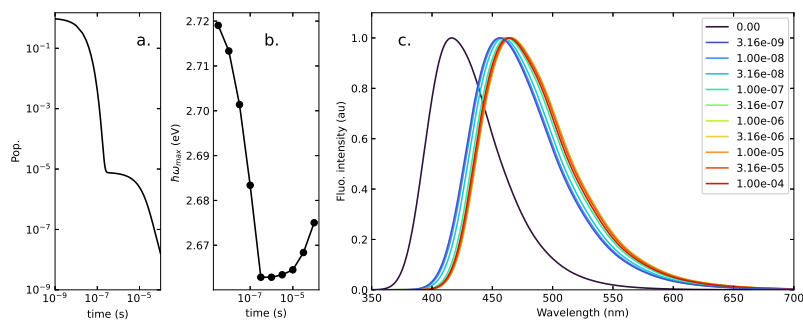
Figure E.6: Simulation of the photophysics of DMAC-TRZ in Zeonex matrix, with $\hbar\omega_c = 8.0\times10^{-3}$ eV. (a) time-evolution of the singlet population (b) time-evolution of the maximum of the fluorescence spectra (c) time-resolved emission spectra. Time expressed in seconds.

Figure E.7: Simulation of the photophysics of DMAC-TRZ in DPEPO matrix, with $\hbar\omega_c = 2.0\times10^{-3}$ eV. (a) time-evolution of the singlet population (b) time-evolution of the maximum of the fluorescence spectra (c) time-resolved emission spectra. Time expressed in seconds.

Figure E.8: Simulation of the photophysics of DMAC-TRZ in DPEPO matrix, with $\hbar\omega_c = 8.0\times10^{-3}$ eV. (a) time-evolution of the singlet population (b) time-evolution of the maximum of the fluorescence spectra (c) time-resolved emission spectra. Time expressed in seconds.
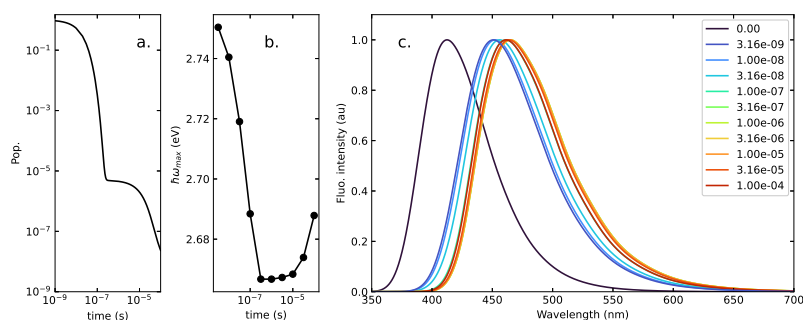
Figure E.9: Same as Fig. 2.27, but using a broader distribution ($\sigma = 20°$) to simulate a higher degree of conformational disorder.
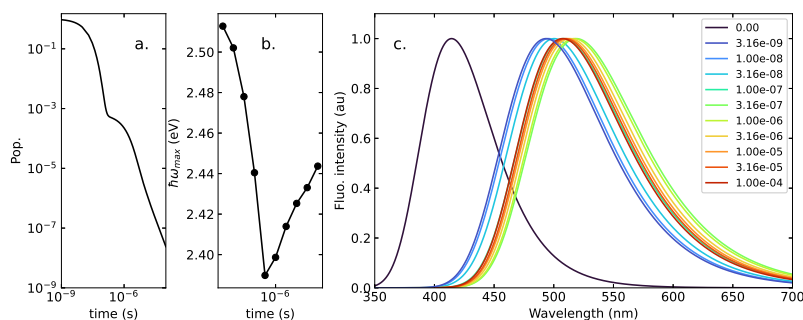
Figure E.10: Same as Fig. 2.29, but using a broader distribution ($\sigma = 20°$) to simulate a higher degree of conformational disorder.

Bibliography

[1] Frank Jensen. *Introduction to Computational Chemistry*. Wiley & Sons, Incorporated, John, 2016, p. 664 (cited on page 5).

[2] Christopher J. Cramer. *Essentials of Computational Chemistry. Theories and Models*. Wiley, 2004, p. 618 (cited on page 5).

[3] Valerio Lucarini et al. *Kramers-Kronig Relations in Optical Materials Research*. Springer London, Limited, 2006 (cited on page 6).

[4] Rodney Loudon. *The quantum theory of light*. Oxford New York: Oxford University Press, 2000 (cited on pages 6, 64, 67, 78).

[5] Lars Onsager. 'Electric Moments of Molecules in Liquids'. In: *Journal of the American Chemical Society* 58.8 (1936), pp. 1486–1493. DOI: `10.1021/ja01299a050` (cited on pages 7, 8).

[6] J.A. Barker and R.O. Watts. 'Monte Carlo studies of the dielectric properties of water-like models'. In: *Molecular Physics* 26.3 (1973), pp. 789–792. DOI: `10.1080/00268977300102101` (cited on page 7).

[7] Christian Reichardt. 'Solvatochromic Dyes as Solvent Polarity Indicators'. In: *Chemical Reviews* 94.8 (1994), pp. 2319–2358. DOI: `10.1021/cr00032a005` (cited on pages 8, 11, 61, 73, 83, 111).

[8] Ernst Lippert. In: *Zeitschrift für Naturforschung A* 10.7 (1955), pp. 541–545. DOI: `doi:10.1515/zna-1955-0707` (cited on page 8).

[9] D. K. Andrea Phan Huu et al. 'Antiadiabatic View of Fast Environmental Effects on Optical Spectra'. In: *Phys. Rev. Lett.* 124 (10 2020), p. 107401. DOI: `10.1103/PhysRevLett.124.107401` (cited on pages 11, 24, 41, 42, 58, 61, 87, 88).

[10] Andrea Amadei et al. 'Theoretical characterization of electronic states in interacting chemical systems'. In: *The Journal of Chemical Physics* 130.8 (2009), p. 084109. DOI: `10.1063/1.3080887` (cited on page 11).

[11] Somananda Sanyal et al. 'Superlinear amplification of the first hyperpolarizability of linear aggregates of DANS molecules'. In: *Phys. Chem. Chem. Phys.* 19 (36 2017), pp. 24979–24984. DOI: `10.1039/C7CP04732K` (cited on pages 11, 26, 54, 57).

[12] Francesca Terenziani et al. 'Charge Instability in Quadrupolar Chromophores: Symmetry Breaking and Solvatochromism'. In: *Journal of the American Chemical Society* 128.49 (2006). PMID: 17147384, pp. 15742–15755. DOI: `10.1021/ja064521j` (cited on pages 11, 26, 27, 30).

[13] Takeshi Yanai, David P Tew, and Nicholas C Handy. 'A new hybrid exchange-correlation functional using the Coulomb-attenuating method (CAM-B3LYP)'. In: *Chemical Physics Letters* 393.1 (2004), pp. 51–57 (cited on page 11).

[14] M. J. Frisch et al. *Gaussian 16 Revision B.01*. Gaussian Inc. Wallingford CT. 2016 (cited on pages 13, 20, 52, 58, 108).

[15] Roberto Cammi and Benedetta Mennucci. 'Linear response theory for the polarizable continuum model'. In: *The Journal of Chemical Physics* 110.20 (1999), pp. 9877–9886 (cited on pages 13, 15, 16, 20).

[16] R. Cammi et al. 'Electronic excitation energies of molecules in solution: State specific and linear response methods for nonequilibrium continuum solvation models'. In: *The Journal of Chemical Physics* 122.10 (2005), p. 104513 (cited on pages 13, 15, 17, 18, 39).

[17] Roberto Improta et al. 'A state-specific polarizable continuum model time dependent density functional theory method for excited state calculations in solution'. In: *The Journal of Chemical Physics* 125.5 (2006), p. 054103. DOI: 10.1063/1.2222364 (cited on pages 13, 15–17, 20, 39).

[18] Marco Caricato et al. 'Formation and relaxation of excited states in solution: A new time dependent polarizable continuum model based on time dependent density functional theory'. In: *The Journal of Chemical Physics* 124.12 (2006), p. 124520 (cited on pages 13, 20).

[19] J. Tomasi, B. Mennucci, and R. Cammi. 'Quantum Mechanical Continuum Solvation Models'. In: *Chem. Rev.* 105 (2005), pp. 2999–3094 (cited on pages 15, 18, 20, 39, 50, 54, 61).

[20] Marco Caricato et al. 'Formation and relaxation of excited states in solution: A new time dependent polarizable continuum model based on time dependent density functional theory'. In: *The Journal of Chemical Physics* 124.12 (2006), p. 124520. DOI: 10.1063/1.2183309 (cited on pages 15–17).

[21] Qisheng Zhang et al. 'Design of Efficient Thermally Activated Delayed Fluorescence Materials for Pure Blue Organic Light Emitting Diodes'. In: *Journal of the American Chemical Society* 134.36 (2012), pp. 14706–14709 (cited on pages 19, 47).

[22] Jiyoung Lee et al. 'Oxadiazole- and triazole-based highly-efficient thermally activated delayed fluorescence emitters for organic light-emitting diodes'. In: *J. Mater. Chem. C* 1 (30 2013), pp. 4599–4604 (cited on page 19).

[23] Paloma L. Santos et al. 'Engineering the singlet-triplet energy splitting in a TADF molecule'. In: *J. Mater. Chem. C* 4 (17 2016), pp. 3815–3824 (cited on pages 19, 20, 48).

[24] Fernando B. Dias et al. 'The Role of Local Triplet Excited States and D-A Relative Orientation in Thermally Activated Delayed Fluorescence: Photophysics and Devices'. In: *Advanced Science* 3.12 (2016), p. 1600080 (cited on pages 19, 20, 47, 48).

[25] Marc K Etherington et al. 'Regio- and conformational isomerization critical to design of efficient thermally-activated delayed fluorescence emitters'. In: *Nature Communications* 8.14987 (2017) (cited on pages 19, 20).

[26] Don M. Mayder et al. 'Design of High-Performance Thermally Activated Delayed Fluorescence Emitters Containing s-Triazine and s-Heptazine with Molecular Orbital Visualization by STM'. In: *Chemistry of Materials* 34.6 (2022), pp. 2624–2635. DOI: 10.1021/acs.chemmater.1c03870 (cited on page 19).

[27] Eduard Spuling et al. '(Deep) blue through-space conjugated TADF emitters based on [2.2]paracyclophanes'. In: *Chem. Commun.* 54 (67 2018), pp. 9278–9281. DOI: 10.1039/C8CC04594A (cited on pages 19, 48).

[28] Andreas Klamt. 'The COSMO and COSMO-RS solvation models'. In: *WIREs Computational Molecular Science* 1.5 (2011), pp. 699–709. DOI: https://doi.org/10.1002/wcms.56 (cited on page 20).

[29] Rama Dhali et al. 'Thermally activated delayed fluorescence: A critical assessment of environmental effects on the singlet–triplet energy gap'. In: *The Journal of Chemical Physics* 154.13 (2021), p. 134112. DOI: 10.1063/5.0042058 (cited on pages 20, 71, 72, 87).

[30] M. Moral et al. 'Theoretical Rationalization of the Singlet-Triplet Gap in OLEDs Materials: Impact of Charge-Transfer Character'. In: *Journal of Chemical Theory and Computation* 11.1 (2015), pp. 168–177 (cited on pages 20, 98).

[31] So Hirata and Martin Head-Gordon. 'Time-dependent density functional theory within the Tamm–Dancoff approximation'. In: *Chemical Physics Letters* 314.3 (1999), pp. 291–299. DOI: https://doi.org/10.1016/S0009-2614(99)01149-5 (cited on pages 20, 52).

[32] Marc K. Etherington et al. 'Revealing the spin–vibronic coupling mechanism of thermally activated delayed fluorescence'. In: *Nature Communications* 7.1 (2016), p. 13680. DOI: 10.1038/ncomms13680 (cited on pages 21, 22, 40).

[33] Marc K. Etherington et al. 'Regio- and conformational isomerization critical to design of efficient thermally-activated delayed fluorescence emitters'. In: *Nat. Commun.* 8 (2017). DOI: 10.1038/ncomms14987 (cited on pages 21, 22, 40, 48).

[34] T. J. Penfold, F. B. Dias, and A. P. Monkman. 'The theory of thermally activated delayed fluorescence for organic light emitting diodes'. In: *Chemical Communications* 54.32 (2018), pp. 3926–3935. DOI: 10.1039/c7cc09612g (cited on pages 21, 40, 48).

[35] Mulliken, R. S. 'Molecular Compounds and their Spectra. II'. In: *J. Am. Chem. Soc.* 74.3 (1952), pp. 811–824 (cited on pages 26, 48).

[36] Rudolph A. Marcus. 'Electron Transfer Reactions in Chemistry: Theory and Experiment (Nobel Lecture)'. In: *Angewandte Chemie International Edition in English* 32.8 (1993), pp. 1111–1121. DOI: https://doi.org/10.1002/anie.199311113 (cited on pages 26, 63, 68).

[37] Anna Painelli. 'Amplification of NLO responses: vibronic and solvent effects in push–pull polyenes'. In: *Chemical Physics* 245.1 (1999), pp. 185–197. DOI: https://doi.org/10.1016/S0301-0104(99)00085-3 (cited on pages 26, 28, 41, 59, 61, 73, 83).

[38] Anna Painelli and Francesca Terenziani. 'Optical Spectra of Push-Pull Chromophores in Solution: A Simple Model'. In: *The Journal of Physical Chemistry A* 104.47 (2000), pp. 11041–11048 (cited on page 26).

[39] B. Boldrini et al. 'Polar Dyes in Solution: A Joint Experimental and Theoretical Study of Absorption and Emission Band Shapes'. In: *J. Phys. Chem. A* 106 (2002), pp. 6286–6294 (cited on pages 26, 49, 54, 57, 61, 73, 83, 112).

[40] Francesca Terenziani, Cristina Sissa, and Anna Painelli. 'Symmetry Breaking in Octupolar Chromophores: Solvatochromism and Electroabsorption'. In: *The Journal of Physical Chemistry B* 112.16 (2008), pp. 5079–5087 (cited on pages 26, 50).

[41] Painelli, A. and Terenziani, F. 'Linear and non-linear optical properties of push-pull chromophores: vibronic and solvation effects beyond perturbation theory'. In: *Synth. Met.* 124.1 (2001), pp. 171–173 (cited on page 26).

[42] D'Avino, G. and Terenziani, F. and Painelli, A. 'Aggregates of Quadrupolar Dyes: Giant Two-Photon Absorption from Biexciton States'. In: *ChemPhysChem* 8 (2007), pp. 2433–2444 (cited on page 26).

[43] S. Sanyal et al. 'Aggregates of quadrupolar dyes for two-photon absorption: the role of intermolecular interactions'. In: *Phys. Chem. Chem. Phys.* 18 (40 2016), pp. 28198–28208. DOI: 10.1039/C6CP05153G (cited on page 26).

[44] Brunella Bardi et al. 'Multistimuli-Responsive Materials from Benzothiadiazole-Based Charge-Transfer Chromophores: Interdependence of Optical Properties and Aggregation'. In: *ChemPhotoChem* 2.12 (2018), pp. 1027–1037. DOI: 10.1002/cptc.201800145 (cited on page 26).

[45] Rama Dhali et al. 'Understanding TADF: a joint experimental and theoretical study of DMAC-TRZ'. In: *Physical Chemistry Chemical Physics* 23.1 (2021), pp. 378–387. DOI: 10.1039/d0cp05982j (cited on pages 26, 40, 48, 73, 76).

[46] Anna Painelli. 'Amplification of NLO responses: vibronic and solvent effects in push-pull polyenes'. In: *Chemical Physics* 245.1 (1999), pp. 185–197 (cited on pages 27, 49).

[47] Francesca Terenziani, Cristina Sissa, and Anna Painelli. 'Symmetry Breaking in Octupolar Chromophores: Solvatochromism and Electroabsorption'. In: *The Journal of Physical Chemistry B* 112.16 (2008). PMID: 18376886, pp. 5079–5087. DOI: `10.1021/jp710241g` (cited on page 27).

[48] Painelli, A. and Terenziani, F. 'A non-perturbative approach to solvatochromic shifts of push-pull chromophores'. In: *Chem. Phys. Lett.* 312.2 (1999), pp. 211–220 (cited on page 28).

[49] Philip W. Anderson. *Basic Notions of Condensed Matter Physics*. Boca Raton, FL: CRC Press, 1996 (cited on page 34).

[50] Cristina Sissa et al. 'Vibrational coherences in charge-transfer dyes: A non-adiabatic picture'. In: *The Journal of Chemical Physics* 141.16 (2014), p. 164317. DOI: `10.1063/1.4898710` (cited on page 34).

[51] Francesca Terenziani et al. 'Essential-State Model for Polymethine Dyes: Symmetry Breaking and Optical Spectra'. In: *The Journal of Physical Chemistry Letters* 1.12 (2010), pp. 1800–1804. DOI: `10.1021/jz100430x` (cited on page 34).

[52] Cristina Sissa et al. 'About the origin of the large Stokes shift in aminoalkyl substituted heptamethine cyanine dyes'. In: *Phys. Chem. Chem. Phys.* 22 (1 2020), pp. 129–135. DOI: `10.1039/C9CP05473A` (cited on page 34).

[53] Cristina Sissa et al. 'Essential State Model for Two-Photon Absorption Spectra of Polymethine Dyes'. In: *ChemPhysChem* 13.11 (2012), pp. 2795–2800. DOI: `10.1002/cphc.201200021` (cited on page 34).

[54] T. Northey, J. Stacey, and T. J. Penfold. 'The role of solid state solvation on the charge transfer state of a thermally activated delayed fluorescence emitter'. In: *Journal of Materials Chemistry C* 5.42 (2017), pp. 11001–11009. DOI: `10.1039/c7tc04099g` (cited on pages 38, 77).

[55] Qian Wang et al. 'QM/MM studies on luminescence mechanism of dinuclear copper iodide complexes with thermally activated delayed fluorescence'. In: *RSC Adv.* 9.36 (2019), pp. 20786–20795. DOI: `10.1039/c9ra02256b` (cited on page 38).

[56] Y. Olivier et al. 'Nature of the singlet and triplet excitations mediating thermally activated delayed fluorescence'. In: *Phys. Rev. Materials* 1 (7 2017), p. 075602. DOI: `10.1103/PhysRevMaterials.1.075602` (cited on pages 38, 40, 69, 77).

[57] Jing Li et al. 'Accurate description of charged excitations in molecular solids from embedded many-body perturbation theory'. In: *Phys. Rev. B* 97 (3 2018), p. 035108 (cited on page 38).

[58] Lingling Lv et al. 'Investigation of Conversion and Decay Processes in Thermally Activated Delayed Fluorescence Copper(I) Molecular Crystal: Theoretical Estimations from an ONIOM Approach Combined with the Tuned Range-Separated Density Functional Theory'. In: *The Journal of Physical Chemistry A* 123.10 (2019), pp. 2080–2090. DOI: `10.1021/acs.jpca.9b00321` (cited on page 38).

[59] Taiping Hu et al. 'Origin of High Efficiencies for Thermally Activated Delayed Fluorescence Organic Light-Emitting Diodes: Atomistic Insight into Molecular Orientation and Torsional Disorder'. In: *J. Phys. Chem. C* 122.48 (2018), pp. 27191–27197. DOI: `10.1021/acs.jpcc.8b08169` (cited on pages 38, 77, 80).

[60] Hao Sun et al. 'Theoretical insights on the luminescent mechanism of an efficient aggregation-induced nondoped delayed fluorescence emitter using QM / MM method'. In: *Int. J. Quantum Chem* (2020). DOI: `10.1002/qua.26490` (cited on page 38).

[61] Jianzhong Fan et al. 'The role of intermolecular interactions in regulating the thermally activated delayed fluorescence and charge transfer properties: a theoretical perspective'. In: *J. Mater. Chem. C* 8.25 (2020), pp. 8601–8612. DOI: 10.1039/d0tc01286f (cited on page 38).

[62] Kai Zhang et al. 'Effect of intermolecular interaction on excited-state properties of thermally activated delayed fluorescence molecules in solid phase: A QM/MM study'. In: *Spectrochim. Acta A* 209 (2019), pp. 248–255. DOI: 10.1016/j.saa.2018.10.053 (cited on page 38).

[63] Yuan-Jun Gao et al. 'QM and ONIOM studies on thermally activated delayed fluorescence of copper(i) complexes in gas phase, solution, and crystal'. In: *Phys. Chem. Chem. Phys.* 20.38 (2018), pp. 24955–24967. DOI: 10.1039/c8cp03657h (cited on page 38).

[64] Chunyun Tu and WanZhen Liang. 'NB-Type Electronic Asymmetric Compounds as Potential Blue-Color TADF Emitters: Steric Hindrance, Substitution Effect, and Electronic Characteristics'. In: *ACS Omega* 2 (2017), pp. 3098–3109. DOI: 10.1021/acsomega.7b00514 (cited on page 38).

[65] Tzu-Ting Huang and Elise Y. Li. 'Enhanced spin-orbit coupling driven by state mixing in organic molecules for OLED applications'. In: *Organic Electronics* 39 (2016), pp. 311–317. DOI: 10.1016/j.orgel.2016.10.026 (cited on pages 38, 40).

[66] Haitao Sun et al. 'Impact of Dielectric Constant on the Singlet–Triplet Gap in Thermally Activated Delayed Fluorescence Materials'. In: *The Journal of Physical Chemistry Letters* 8.11 (2017), pp. 2393–2398. DOI: 10.1021/acs.jpclett.7b00688 (cited on page 38).

[67] Mónica Moral et al. 'Combined Theoretical and Experimental Study on Intramolecular Charge Transfer Processes in Star-Shaped Conjugated Molecules'. In: *J. Phys. Chem. C* 123 (2019), pp. 11179–11188. DOI: 10.1021/acs.jpcc.8b12248 (cited on page 38).

[68] Igor Lyskov et al. 'Exciton energy transfer in organic light emitting diodes with thermally activated delayed fluorescence dopants'. In: *Journal of Materials Chemistry C* 6.25 (2018), pp. 6860–6868. DOI: 10.1039/c8tc01992d (cited on page 38).

[69] T. J. Penfold, F. B. Dias, and A. P. Monkman. 'The theory of thermally activated delayed fluorescence for organic light emitting diodes'. In: *Chem. Commun.* 54 (2018), pp. 3926–3935. DOI: 10.1039/c7cc09612g (cited on page 38).

[70] Ryoichi Ishimatsu et al. 'Solvent Effect on Thermally Activated Delayed Fluorescence by 1,2,3,5-Tetrakis(carbazol-9-yl)-4,6-dicyanobenzene'. In: *J. Phys. Chem. A* 117 (2013), pp. 5607–5612. DOI: 10.1021/jp404120s (cited on page 38).

[71] Hiroki Uoyama et al. 'Highly efficient organic light-emitting diodes from delayed fluorescence'. In: *Nature* 492.7428 (2012), pp. 234–238. DOI: 10.1038/nature11687 (cited on page 38).

[72] Minki Hong et al. 'Effect of Substituents on the Electronic Structure and Degradation Process in Carbazole Derivatives for Blue OLED Host Materials'. In: *Chem. Mater.* 28 (2016), pp. 5791–5798. DOI: 10.1021/acs.chemmater.6b02069 (cited on page 38).

[73] Georgi Valchanov et al. 'Understanding the Fluorescence of TADF Light-Emitting Dyes'. In: *J. Phys. Chem. A* 120 (2016), pp. 6944–6955. DOI: 10.1021/acs.jpca.6b06680 (cited on page 38).

[74] Gintare Grybauskaite-Kaminskiene et al. 'Contribution of TADF and exciplex emission for efficient "warm-white" OLEDs'. In: *J. Mater. Chem. C.* 6 (2018), pp. 1543–1550. DOI: 10.1039/c7tc05392d (cited on page 38).

[75] Tom Cardeynaels et al. 'Benzo[1,2-b:4,5-b']dithiophene as a weak donor component for push-pull materials displaying thermally activated delayed fluorescence or room temperature phosphorescence'. In: *Dyes and Pigments* (2020), p. 109022. DOI: `10.1016/j.dyepig.2020.109022` (cited on page 38).

[76] Chao Wang et al. 'Prediction of Intramolecular Charge-Transfer Excitation for Thermally Activated Delayed Fluorescence Molecules from a Descriptor-Tuned Density Functional'. In: *J. Phys. Chem. C* 122 (2018), pp. 7816–7823. DOI: `10.1021/acs.jpcc.7b10560` (cited on page 38).

[77] Lijuan Wang et al. 'Theoretical tuning of the singlet–triplet energy gap to achieve efficient long-wavelength thermally activated delayed fluorescence emitters: the impact of substituents'. In: *Phys. Chem. Chem. Phys.* 19 (2017), pp. 21639–21647. DOI: `10.1039/c7cp02615c` (cited on page 38).

[78] Ying Gao et al. 'Investigation on the effect of connected bridge on thermally activated delayed fluorescence property for DCBPy emitter'. In: *Dyes and Pigments* 145 (2017), pp. 277–284. DOI: `10.1016/j.dyepig.2017.04.001` (cited on pages 38, 40).

[79] Chuhuan He et al. 'Unraveling the Emission Mechanism of Radical-Based Organic Light-Emitting Diodes'. In: *J. Phys. Chem. Lett.* 10 (2019), pp. 574–580. DOI: `10.1021/acs.jpclett.8b03864` (cited on page 38).

[80] Pralok K. Samanta et al. 'Up-Conversion Intersystem Crossing Rates in Organic Emitters for Thermally Activated Delayed Fluorescence: Impact of the Nature of Singlet vs Triplet Excited States'. In: *Journal of the American Chemical Society* 139.11 (2017), pp. 4042–4051. DOI: `10.1021/jacs.6b12124` (cited on pages 38, 40, 68, 69, 71).

[81] B. Lunkenheimer and Köhn. 'Solvent Effects on Electronically Excited States Using the Conductor- Like Screening Model and the Second-Order Correlated Method ADC(2)'. In: *J. Chem. Theory Comput.* 9 (2013), pp. 977–994 (cited on pages 39, 61).

[82] Ciro A. Guido and Stefano Caprasecca. 'On the description of the environment polarization response to electronic transitions'. In: *International Journal of Quantum Chemistry* 119.1 (2019), e25711. DOI: `10.1002/qua.25711` (cited on page 39).

[83] Aleksandr V. Marenich, Christopher J. Cramer, and Donald G. Truhlar. 'Electronic Absorption Spectra and Solvatochromic Shifts by the Vertical Excitation Model: Solvated Clusters and Molecular Dynamics Sampling'. In: *The Journal of Physical Chemistry B* 119.3 (2014), pp. 958–967. DOI: `10.1021/jp506293w` (cited on page 39).

[84] Hyung J. Kim and James T. Hynes. 'Equilibrium and nonequilibrium solvation and solute electronic structure. III. Quantum theory'. In: *The Journal of Chemical Physics* 96 (1992), pp. 5088–5110 (cited on pages 39, 41).

[85] M. V. Basilevsky, G. E. Chudinov, and M. D. Newton. 'The multi-configurational adiabatic electron transfer theory and its invariance under transformations of charge density basis functions'. In: *Chemical Physics* 179 (1994), pp. 263–278 (cited on pages 39, 41).

[86] Zeyi Tu et al. 'Nature of the Lowest Singlet and Triplet Excited States of Organic Thermally Activated Delayed Fluorescence Emitters: A Self-Consistent Quantum Mechanics/Embedded Charge Study'. In: *Chem. Mater.* 31 (2019), pp. 6665–6671. DOI: `10.1021/acs.chemmater.9b00824` (cited on page 40).

[87] Piotr de Silva. 'Inverted Singlet–Triplet Gaps and Their Relevance to Thermally Activated Delayed Fluorescence'. In: *The Journal of Physical Chemistry Letters* 10.18 (2019), pp. 5674–5679. DOI: `10.1021/acs.jpclett.9b02333` (cited on pages 40, 49).

[88] Johannes Ehrmaier et al. 'Singlet–Triplet Inversion in Heptazine and in Polymeric Carbon Nitrides'. In: *The Journal of Physical Chemistry A* 123.38 (2019), pp. 8099–8108. DOI: `10.1021/acs.jpca.9b06215` (cited on pages 40, 49).

[89] Robert Pollice et al. 'Organic Molecules with Inverted Gaps between First Excited Singlet and Triplet States and Appreciable Fluorescence Rates'. In: (2020). DOI: `10.26434/chemrxiv.13087319.v1` (cited on pages 40, 49).

[90] J. Sanz-Rodrigo et al. 'Negative Singlet–Triplet Excitation Energy Gap in Triangle-Shaped Molecular Emitters for Efficient Triplet Harvesting'. In: *The Journal of Physical Chemistry A* 125.2 (2021), pp. 513–522. DOI: `10.1021/acs.jpca.0c08029` (cited on pages 40, 49).

[91] G. Ricci et al. 'Singlet-Triplet Excited-State Inversion in Heptazine and Related Molecules: Assessment of TD-DFT and ab initio Methods'. In: *ChemPhysChem* (2021). DOI: `10.1002/cphc.202000926` (cited on pages 40, 49).

[92] Monika Stanke. 'Adiabatic, Born-Oppenheimer, and Non-adiabatic Approaches'. In: *Handbook of Computational Chemistry*. Springer Netherlands, 2015, pp. 1–51. DOI: `10.1007/978-94-007-6169-8_41-1` (cited on page 41).

[93] D. Feinberg, S. Ciuchi, and F. De Pasquale. 'Squeezing phenomena in interacting electron-phonon systems'. In: *Int. J. Modern Phys. B* 4 (1990), pp. 1317–1367 (cited on page 41).

[94] Ciro A. Guido et al. 'An open quantum system theory for polarizable continuum models'. In: *The Journal of Chemical Physics* 152.17 (2020), p. 174114. DOI: `10.1063/5.0003523` (cited on page 41).

[95] H. Hayashi et al. 'The complete optical spectrum of liquid water measured by inelastic x-ray scattering'. In: *Proceedings of the National Academy of Sciences* 97.12 (2000), pp. 6264–6266. DOI: `10.1073/pnas.110572097` (cited on page 42).

[96] Joel M. Milanese et al. 'Convergence of Computed Aqueous Absorption Spectra with Explicit Quantum Mechanical Solvent'. In: *Journal of Chemical Theory and Computation* 13.5 (2017), pp. 2159–2171. DOI: `10.1021/acs.jctc.7b00159` (cited on page 42).

[97] Joseph Shinar, ed. *Organic Light-Emitting Devices*. Springer-Verlag New York, 2004 (cited on page 45).

[98] T. M. Brown et al. 'LiF/Al cathodes and the effect of LiF thickness on the device characteristics and built-in potential of polymer light-emitting diodes'. In: *Applied Physics Letters* 77.19 (2000), pp. 3096–3098 (cited on page 45).

[99] F. Cacialli et al. 'Efficient green light-emitting diodes from a phenylated derivative of poly(p-phenylene-vinylene)'. In: *Applied Physics Letters* 69.25 (1996), pp. 3794–3796 (cited on page 45).

[100] G. Gigli et al. 'High-efficiency oligothiopene-based light-emitting diodes'. In: *Applied Physics Letters* 75.4 (1999), pp. 439–441 (cited on page 45).

[101] Franco Cacialli et al. 'Cyclodextrin-threaded conjugated polyrotaxanes as insulated molecular wires with reduced interstrand interactions'. In: *Nature Materials* 1 (2002), p. 160 (cited on page 45).

[102] Chihaya Adachi. 'Third-generation organic electroluminescence materials'. In: *Japanese Journal of Applied Physics* 53.6 (2014), p. 060101 (cited on page 46).

[103] Chihaya Adachi et al. 'Nearly 100% internal phosphorescence efficiency in an organic light-emitting device'. In: *Journal of Applied Physics* 90.10 (2001), pp. 5048–5051 (cited on page 46).

[104] C. A. Parker, C. G. Hatchard, and Edmund John Bowen. 'Delayed fluorescence from solutions of anthracene and phenanthrene'. In: *Proceedings of the Royal Society of London. Series A. Mathematical and Physical Sciences* 269.1339 (1962), pp. 574–584 (cited on page 46).

[105] Denis Y. Kondakov. 'Triplet-triplet annihilation in highly efficient fluorescent organic light-emitting diodes: current state and future outlook'. In: *Philosophical Transactions of the Royal Society A: Mathematical, Physical and Engineering Sciences* 373.2044 (2015), p. 20140321 (cited on page 46).

[106] C. A. Parker and C. G. Hatchard. 'Triplet-singlet emission in fluid solutions. Phosphorescence of eosin'. In: *Trans. Faraday Soc.* 57 (0 1961), pp. 1894–1904 (cited on page 46).

[107] Hajime Nakanotani et al. 'High-efficiency organic light-emitting diodes with fluorescent emitters'. In: *Nature Communications* 5 (2014), p. 4061 (cited on page 46).

[108] Y. Olivier et al. 'Computational Design of Thermally Activated Delayed Fluorescence Materials: The Challenges Ahead'. In: *The Journal of Physical Chemistry Letters* 9.20 (2018), pp. 6149–6163. DOI: 10.1021/acs.jpclett.8b02327 (cited on pages 47, 50, 68, 73, 84, 98).

[109] Mostafa A. El-Sayed. 'Triplet state. Its radiative and nonradiative properties'. In: *Accounts of Chemical Research* 1.1 (1968), pp. 8–16. DOI: 10.1021/ar50001a002 (cited on page 47).

[110] Chan Seok Oh et al. 'Dihedral Angle Control of Blue Thermally Activated Delayed Fluorescent Emitters through Donor Substitution Position for Efficient Reverse Intersystem Crossing'. In: *ACS Applied Materials & Interfaces* 10.41 (2018), pp. 35420–35429. DOI: 10.1021/acsami.8b10595 (cited on page 48).

[111] D. K. Andrea Phan Huu, Sangeeth Saseendran, and Anna Painelli. 'Effective models for TADF: the role of the medium polarizability'. In: *Journal of Materials Chemistry C* (2022), pp. 4620–4628. DOI: 10.1039/d1tc05296a (cited on pages 48, 73–75, 80).

[112] D. K. Andrea Phan Huu et al. 'Thermally Activated Delayed Fluorescence: Polarity, Rigidity, and Disorder in Condensed Phases'. In: *Journal of the American Chemical Society* 144.33 (2022). PMID: 35944182, pp. 15211–15222. DOI: 10.1021/jacs.2c05537 (cited on page 48).

[113] Katsuaki Kawasumi et al. 'Thermally Activated Delayed Fluorescence Materials Based on Homoconjugation Effect of Donor–Acceptor Triptycenes'. In: *Journal of the American Chemical Society* 137.37 (2015). PMID: 26367852, pp. 11908–11911. DOI: 10.1021/jacs.5b07932 (cited on page 48).

[114] Francesca Terenziani, Gabriele D'Avino, and Anna Painelli. 'Multichromophores for Nonlinear Optics: Designing the Material Properties by Electrostatic Interactions'. In: *ChemPhysChem* 8.17 (2007), pp. 2433–2444 (cited on pages 49, 50).

[115] Francesca Terenziani et al. 'Charge Instability in Quadrupolar Chromophores: Symmetry Breaking and Solvatochromism'. In: *Journal of the American Chemical Society* 128.49 (2006), pp. 15742–15755 (cited on page 49).

[116] Gabriele D'Avino, Francesca Terenziani, and Anna Painelli. 'Aggregates of Quadrupolar Dyes: Giant Two-Photon Absorption from Biexciton States'. In: *The Journal of Physical Chemistry B* 110.51 (2006), pp. 25590–25592 (cited on page 50).

[117] Cristina Sissa et al. 'Dimers of Quadrupolar Chromophores in Solution: Electrostatic Interactions and Optical Spectra'. In: *The Journal of Physical Chemistry B* 114.2 (2010), pp. 882–893 (cited on page 50).

[118] Francesco Di Maiolo and Anna Painelli. 'Intermolecular Energy Transfer in Real Time'. In: *Journal of Chemical Theory and Computation* 14.10 (2018). PMID: 30141921, pp. 5339–5349. DOI: `10.1021/acs.jctc.8b00540` (cited on pages 50, 64, 86).

[119] Andreas Dreuw and Martin Head-Gordon. 'Single-Reference ab Initio Methods for the Calculation of Excited States of Large Molecules'. In: *Chemical Reviews* 105.11 (2005), pp. 4009–4037 (cited on pages 50, 97).

[120] Michael J. G. Peach et al. 'Excitation energies in density functional theory: An evaluation and a diagnostic test'. In: *The Journal of Chemical Physics* 128.4 (2008), p. 044118 (cited on page 50).

[121] Wei-Lung Tsai et al. 'A versatile thermally activated delayed fluorescence emitter for both highly efficient doped and non-doped organic light emitting devices'. In: *Chem. Commun.* 51 (71 2015), pp. 13662–13665. DOI: `10.1039/C5CC05022G` (cited on page 51).

[122] Michael Y. Wong and Eli Zysman-Colman. 'Purely Organic Thermally Activated Delayed Fluorescence Materials for Organic Light-Emitting Diodes'. In: *Advanced Materials* 29.22 (2017), p. 1605444. DOI: `10.1002/adma.201605444` (cited on page 51).

[123] Axel D. Becke. 'Density-functional thermochemistry. III. The role of exact exchange'. In: *The Journal of Chemical Physics* 98.7 (1993), pp. 5648–5652. DOI: `10.1063/1.464913` (cited on page 52).

[124] Takeshi Yanai, David P Tew, and Nicholas C Handy. 'A new hybrid exchange–correlation functional using the Coulomb-attenuating method (CAM-B3LYP)'. In: *Chemical Physics Letters* 393.1 (2004), pp. 51–57. DOI: `https://doi.org/10.1016/j.cplett.2004.06.011` (cited on page 52).

[125] Yan Zhao and Donald G. Truhlar. 'The M06 suite of density functionals for main group thermochemistry, thermochemical kinetics, noncovalent interactions, excited states, and transition elements: two new functionals and systematic testing of four M06-class functionals and 12 other functionals'. In: *Theor. Chem. Acc.* 120 (2008), pp. 215–241. DOI: `10.1007/s00214-007-0310-x` (cited on page 52).

[126] Haitao Sun, Cheng Zhong, and Jean-Luc Brédas. 'Reliable Prediction with Tuned Range-Separated Functionals of the Singlet-Triplet Gap in Organic Emitters for Thermally Activated Delayed Fluorescence'. In: *Journal of Chemical Theory and Computation* 11.8 (2015). PMID: 26574466, pp. 3851–3858. DOI: `10.1021/acs.jctc.5b00431` (cited on page 52).

[127] Frank Neese. 'The ORCA program system'. In: *WIREs Computational Molecular Science* 2.1 (2012), pp. 73–78. DOI: `10.1002/wcms.81` (cited on pages 52, 72).

[128] Frank Neese. 'Efficient and accurate approximations to the molecular spin-orbit coupling operator and their use in molecular g-tensor calculations'. In: *The Journal of Chemical Physics* 122.3 (2005), p. 034107. DOI: `10.1063/1.1829047` (cited on pages 52, 72).

[129] Thomas Froitzheim, Stefan Grimme, and Jan-Michael Mewes. 'Either Accurate Singlet–Triplet Gaps or Excited-State Structures: Testing and Understanding the Performance of TD-DFT for TADF Emitters'. In: *Journal of Chemical Theory and Computation* 18.12 (2022). PMID: 36409831, pp. 7702–7713. DOI: `10.1021/acs.jctc.2c00905` (cited on page 52).

[130] Tamar Stein, Leeor Kronik, and Roi Baer. 'Reliable Prediction of Charge Transfer Excitations in Molecular Complexes Using Time-Dependent Density Functional Theory'. In: *Journal of the American Chemical Society* 131.8 (2009), pp. 2818–2820. DOI: 10.1021/ja8087482 (cited on page 52).

[131] Haitao Sun and Jochen Autschbach. 'Influence of the Delocalization Error and Applicability of Optimal Functional Tuning in Density Functional Calculations of Nonlinear Optical Properties of Organic Donor-Acceptor Chromophores'. In: *ChemPhysChem* 14.11 (2013), pp. 2450–2461. DOI: 10.1002/cphc.201300256 (cited on page 52).

[132] Painelli, A. and Terenziani, F. 'Optical Spectra of Push-Pull Chromophores in Solution: A Simple Model'. In: *The Journal of Physical Chemistry A* 104.47 (2000), pp. 11041–11048 (cited on pages 54, 57, 112).

[133] Cristina Sissa et al. 'Tuning the Nature of the Fluorescent State: A Substituted Polycondensed Dye as a Case Study'. In: *Chemistry - A European Journal* 19.3 (2012), pp. 924–935. DOI: 10.1002/chem.201202154 (cited on pages 54, 59).

[134] Luca Grisanti et al. 'Enhancing the efficiency of two-photon absorption by metal coordination'. In: *Physical Chemistry Chemical Physics* 11.41 (2009), p. 9450. DOI: 10.1039/b911268e (cited on page 54).

[135] Painelli, A. 'Vibronic contribution to static NLO properties: exact results for the DA dimer'. In: *Chemical Physics Letters* 285.5 (1998), pp. 352–358 (cited on page 55).

[136] Ángel Piñeiro et al. 'Refractive Indexes of Binary Mixtures of Tetrahydrofuran with 1-Alkanols at 25°C and Temperature Dependence of n and ρ for the Pure Liquids'. In: *Journal of Solution Chemistry* 31.5 (2002), pp. 369–380. DOI: 10.1023/A:1015807331250 (cited on page 59).

[137] Gerold U. Bublitz and Steven G. Boxer. 'Effective Polarity of Frozen Solvent Glasses in the Vicinity of Dipolar Solutes'. In: *Journal of the American Chemical Society* 120.16 (1998), pp. 3988–3992. DOI: 10.1021/ja971665c (cited on page 59).

[138] S. Di Bella, T. J. Marks, and M. A. Ratner. 'Environmental Effects on Nonlinear Optical Chromophore Performance. Calculation of Molecular Quadratic Hyperpolarizabilities in Solvating Media'. In: *J. Am. Chem. Soc.* 116 (1994), pp. 4440–4445 (cited on page 61).

[139] A. V. Marenich et al. 'Practical computation of electronic excitation in solution: vertical excitation model'. In: *Chem. Sci.* 2 (2011), pp. 2143–2161 (cited on page 61).

[140] Matthias Hempe et al. 'Vibrational Damping Reveals Vibronic Coupling in Thermally Activated Delayed Fluorescence Materials'. In: *Chemistry of Materials* 33.9 (2021), pp. 3066–3080. DOI: 10.1021/acs.chemmater.0c03783 (cited on page 66).

[141] Naoya Aizawa et al. 'Kinetic prediction of reverse intersystem crossing in organic donor–acceptor molecules'. In: *Nature Communications* 11.1 (2020), p. 3909. DOI: 10.1038/s41467-020-17777-2 (cited on pages 68, 70).

[142] Abraham Nitzan. *Chemical dynamics in condensed phases : relaxation, transfer, and reactions in condensed molecular systems*. Oxford: Oxford University Press, 2013 (cited on pages 68, 75).

[143] Neil R. Kestner, Jean Logan, and Joshua Jortner. 'Thermal electron transfer reactions in polar solvents'. In: *J. Phys. Chem.* 78.21 (1974), pp. 2148–2166. DOI: 10.1021/j100614a017 (cited on page 68).

[144] Jean-Luc Brédas et al. 'Charge-Transfer and Energy-Transfer Processes in π-Conjugated Oligomers and Polymers: A Molecular Picture'. In: *Chem. Rev.* 104.11 (2004), pp. 4971–5004. DOI: 10.1021/cr040084k (cited on page 68).

[145]   Jan-Michael Mewes. 'Modeling TADF in organic emitters requires a careful consideration of the environment and going beyond the Franck–Condon approximation'. In: *Physical Chemistry Chemical Physics* 20.18 (2018), pp. 12454–12469. DOI: `10.1039/c8cp01792a` (cited on pages 71, 73, 87, 88).

[146]   Thomas J. Penfold et al. 'Spin-Vibronic Mechanism for Intersystem Crossing'. In: *Chemical Reviews* 118.15 (2018), pp. 6975–7025. DOI: `10.1021/acs.chemrev.7b00617` (cited on page 71).

[147]   Christel M. Marian et al. 'Intersystem Crossing Processes in TADF Emitters'. In: *Highly Efficient OLEDs*. John Wiley & Sons, Ltd, 2018. Chap. 8, pp. 257–296. DOI: `https://doi.org/10.1002/9783527691722.ch8` (cited on page 72).

[148]   Kleitos Stavrou, Larissa G. Franca, and Andrew P. Monkman. 'Photophysics of TADF Guest–Host Systems: Introducing the Idea of Hosting Potential'. In: *ACS Applied Electronic Materials* 2.9 (2020), pp. 2868–2881. DOI: `10.1021/acsaelm.0c00514` (cited on pages 72, 76, 83, 84, 115, 117, 118).

[149]   W. Liptay. 'Electrochromism and Solvatochromism'. In: *Angewandte Chemie International Edition in English* 8.3 (1969), pp. 177–188. DOI: `10.1002/anie.196901771` (cited on page 73).

[150]   Terenziani, F. and Painelli, A. and Girlando, A. and Metzger, R. M. 'From Solution to Langmuir-Blodgett Films: Spectroscopic Study of a Zwitterionic Dye'. In: *The Journal of Physical Chemistry B* 108.30 (2004), pp. 10743–10750 (cited on page 73).

[151]   Lukas Kunze et al. 'PCM-ROKS for the Description of Charge-Transfer States in Solution: Singlet–Triplet Gaps with Chemical Accuracy from Open-Shell Kohn–Sham Reaction-Field Calculations'. In: *The Journal of Physical Chemistry Letters* 12.35 (2021). PMID: 34449230, pp. 8470–8480. DOI: `10.1021/acs.jpclett.1c02299` (cited on page 73).

[152]   Alexander J. Gillett et al. 'Dielectric control of reverse intersystem crossing in thermally activated delayed fluorescence emitters'. In: *Nature Materials* 21.10 (2022), pp. 1150–1157. DOI: `10.1038/s41563-022-01321-2` (cited on page 74).

[153]   Tatu Kumpulainen et al. 'Ultrafast Elementary Photochemical Processes of Organic Molecules in Liquid Solution'. In: *Chemical Reviews* 117.16 (2016), pp. 10826–10939. DOI: `10.1021/acs.chemrev.6b00491` (cited on page 77).

[154]   Axel Kahnt et al. 'Temperature Dependence of Charge Separation and Recombination in Porphyrin Oligomer–Fullerene Donor–Acceptor Systems'. In: *Journal of the American Chemical Society* 133.25 (2011), pp. 9863–9871. DOI: `10.1021/ja2019367` (cited on page 77).

[155]   Alexander Aster et al. 'Tuning symmetry breaking charge separation in perylene bichromophores by conformational control'. In: *Chemical Science* 10.45 (2019), pp. 10629–10639. DOI: `10.1039/c9sc03913a` (cited on page 77).

[156]   A. Bello, E. Laredo, and M. Grimau. 'Distribution of relaxation times from dielectric spectroscopy using Monte Carlo simulated annealing: Application to $\alpha - $ PVDF'. In: *Phys. Rev. B* 60 (18 1999), pp. 12764–12774. DOI: `10.1103/PhysRevB.60.12764` (cited on page 78).

[157]   Zulkifli Ahmad. 'Polymer Dielectric Materials'. In: *Dielectric Material*. Ed. by Marius Alexandru Silaghi. Rijeka: IntechOpen, 2012. Chap. 1. DOI: `10.5772/50638` (cited on page 78).

[158]   X. de Vries and R. Coehoorn. 'Vibrational mode contribution to the dielectric permittivity of disordered small-molecule organic semiconductors'. In: *Phys. Rev. Materials* 4 (8 2020), p. 085602. DOI: `10.1103/PhysRevMaterials.4.085602` (cited on page 78).

[159]   F. B. Dias, T. J Penfold, and A. P. Monkman. 'Photophysics of thermally activated delayed fluorescence molecules'. In: *Methods Appl. Fluoresc.* 5.1 (2017), p. 012001 (cited on page 84).

[160] M. D. Ediger. 'Perspective: Highly stable vapor-deposited glasses'. In: *The Journal of Chemical Physics* 147.21 (2017), p. 210901. DOI: 10.1063/1.5006265 (cited on page 84).

[161] Feng-Ming Xie et al. 'Effects of the relative position and number of donors and acceptors on the properties of TADF materials'. In: *Journal of Materials Chemistry C* 8.28 (2020), pp. 9476–9494. DOI: 10.1039/d0tc02252g (cited on page 86).

[162] F. Di Maiolo and A. Painelli. 'Dynamical disorder and resonance energy transfer: a novel quantum-classical approach'. In: *Physical Chemistry Chemical Physics* 22.3 (2020), pp. 1061–1068. DOI: 10.1039/c9cp06038c (cited on page 86).

[163] Stéphanie Valleau, Alexander Eisfeld, and Alán Aspuru-Guzik. 'On the alternatives for bath correlators and spectral densities from mixed quantum-classical simulations'. In: *The Journal of Chemical Physics* 137.22 (2012), p. 224103. DOI: 10.1063/1.4769079 (cited on page 87).

[164] Chao Wang and Qisheng Zhang. 'Understanding Solid-State Solvation-Enhanced Thermally Activated Delayed Fluorescence Using a Descriptor-Tuned Screened Range-Separated Functional'. In: *J. Phys. Chem. C* 123 (2019), pp. 4407–4416. DOI: 10.1021/acs.jpcc.8b08228 (cited on page 89).

[165] Tomas Serevičius et al. 'Temporal Dynamics of Solid-State Thermally Activated Delayed Fluorescence: Disorder or Ultraslow Solvation?' In: *The Journal of Physical Chemistry Letters* 13.7 (2022). PMID: 35174704, pp. 1839–1844. DOI: 10.1021/acs.jpclett.1c03810 (cited on page 89).

[166] Erich Runge and E. K. U. Gross. 'Density-Functional Theory for Time-Dependent Systems'. In: *Phys. Rev. Lett.* 52 (12 1984), pp. 997–1000 (cited on page 97).

[167] J. Cizek and J. Paldus. 'Stability Conditions for the Solutions of the Hartree-Fock Equations for Atomic and Molecular Systems. Application to the Pi-Electron Model of Cyclic Polyenes'. In: *The Journal of Chemical Physics* 47.10 (1967), pp. 3976–3985 (cited on page 98).

[168] Haitao Sun, Cheng Zhong, and Jean-Luc Brédas. 'Reliable Prediction with Tuned Range-Separated Functionals of the Singlet-Triplet Gap in Organic Emitters for Thermally Activated Delayed Fluorescence'. In: *Journal of Chemical Theory and Computation* 11.8 (2015). PMID: 26574466, pp. 3851–3858. DOI: 10.1021/acs.jctc.5b00431 (cited on pages 98, 99).

[169] Kiet A. Nguyen, Paul N. Day, and Ruth Pachter. 'The performance and relationship among range-separated schemes for density functional theory'. In: *The Journal of Chemical Physics* 135.7 (2011), p. 074109. DOI: 10.1063/1.3624889 (cited on page 99).

[170] Oleg A. Vydrov and Gustavo E. Scuseria. 'Assessment of a long-range corrected hybrid functional'. In: *The Journal of Chemical Physics* 125.23 (2006), p. 234109. DOI: 10.1063/1.2409292 (cited on page 99).

[171] Alexandra E. Raeber and Bryan M. Wong. 'The Importance of Short- and Long-Range Exchange on Various Excited State Properties of DNA Monomers, Stacked Complexes, and Watson-Crick Pairs'. In: *Journal of Chemical Theory and Computation* 11.5 (2015). PMID: 26574420, pp. 2199–2209. DOI: 10.1021/acs.jctc.5b00105 (cited on page 99).

[172] Leeor Kronik et al. 'Excitation Gaps of Finite-Sized Systems from Optimally Tuned Range-Separated Hybrid Functionals'. In: *Journal of Chemical Theory and Computation* 8.5 (2012). PMID: 26593646, pp. 1515–1531. DOI: 10.1021/ct2009363 (cited on page 99).

[173] Julien Eng, Beth A. Laidlaw, and Thomas J. Penfold. 'On the geometry dependence of tuned-range separated hybrid functionals'. In: *Journal of Computational Chemistry* 40.25 (2019), pp. 2191–2199. DOI: 10.1002/jcc.25868 (cited on page 100).

[174] Tian Lu and Feiwu Chen. 'Multiwfn: A multifunctional wavefunction analyzer'. In: *J. Comput. Chem.* 33 (2012), pp. 580–592. DOI: `10.1002/jcc.22885` (cited on page 108).

[175] Terenziani, F. and Painelli, A. 'Two-dimensional electronic-vibrational spectra: modeling correlated electronic and nuclear motion'. In: *Phys. Chem. Chem. Phys.* 17 (19 2015), pp. 13074–13081 (cited on page 112).

List of publications

▶ D. K. A. Phan Huu, R. Dhali, C. Pieroni, F. Di Maiolo, C. Sissa, F. Terenziani and A. Painelli, "Antiadiabatic view of fast environmental effects on optical spectra" *Physical Review Letters*, vol. 124, p. 107401, 2020.

▶ D. K. A. Phan Huu, C. Sissa, F. Terenziani, and A. Painelli, "Optical spectra of organic dyes in condensed phases: the role of the medium polarizability" *Physical Chemistry Chemical Physics*, vol. 22, p. 25483-25491, 2020.

▶ R. Dhali, D. K. A. Phan Huu, F. Bertocchi, C. Sissa, F. Terenziani and A. Painelli, "Understanding TADF: a joint experimental and theoretical study of DMAC-TRZ" *Physical Chemistry Chemical Physics*, vol. 23, p. 378-387, 2021.

▶ R. Dhali, D. K. A. Phan Huu, F. Terenziani, C. Sissa and A. Painelli, "Thermally activated delayed fluorescence: A critical assessment of environmental effects on the singlet–triplet energy gap" *The Journal of Chemical Physics*,vol. 154, p. 134112, 2021.

▶ D. K. A. Phan Huu, S. Saseendran and A. Painelli, "Effective models for TADF: the role of the medium polarizability" *Journal of Materials Chemistry C*, vol. 10, p. 4620-4628, 2022.

▶ D. K. A. Phan Huu, S. Saseendran, R. Dhali, L. G. Franca, K. Stavrou, A. P. Monkman and A. Painelli, "Thermally activated delayed fluorescence: polarity, rigidity, and disorder in condensed phases" *Journal of the American Chemical Society*, vol. 144, p. 15211-15222, 2022.

▶ C. Sissa, K Swathi, M. Sujith, PS Divya, M. P Varghese, A. Delledonne, D. K. A. Phan Huu, F. Di Maiolo, F. Terenziani, A. Lapini, A. Painelli and K. G. Thomas "From Symmetry Breaking to Symmetry Swap: Is Kasha's Rule Violated in Multibranched Phenyleneethynylenes?" *Chemical Science*, 2023, Advance Article.